Eur. Phys. J. C (2023) 83:1028
https://doi.org/10.1140/epjc/s10052-023-12090-w

THE EUROPEAN PHYSICAL JOURNAL C

Experimental Physics

Developments and results in the context of the JEM-EUSO program obtained with the ESAF simulation and analysis framework

S. Abe[1], J. H. Adams Jr.[2], D. Allard[3], P. Alldredge[2], L. Anchordoqui[4], A. Anzalone[5,6], E. Arnone[7,8], B. Baret[3], D. Barghini[7,8], M. Battisti[7,8], J. Bayer[10], R. Bellotti[11,12], A. A. Belov[13], M. Bertaina[7,8,a], P. F. Bertone[14], M. Bianciotto[7,8], P. L. Biermann[15], F. Bisconti[7,16], C. Blaksley[17], S. Blin-Bondil[3], P. Bobik[18], K. Bolmgren[19], S. Briz[20], J. Burton[2], F. Cafagna[11,12], G. Cambié[16,21], D. Campana[22], F. Capel[23], R. Caruso[6,24], M. Casolino[16,17,21], C. Cassardo[7,8], A. Castellina[7,25], K. Černý[26], M. J. Christl[14], R. Colalillo[22,27], L. Conti[16,28], G. Cotto[7,8], H. J. Crawford[29], R. Cremonini[8], A. Creusot[3], A. Cummings[56], A. de Castro Gónzalez[20], C. de la Taille[30], L. del Peral[33], R. Diesing[20], P. Dinaucourt[30], A. Di Nola[27], A. Ebersoldt[15], T. Ebisuzaki[17], J. Eser[20], F. Fenu[7,8,53,b], S. Ferrarese[7,8], G. Filippatos[31], W. W. Finch[31], F. Flaminio[27], C. Fornaro[16,28], D. Fuehne[31], C. Fuglesang[19], M. Fukushima[32], D. Gardiol[7,25], G. K. Garipov[13], A. Golzio[7,8], P. Gorodetzky[3], F. Guarino[22,27], C. Guépin[20], A. Guzmán[10], A. Haungs[15], T. Heibges[31], J. Hernández-Carretero[33], F. Isgrò[22,27], E. G. Judd[29], F. Kajino[34], I. Kaneko[17], Y. Kawasaki[17†], M. Kleifges[15], P. A. Klimov[13], I. Kreykenbohm[35], J. F. Krizmanic[36], V. Kungel[31], E. Kuznetsov[2], F. López Martínez[20], S. Mackovjak[18], D. Mandát[37], M. Manfrin[7,8], A. Marcelli[21], L. Marcelli[16], W. Marszał[38], J. N. Matthews[39], A. Menshikov[15], T. Mernik[10], M. Mese[22,27], S. S. Meyer[20], J. Mimouni[40], H. Miyamoto[7,8], Y. Mizumoto[41], A. Monaco[11,12], J.A Morales de los Ríos[33], S. Nagataki[17], J. M. Nachtman[42], D. Naumov[43], A. Neronov[3], T. Nonaka[32], T. Ogawa[17], S. Ogio[32], H. Ohmori[17], A. V. Olinto[20], Y. Onel[42], G. Osteria[22], A. Pagliaro[5,6], B. Panico[22,27], E. Parizot[3,9], I. H. Park[44], B. Pastircak[18], T. Paul[4], M. Pech[37], F. Perfetto[22], P. Picozza[16,21], L. W. Piotrowski[45], Z. Plebaniak[8,16,21,38,c], J. Posligua[42], R. Prevete[22,27], G. Prévôt[3], H. Prieto[33], M. Przybylak[38], M. Putis[18], E. Reali[16,21], P. Reardon[2], M. H. Reno[42], M. Ricci[46], M. Rodríguez Frías[33,55], G. Romoli[16,21], G. Sáez Cano[33], H. Sagawa[32], N. Sakaki[17], A. Santangelo[10], O. A. Saprykin[47], F. Sarazin[31], M. Sato[48], H. Schieler[15], P. Schovánek[37], V. Scotti[22,27], S. Selmane[3], S. A. Sharakin[13], K. Shinozaki[38], J. F. Soriano[4], J. Szabelski[38], N. Tajima[17], T. Tajima[17,57], Y. Takahashi[48], M. Takeda[32], Y. Takizawa[17], C. Tenzer[10], S. B. Thomas[39], L. G. Tkachev[43], T. Tomida[49], S. Toscano[50], M. Traïche[51], D. Trofimov[3,13], K. Tsuno[17], P. Vallania[7,25], L. Valore[27,22], T. M. Venters[36], C. Vigorito[7,8], P. von Ballmoos[54], M. Vrabel[38], S. Wada[17], J. Watts Jr.[2], A. Weindl[15], L. Wiencke[31], J. Wilms[35], D. Winn[52], H. Wistrand[31], I. V. Yashin[13], R. Young[14], M. Yu. Zotov[13]

[1] Nihon University, Funabashi, Chiba, Japan
[2] University of Alabama in Huntsville, Huntsville, AL, USA
[3] Université de Paris, CNRS, AstroParticule et Cosmologie, 75013 Paris, France
[4] Lehman College, City University of New York (CUNY), New York, NY, USA
[5] INAF-Istituto di Astrofisica Spaziale e Fisica Cosmica di Palermo, Palermo, Italy
[6] Istituto Nazionale di Fisica Nucleare-Sezione di Catania, Catania, Italy
[7] Istituto Nazionale di Fisica Nucleare-Sezione di Torino, Turin, Italy
[8] Dipartimento di Fisica, Università degli Studi di Torino, Via Pietro Giuria 1, 10125 Turin, Italy
[9] Institut universitaire de France (IUF), Paris, France
[10] Institute for Astronomy and Astrophysics, Kepler Center, University of Tübingen, Tübingen, Germany
[11] Istituto Nazionale di Fisica Nucleare-Sezione di Bari, Bari, Italy
[12] Università degli Studi di Bari Aldo Moro, Bari, Italy
[13] Skobeltsyn Institute of Nuclear Physics, Lomonosov Moscow State University, Moscow, Russia
[14] NASA Marshall Space Flight Center, Huntsville, AL, USA
[15] Karlsruhe Institute of Technology (KIT), Karlsruhe, Germany
[16] Istituto Nazionale di Fisica Nucleare-Sezione di Roma Tor Vergata, Rome, Italy
[17] RIKEN, Wako, Japan
[18] Slovak Academy of Science, Institute of Experimental Physics, Kosice, Slovakia
[19] KTH Royal Institute of Technology, Stockholm, Sweden

[20] University of Chicago, Chicago, IL, USA
[21] Dipartimento di Fisica, Università di Roma Tor Vergata, Rome, Italy
[22] Istituto Nazionale di Fisica Nucleare-Sezione di Napoli, Naples, Italy
[23] Max Planck Institute for Physics, Munich, Germany
[24] Dipartimento di Fisica e Astronomia "Ettore Majorana", Università di Catania, Catania, Italy
[25] Osservatorio Astrofisico di Torino, Istituto Nazionale di Astrofisica, Pino Torinese, Italy
[26] Joint Laboratory of Optics, Faculty of Science, Palacký University, Olomouc, Czech Republic
[27] Dipartimento di Fisica "Ettore Pancini", Università di Napoli Federico II, Naples, Italy
[28] Uninettuno University, Rome, Italy
[29] Space Science Laboratory, University of California, Berkeley, CA, USA
[30] Omega, Ecole Polytechnique, CNRS/IN2P3, Palaiseau, France
[31] Colorado School of Mines, Golden, CO, USA
[32] Institute for Cosmic Ray Research, University of Tokyo, Kashiwa, Japan
[33] Universidad de Alcalá (UAH), Madrid, Spain
[34] Konan University, Kobe, Japan
[35] ECAP, University of Erlangen-Nuremberg, Erlangen, Germany
[36] NASA Goddard Space Flight Center, Greenbelt, MD, USA
[37] Institute of Physics of the Czech Academy of Sciences, Prague, Czech Republic
[38] National Centre for Nuclear Research, Otwock, Poland
[39] University of Utah, Salt Lake City, UT, USA
[40] Lab. of Math. and Sub-Atomic Phys. (LPMPS), Univ. Constantine I, Constantine, Algeria
[41] National Astronomical Observatory, Mitaka, Japan
[42] University of Iowa, Iowa City, IA, USA
[43] Joint Institute for Nuclear Research, Dubna, Russia
[44] Sungkyunkwan University, Seoul, Republic of Korea
[45] Faculty of Physics, University of Warsaw, Warsaw, Poland
[46] Istituto Nazionale di Fisica Nucleare-Laboratori Nazionali di Frascati, Frascati, Italy
[47] Space Regatta Consortium, Korolev, Russia
[48] Hokkaido University, Sapporo, Japan
[49] Shinshu University, Nagano, Japan
[50] ISDC Data Centre for Astrophysics, Versoix, Switzerland
[51] Centre for Development of Advanced Technologies (CDTA), Algiers, Algeria
[52] Fairfield University, Fairfield, CT, USA
[53] Agenzia Spaziale Italiana, Via del Politecnico, 00133 Rome, Italy
[54] IRAP, Université de Toulouse, CNRS, Toulouse, France
[55] Center for Pulsed Lasers (CLPU), Salamanca, Spain
[56] Pennsylvania State University, State College, PA, USA
[57] Department of Physics and Astronomy, University of California, Irvine, USA
[†] Deceased

Received: 23 June 2023 / Accepted: 28 September 2023 / Published online: 13 November 2023

Abstract JEM-EUSO is an international program for the development of space-based Ultra-High Energy Cosmic Ray observatories. The program consists of a series of missions which are either under development or in the data analysis phase. All instruments are based on a wide-field-of-view telescope, which operates in the near-UV range, designed to detect the fluorescence light emitted by extensive air showers in the atmosphere. We describe the simulation software ESAF in the framework of the JEM-EUSO program and explain the physical assumptions used. We present here the implementation of the JEM-EUSO, POEMMA, K-EUSO, TUS, Mini-EUSO, EUSO-SPB1 and EUSO-TA configurations in ESAF. For the first time ESAF simulation outputs are compared with experimental data.

This paper is dedicated to Yoshiya Kawasaki who contributed significantly to the ESAF developments during the JEM-EUSO mission.

[a] e-mail: bertaina@to.infn.it (corresponding author)
[b] e-mail: francesco.fenu@gmail.com (corresponding author)
[c] e-mail: zbigniew.plebaniak@roma2.infn.it (corresponding author)

1 Introduction

The study of Ultra-High Energy Cosmic Rays (UHECRs) and the understanding of particle acceleration in the cosmos is of utmost importance for astro-particle physics as well as for fundamental physics. The current main goals are to identify sources of UHECRs and their composition. UHECRs above 5×10^{19} eV have a flux lower than 1 event per century per square kilometer [1], therefore, huge sensitive volumes are necessary to collect enough statistics.

A space-based detector for UHECR research has the advantage of a very large exposure and a uniform coverage of the celestial sphere. The idea of space-based observation of UHECRs was first proposed by John Linsley in the late 70s with the SOCRAS concept [2]. The principle of observation is based on the detection of UV light emitted by isotropic fluorescence of atmospheric nitrogen excited by Extensive Air Showers (EAS) in the Earth's atmosphere and forward-beamed Cherenkov radiation diffusely reflected from the Earth's surface or dense cloud tops. In 1995 Linsley's original idea was re-adapted by Yoshiyuki Takahashi into the MASS concept [3] which evolved in 1996, in the US, into the OWL mission [4]. In parallel the MASS, or Airwatch concept as it was later on renamed, evolved in Europe into EUSO, the Extreme Universe Space Observatory. Livio Scarsi first proposed EUSO as a free-flyer to the European Space Agency's (ESA) F2/F3 [5] call in 2000. ESA selected the mission but recast it as a payload for the Columbus module of the International Space Station (ISS) [6]. The phase-A study for the feasibility of EUSO, started in 2001 and was successfully completed in March 2004. Although EUSO was found technically ready to proceed into phase B, ESA did not continue the program.

In 2006, the Japanese and US teams, under the leadership of Yoshiyuki Takahashi, redefined the mission as an observatory attached to KIBO, the Japanese Experiment Module (JEM) of the ISS. They renamed the mission JEM-EUSO and started a new phase-A study targeting launch in 2013 in the framework of the second utilization phase of the JEM/EF (Exposure Facility) [7]. The Phase A/B1 study of JEM-EUSO led by Japan Aerospace Exploration Agency (JAXA) continued with extensive simulations, design, and prototype developments that significantly improved the JEM-EUSO mission profile (see Fig. 1), targeting a launch in 2016 [8].

As a result of this study, the main telescope was designed with a wide Field-of-View (FoV; ~ 0.85 sr) optics composed of three Fresnel lenses. Different configurations have been studied: the "side-cut" version of the instrument with a 2.65 m major axis and 1.9 m minor axis (4.5 m^2 optical aperture) to fit in the cargo of the JAXA HTV rocket as described in [10] and the SpaceX Dragon option with 2.5 m diameter circular optics [9]. The difference between the two configurations is shown in Fig. 2. The use of Fresnel lenses realized in Poly(Methyl MethAcrylate) – PMMA – allows building a refractor telescope capable of meeting the requirements of a large optical system with wide FoV with the constraints of a spaceborne experiment. Furthermore, the reduced thickness of the lenses allows to reduce the mass of the optics resulting in a light system capable of withstanding launch vibration and thermal expansion.

The telescope records the EAS-induced tracks with a time resolution of 2.5 μs, known as a Gate Time Unit (GTU). The Focal Surface (FS) detector is formed by 137 Photo Detector Modules (PDMs) comprising of $\sim$ 5000 Multi-Anode Photo-Multiplier Tubes (MAPMTs) in total (36 MAPMTs per PDM, 64 pixels each). Each PDM is composed by 9 Elementary Cells (ECs). One EC is composed by 4 MAPMTs, 64 pixels each. The FS detector is highly pixelated in $\sim 3 \times 10^5$ channels providing a pixel FoV of $\sim 0.074°$, equivalent to ~ 0.5 km at ground seen from an altitude of ~ 400 km. An optical filter is placed in front of the MAPMTs to select photons mainly in the fluorescence bandwidth (290–430 nm).

In 2013 it became clear that JEM-EUSO could not proceed further within the JAXA leadership. The mission was put on hold status and JEM-EUSO was reoriented as an extensive pathfinder program, with the acronym redefined as the Joint Experiment Missions for Extreme Universe Space Observatory [12]. The program includes several missions from ground (EUSO-TA [13]), on board of stratospheric balloons (EUSO-Balloon [14], EUSO-SPB1 [15], and EUSO-SPB2 [16]), and from space (TUS [17] and Mini-EUSO [18]). Each employs fluorescence detectors to test the observational technique, and to validate the technology. The final goal of the program is the realization of a large space-based mission following the concepts developed in the past decades, namely the medium-size K-EUSO [19] and the large-size POEMMA [20] missions.

All these detectors demand extensive simulation work to estimate their performance and to support the analysis of the collected data. It was clear at the time of the JEM-EUSO mission that the most efficient way was to re-adapt the existing software instead of developing totally new code. For this reason, the two official software packages adopted by JEM-EUSO are the Euso Simulation and Analysis Framework (ESAF) [21], originally developed within the EUSO project, and the $\overline{\text{Off}}\underline{\text{Line}}$ package [22] designed for the Pierre Auger Observatory [23]. A comparison between the two frameworks and their designs is reported in [16] while examples of cross-checks carried out in the past on their relative performance is summarized in Appendix C. The main motivations to adopt both packages are: (a) it is straightforward to re-adapt the EUSO code to the JEM-EUSO configuration; (b) $\overline{\text{Off}}\underline{\text{Line}}$ output is extensively tested within the Auger project and thus with experimental data; (c) the possibility to adopt both packages gives opportunities for cross-checks. A synthetic description of the developments performed with the $\overline{\text{Off}}\underline{\text{Line}}$ software to accommodate the different configurations of the telescopes of the JEM-EUSO program can be found in [24]. In this paper we summarize developments and performance results obtained with ESAF, including some of those already discussed in earlier publications.

The main objective of this paper is to demonstrate the potential and flexibility of the ESAF software and its applications in the context of the JEM-EUSO program. A comparison with experimental data is provided to show the utility of the ESAF software in the interpretation of the data. The

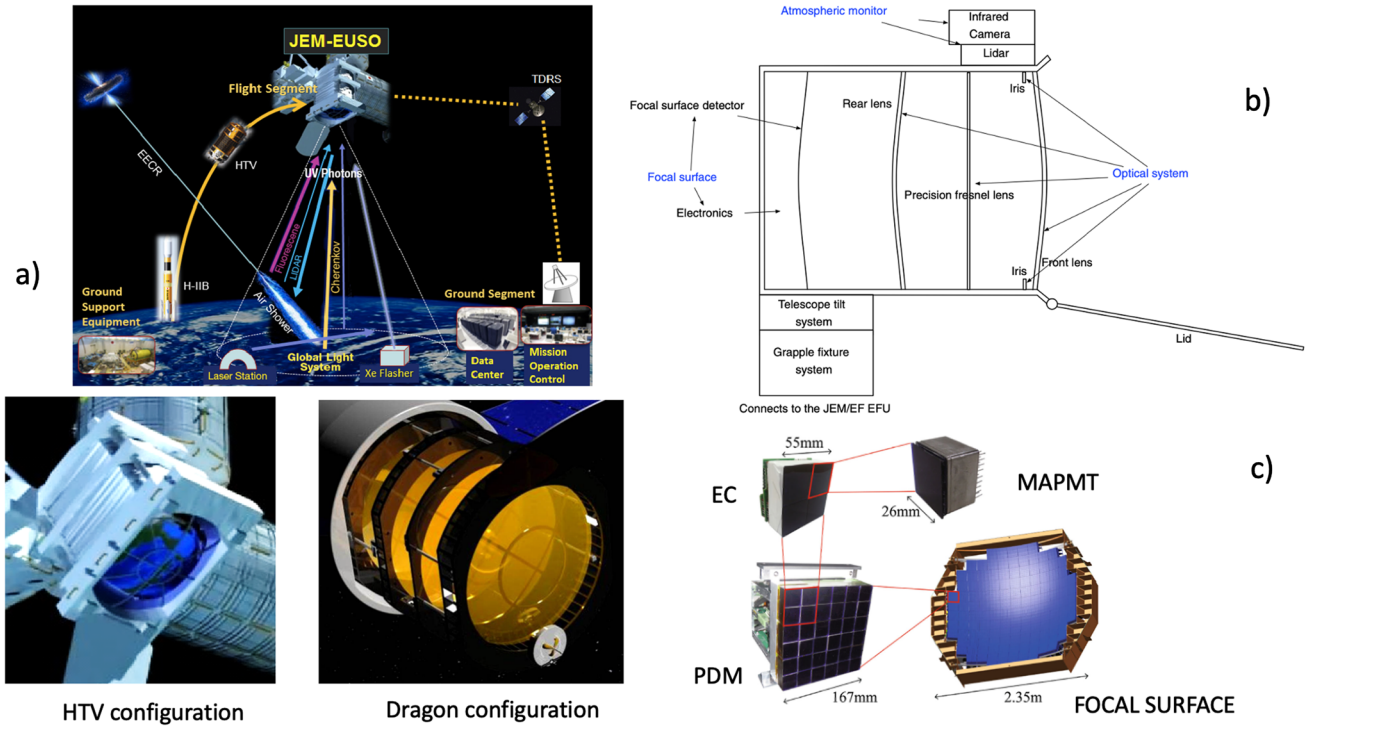

Fig. 1 Panel **a**: Conceptual view of the whole JEM-EUSO system. Panel **b**: Conceptual design of the JEM-EUSO system: three Fresnel lenses focus the light on the focal surface. Panel **c**: Conceptual design of the JEM-EUSO Focal Surface with its elements and sub-elements parts. The focal surface of the detector is formed by 137 Photo Detector Modules (PDMs) comprising of ∼ 5000 Multi-Anode Photo-Multiplier Tubes (MAPMTs) in total (36 MAPMTs per PDM, 64 pixels each). Each PDM is composed by 9 Elementary Cells (ECs). See the text for details. Figure adapted from [9]

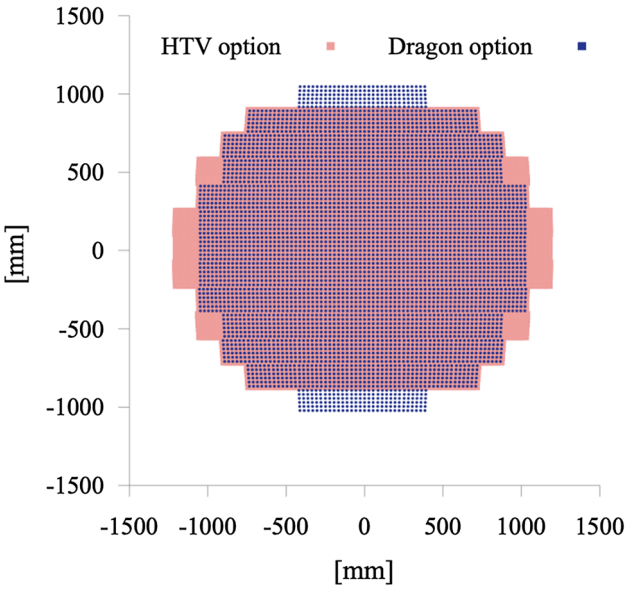

Fig. 2 A diagram of the position of the MAPMTs of the Dragon configuration (blue) of JEM-EUSO superimposed on the same diagram for the HTV configuration (red). Image taken from [11]

paper is structured in the following way. Section 2 outlines the detector characteristics of the different projects of the JEM-EUSO program which have been implemented in ESAF. Section 3 summarizes the main features of the ESAF framework while Sect. 4 reports the new ESAF developments performed within the JEM-EUSO program. Section 5 provides the key results obtained with simulations for the different detector configurations implemented in the software, namely JEM-EUSO, POEMMA, K-EUSO, Mini-EUSO, TUS, EUSO-SPB1 and EUSO-TA as well as comparisons with data. The conclusions and perspectives are the subject of Sect. 6.

2 The missions of the JEM-EUSO program

In this section we summarize the different configurations implemented in ESAF to simulate the performance of the various projects of the JEM-EUSO program which have been defined since the original JEM-EUSO mission was put on hold. A comparison of the main parameters of the different configurations is presented in Table 1.

Table 1 The main parameters of different configurations of JEM-EUSO experiments

Experiment	JEM-EUSO	K-EUSO	POEMMA	Mini-EUSO	TUS	EUSO-Balloon	EUSO-SPB1	EUSO-SPB2	EUSO-TA
Optics type	Lenses	Lenses	Mirror	Lenses	Mirror	Lenses	Lenses	Mirror	Lenses
Optics aperture (m^2)	~ 4.5	~ 3	~ 6	~ 0.05	~ 2	~ 1	~ 1	~ 1	~ 1
Height (km)	400	400	525	400	~ 500	~ 38	~ 33	~ 33	~ 0
FoV (°)	$\sim 64 \times 45$	$\sim 20 \times 15$	~ 45	~ 44	~ 9	~ 11	~ 11	12×36	~ 11
Area at ground (km^2)	1.4×10^5	4.8×10^4	1.5×10^5	$\sim 8 \times 10^4$	$\sim 6.4 \times 10^3$	~ 54	~ 40	~ 150	–
PDMs	137	44	55	1	1	1	1	3	1
Pixels	3.2×10^5	1×10^5	1.3×10^5	2304	256	2304	2304	6912	2304
Spatial ang. resolution (°)	~ 0.074	~ 0.1	~ 0.084	~ 0.9	~ 0.7	~ 0.2	~ 0.2	~ 0.25	~ 0.2
Pixel size at ground (km)	~ 0.5–0.6	~ 0.6–0.7	~ 0.8	~ 6.3	~ 5.0	~ 0.13	~ 0.12	~ 0.14	–
GTU (μs)	2.5	2.5	1.0	2.5	0.8	2.5	2.5	1.0	2.5
Bckg level (cts/pix/GTU)	1.1	0.6	1.5	~ 1.0	~ 18.0	~ 0.5–1.0	1–2	~ 1	1–2
Reference	[9,10]	[19]	[20,38]	[18,39]	[17,29]	[14,33]	[15]	[16,37]	[13]

K-EUSO is the result of the joint efforts to improve the performance of the Russian KLYPVE mission [25] by employing the technologies developed for the JEM-EUSO mission, such as the focal surface detectors and the readout electronics. The KLYPVE mission, named after Russian words "ultra-high energy cosmic rays" has undergone pre-phase A study, including launch and accommodation on the ISS. Since its first conception as KLYPVE, the K-EUSO project has passed various modifications aimed to increase the FoV and UHECR statistics [26,27], compatibly with shipping possibilities using the Soyuz spacecraft and to decrease the number of external vehicle activities by the astronauts. All the different improved solutions have been implemented in ESAF. We report in Sect. 5 on the expected performance of the latest version of the instrument under study [19,28] (see Fig. 3a).

In this configuration, the detector consists of a refractive optical system of 1400 mm $\times$ 2400 mm size. The optics is based on two Fresnel lenses that focus the light onto a focal surface of 1300 mm $\times$ 1000 mm size. The FS consists of 44 PDMs. Each pixel has a field of view of 0.1° which corresponds to $\sim$ 700 m on the ground. The time resolution is in the process of being optimized and ranges from 1 to 2.5 μs. The exact value will be based on a trade-off between the limited hardware and telemetry budgets and the need of a good time resolution. In the following, the 2.5 μs GTU has been adopted for simulations.

The Probe Of Extreme Multi-Messenger Astrophysics (POEMMA) design [20] combines the concept developed for the OWL mission and the experience of designing the JEM-EUSO fluorescence detection camera. POEMMA is composed of two identical satellites flying in formation at an altitude of 525 km with the ability to observe overlapping regions during moonless nights at angles ranging from nadir to just above the limb of the Earth, but also with independent pointing strategies to exploit at maximum the scientific program of the mission.

Each telescope (see Fig. 3b) is composed of a wide (45°) FoV Schmidt optical system with an optical collecting area of over 6 m^2. The focal surface of POEMMA is composed of a hybrid of two types of cameras: about 90% of the FS is dedicated to the POEMMA fluorescence camera (PFC), while the POEMMA Cherenkov camera (PCC) occupies the crescent moon shaped edge of the FS which images the limb of the Earth. The PFC is composed of 55 JEM-EUSO PDMs based on MAPMTs for a total of $\sim$ 130,000 channels. The GTU for the PFC is 1 μs. The much faster POEMMA Cherenkov camera (PCC) is composed of Silicon Photo-Multipliers (SiPMs) which is tested with EUSO-SPB2.

The world's first orbital detector aiming at detecting UHECRs was the Tracking Ultraviolet Setup (TUS) UV telescope, launched on April 28, 2016 as a part of the scientific payload of the Lomonosov satellite [17], see Fig. 4.

TUS provides the first opportunity to compare ESAF simulations to real data taken from space. Some examples can be found in [29] and are reported here. The instrument recorded data until the end of November 2017. Different scientific modes were tested: cosmic ray, lightning and meteor modes. The satellite had a sun-synchronous orbit (i.e. passing over any given point of the earth surface at the same local mean solar time) with an inclination of 97.3°, a period of $\sim$ 94 min, and a height of 470–500 km. The TUS telescope consisted of two main parts: a modular Fresnel mirror-concentrator with an area of $\sim$ 2 m^2 and 256 PMTs arranged in a 16 $\times$ 16 photo-receiver matrix located in the focal plane of the mirror. The FoV of one pixel was 10 mrad, which corresponds to a spatial spot of $\sim$ 5 km $\times$ 5 km at sea level. Thus, the full area observed by TUS at any moment was $\sim$ 80 km $\times$ 80 km. TUS was sensitive to the near-UV band and had a time resolution of 0.8 μs in the cosmic ray mode, with a full temporal

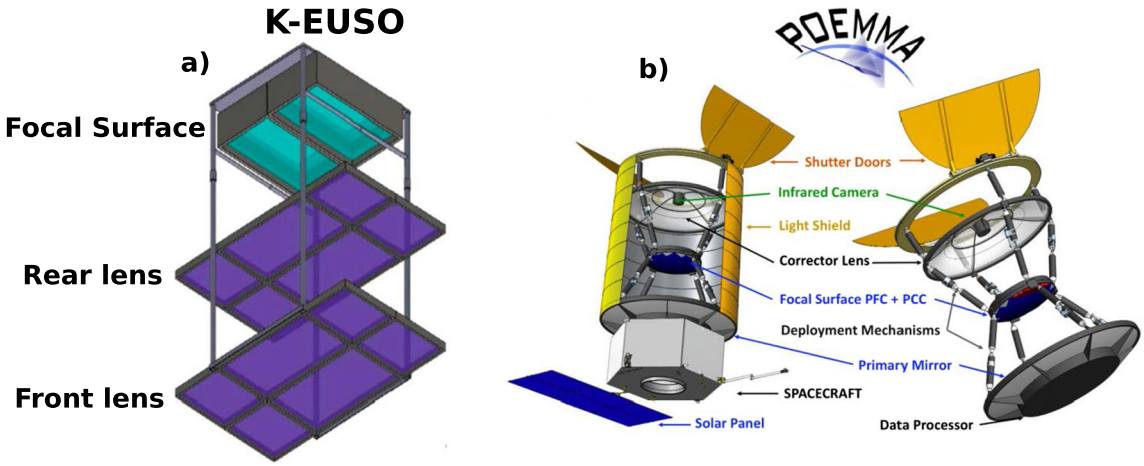

Fig. 3 Scheme of the simulated K-EUSO detector (panel **a**) and of the POEMMA telescope (panel **b**). Figure adapted from [19,20]

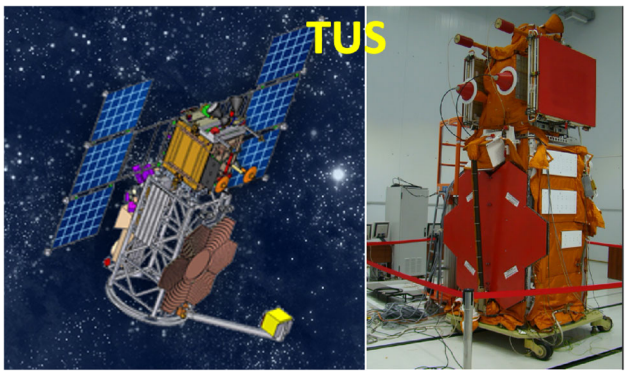

Fig. 4 Artist's view of the TUS detector on board the Lomonosov satellite (left) and preflight preparations at the Vostochny cosmodrome (right)

window of 256 time steps. TUS data offer the opportunity to develop strategies in the analysis and reconstruction of events which will be essential for future space-based missions.

Mini-EUSO [18] is an UV telescope launched in August 2019 and installed periodically inside the ISS, with installations occurring every couple of weeks since October 2019. Mini-EUSO is installed looking down on the Earth from a nadir-facing window in the Russian Zvezda module (see Fig. 5). So far $\sim$ 80 sessions of about 12 h of data taking have been performed.

Mini-EUSO maps the Earth in the UV range (290–430 nm) with a spatial resolutions of $\sim$ 6 km (similar to TUS) and three different temporal resolutions of 2.5 μs, 320 μs, and 41 ms operating simultaneously. While the 41 ms time range allows continuous video-taking, the other two modes allow acquisitions of 4 packets of 128 GTUs each every 5.24 s when the trigger condition is satisfied, to catch fast luminous transients (flashes, lightning, etc.). The optical system consists of 2 Fresnel lenses of 25 cm diameter each with a large FoV of $\sim$ 44°. Data carried down to Earth from the ISS allowed for the first analyses showing that Mini-EUSO observes different Earth emissions depending on the surface visible, e.g., ground, sea, or clouds as well as slow transients such as meteors. Tens of thousands of meteor events have been identified in the data with absolute magnitude lower than +5 (the events last typically in the order of 1 s). At shorter times scales (typically hundreds of μs), several hundreds of lightning associated signals (among them 26 elves) have been detected. In addition, many anthropogenic flashes presumably related to airport lights or other flashing tower lights have been acquired. A summary of the most recent results of Mini-EUSO can be found in [30].

While TUS was conceived mainly to prove the observation of UHECRs from space with a FS-instrumentation similar to ground-based detectors, Mini-EUSO has been developed in order to test the same FS-instrumentation foreseen for K-EUSO and POEMMA. Moreover, it is important to recall that Mini-EUSO was designed to detect similar photoelectron counts per pixel as JEM-EUSO in the case of diffused light sources. This is done by compensating the $\sim 10^{-2}$ times optics aperture with $\sim 10^2$ times wider pixel FoV. Therefore, these results on diffuse light sources are representative of observations of the future large missions K-EUSO and POEMMA, which have similar apertures and instantaneous FoV. As a consequence, Mini-EUSO energy threshold for UHECRs is well above 10^{21} eV as explained in Sect. 5.

The JEM-EUSO program includes stratospheric balloon missions with increasing level of performance and upgraded designs (see Fig. 6). In addition to demonstrating the capabilities of the JEM-EUSO instruments to detect and reconstruct EASs from the edge of space, they also give access to direct measurement of the UV nightglow emission and artificial UV contributions above ground and oceans, which are important information to optimize the design of the space-based missions. Three balloon flights have been performed so

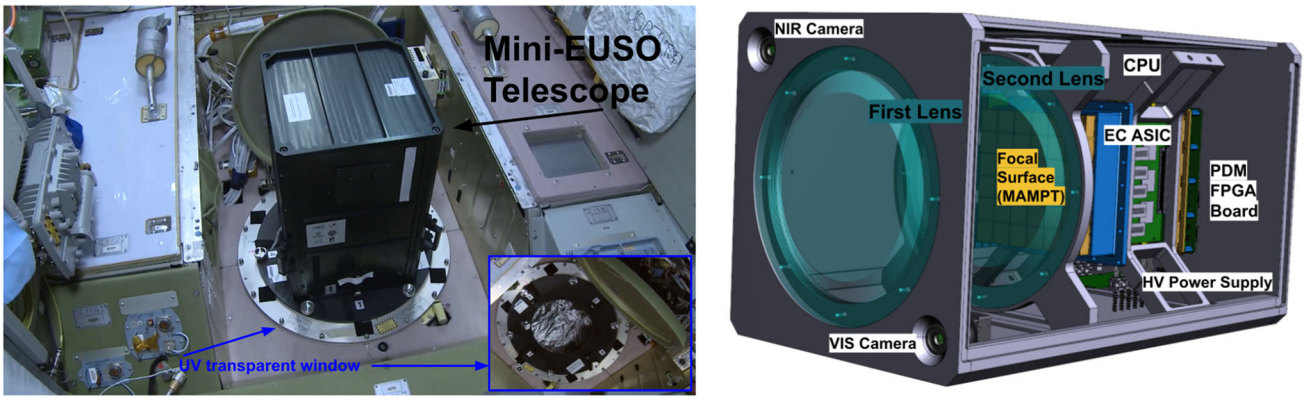

Fig. 5 Mini-EUSO attached to the Zvezda module on the ISS (left) and schematic view of the different parts of the Mini-EUSO detector (right)

Fig. 6 Stratospheric balloon missions EUSO-Balloon, EUSO-SPB1, and EUSO-SPB2, and ground mission EUSO-TA of the JEM-EUSO program. Image adapted from [12]

far: EUSO-Balloon (Canada, 1 night), EUSO-SPB1 (Pacific Ocean, 12 nights), and EUSO-SPB2 (Pacific Ocean, 37 h).

The telescope configuration of EUSO-Balloon and EUSO-SPB1 is similar: two Fresnel lenses of ~ 1 m^2 each and one PDM as FS with 2.5 μs time resolution.

EUSO-Balloon [14] was launched by National Centre for Space Studies in France (CNES) from the Timmins base in Ontario (Canada) on the moonless night of August 25, 2014. After reaching the floating altitude of $\sim$ 38 km, EUSO-Balloon imaged the UV intensity with a spatial and temporal resolutions of 130 m and 2.5 μs, respectively, in the wavelength range 290–430 nm for more than 5 h before descending to ground. The full FoV in nadir mode was $\sim 11°$. During 2.5 h of EUSO-Balloon flight, a helicopter circled under the balloon operating UV flashers and a UV laser to simulate the optical signals from UHECRs, to calibrate the apparatus, and to characterise the optical atmospheric conditions. Data collected by EUSO-Balloon have been analyzed to infer different information among which the response of the detector to the UV flasher and laser events, and the UV radiance from the Earth atmosphere and ground in different conditions: clear and cloudy atmosphere, forests, lakes, as well as city lights [31]. The helicopter events proved to be extremely useful to understand the system's performance and to test the capability of EUSO-Balloon to detect and reconstruct signals similar to EASs [32]. A summary of the results of the EUSO-Balloon mission is reported in [33].

EUSO-SPB1 [15] was launched on April 25, 2017 from Wanaka (New Zealand) as a mission of opportunity on a NASA SPB test flight planned to circle the southern hemisphere. The telescope was an upgraded version of that used in the EUSO-Balloon mission. The JEM-EUSO first level trigger was implemented with adaptations for a balloon observation [34]. Prior to flight, in October 2016, the fully assembled EUSO-SPB1 detector was tested for a week at the EUSO-TA site to measure its response and for calibrations by means of a portable Ground Laser System (GLS). Observations of the Central Laser Facility (CLF), stars and meteors were performed. Unfortunately, although the instrument was showing nominal behaviour and performance, the flight was terminated prematurely in the Pacific Ocean about 300 km SE of Easter Island after only 12 days aloft of the $\sim$ 100 scheduled,

due to a leak in the balloon, and the payload was lost. During flight, $\sim$ 30 h of data were collected [35].

EUSO-SPB2 [16] was launched on May 13, 2023 from Wanaka on a NASA SPB test flight. It was equipped with 2 telescopes. One telescope was devoted to UHECR measurements using the fluorescence technique. EUSO-SPB2 employed a Schmidt camera with 3 PDMs, a 1 μs GTU, and a more efficient balloon-oriented trigger logic to improve the sensitivity of the instrument [36]. The FS of the second telescope was based on SiPM sensors and a dedicated electronics to detect the Cherenkov emission in air by UHECR EASs. Unfortunately, the balloon developed a leak and was terminated over the Pacific Ocean after only about 37 hours of flight. Despite the very short flight, all instruments performed very well. Analysis of the flight data is ongoing. Preliminary results were presented in [37].

EUSO-TA [13] is a ground-based telescope, installed at the Telescope Array [40] (TA) site in Black Rock Mesa, Utah, USA (see Fig. 6). This is the first detector to successfully use a Fresnel lens based optical system and one PDM foreseen for JEM-EUSO with a 2.5 μs GTU. The FoV is $10.6^\circ \times 10.6^\circ$. The telescope is located in front of one of the fluorescence detector stations of the TA experiment. Between 2015 and 2016, a few campaigns of joint observations with TA allowed EUSO-TA to detect 9 UHECR events in $\sim$ 140 h of data taking, all lasting 1 or 2 GTUs at maximum, as well as a few meteors. The limiting magnitude of +5.5 on summed frames ($\sim$ 3 ms) was established. These observations provided important data to optimize the detector technology in view of subsequent balloon and space missions. The current upgrade of the detector includes a new acquisition system based on the Zynq board, like in Mini-EUSO, and the implementation of a self-triggering system which has become operational in June 2022.

3 An overview of the EUSO simulation and analysis framework

The Euso Simulation and Analysis Framework (ESAF) is a simulation and analysis software specifically designed for the performance assessment of space-based cosmic ray observatories. It has been developed in the framework of the EUSO project [21]. The software consists of $\sim 2 \cdot 10^5$ lines of code written in C++ following an object oriented approach and makes use of the ROOT data analysis framework developed at European Organization for Nuclear Research (CERN) [41].

In this section, we briefly summarize the key aspects of the ESAF software while in the following one we report on the new developments to support the JEM-EUSO program. A short technical description of the ESAF design is reported in Appendix A. See Ref. [21] for a detailed and comprehensive description of the ESAF software.

The ESAF software performs the simulation of an UHECR event, its detection and the shower parameter reconstruction. In more detail, the ESAF code includes: (a) EAS simulation both by means of internally developed algorithms (e.g., the SLAST shower generator, which includes the Greisen–Ilina–Linsley (GIL) parameterization [42]) and interfaces to existing widely-used codes (e.g., CORSIKA [43] or CONEX [44]); (b) a complete description of the atmosphere, including aerosols, ozone and Rayleigh scattering and clouds; (c) fluorescence and Cherenkov light production; (d) a complete simulation of photon propagation, from the production point up to the telescope, including diffuse reflection interactions with ground and atmosphere, and a Monte-Carlo code dealing with multiple scattering; (e) simulation of optics, geometry and a photodetector of a telescope; (f) simulation of the electronics, trigger, and background; (g) pattern recognition and shower signal identification above background; (h) reconstruction of direction, energy, and slant depth of the shower maximum ($X_{\max}$), i.e., the atmospheric depth of the shower maximum from the top of the atmosphere.

The ESAF software produces two distinct executable files called *Simu* and *Reco* respectively. The first one performs the simulation of the entire physical process, the second one activates the entire reconstruction chain. The two codes work independently.

4 Development of the ESAF simulation and reconstruction frameworks for JEM-EUSO

Since 2007, when ESAF was adopted also for the JEM-EUSO mission, new functionality was developed to include specific characteristics of the JEM-EUSO telescope. More recently, the configurations of almost all the projects conceived within the JEM-EUSO program have been developed as well. These new implementations include: (a) detector configurations and the new trigger algorithms; (b) two new track recognition algorithms named *Linear Track Trigger* (LTT) and *Peak and WIndow SEarching* (PWISE); (c) new reconstruction algorithms for the energy and $X_{\max}$ EAS parameters; (d) light transients emitted by other classes of events such as ground flashers, space debris, Transient Luminous Events (TLEs) [45], meteors and nuclearites [46].

In what follows, the ESAF software is described in more details and a few examples of its functionality are provided with specific emphasis on the new implementations.

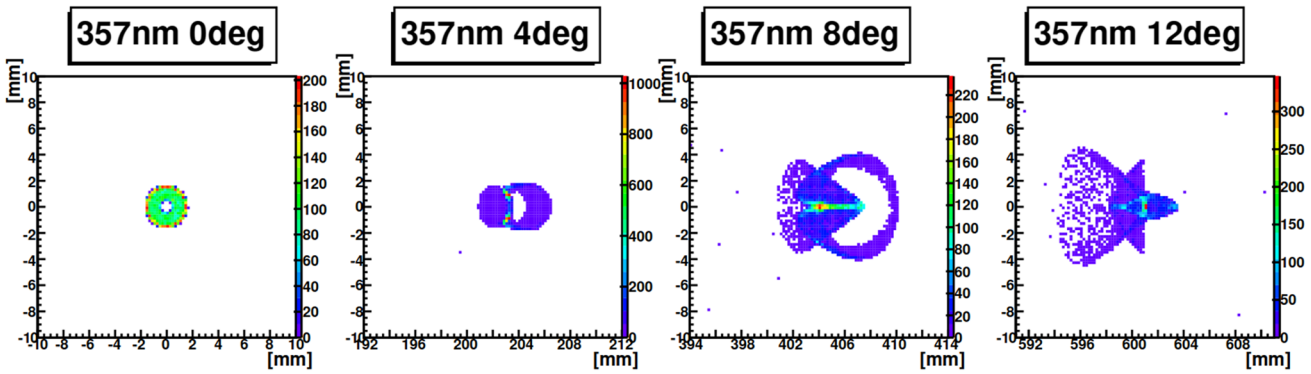

Fig. 7 PSF diagrams of one version of the K-EUSO optics. Panels correspond to light at 357 nm with incident angles from the optical axis 0°, 4°, 8° and 12° respectively. The size of each frame is 20 mm × 20 mm. The number of arrived photons increases as the color changes from blue to red. An arbitrary point-like source has been used to test the proper implementation of the optics response in ESAF code

4.1 The EAS simulation framework

The *Simu* framework of ESAF performs the simulation of the entire physical process from shower to telemetry. Both an extensive air shower and the photon propagation are simulated. CONEX [44] and CORSIKA [43] interfaces have been implemented in the framework in addition to the ESAF EAS generators such as SLAST [47]. All these generators are currently adopted in ESAF, depending on the objective of the simulation. CORSIKA and CONEX guarantee more carefully tuned to experimental results, however, the computation time is usually considerable. On the other hand, SLAST is a very fast simulator which can provide a sufficiently good approximation of the EAS development when the user is interested in an overall performance result. This is the simulator which has been adopted in the results presented in this paper, unless differently mentioned.

An atmosphere model according to the 1976 Standard US Atmosphere [48] is implemented, as well as the fluorescence yield parameterization [49] and the standard Cherenkov production theory. The LOWTRAN 7 package [50] is embedded into ESAF to simulate the atmospheric transmission. Both Rayleigh and Mie scattering as well as the ozone absorption are taken into account. The presence of clouds is simulated in a parametric way as a uniform layer with predefined optical depth, altitude and thickness. Photon spectral distribution, timing and direction are produced for each step of the shower development (10 g/cm^2). According to such distributions we generate the single photons that are propagated to the instrument depending on the solid angle covered by the telescope pupil. Each of such photons is followed individually and the transmittance is calculated accordingly. No weighting is applied since photons are few and therefore we can afford to perform the calculation of each of them. The optics simulation is performed through a ray trace code developed at RIKEN [51]. Figure 7 shows an example of typical sizes of the optical Point Spread Function (PSF). The images refer to one of the different K-EUSO configurations that have been designed along the years.

For the RIKEN Monte-Carlo simulator and the GEANT4 optics interface [52], the real Fresnel structure is implemented, so photons can be reflected or refracted on the surface of grooves. A cross section drawing of the Mini-EUSO optics with grooves implemented in the "RIKEN simulator" is reported in [18]. In the latter case, the position of the spot on the focal surface is parameterized in an analytical way as a function of the entrance direction. An additional random component of Gaussian shape is added to parameterize the point spread function. An efficiency factor takes into account the transmittance of lenses. In particular, this is the procedure that has been adopted to estimate the performance of POEMMA [38] (see Fig. 3) but it could be applied to any detector.

The Focal Surface (FS) structure (see Fig. 8) is read as a parameter file, where the position and orientation of each single MAPMT is defined. The overall detector efficiency is parameterized at the single pixel level as product of quantum and collection efficiency. The MAPMTs have an average gain set by a parameter and the front-end electronics is treated in a simplified way with a threshold on the current pulse delivered by the MAPMT. The current pulse associated to each photoelectron is varied according to a gaussian distribution.

The background can be added at either the signal from the front-end electronics or to the pixel counts. The electronics simulation is then concluded by the trigger. Several algorithms, specific for each detector, have been implemented in ESAF and can be used in combination. JEM-EUSO, K-EUSO and POEMMA adopt the same trigger scheme on two levels operated on a PDM basis. The first level trigger looks for concentrations of the signal localized in space and time. The second level trigger is activated each time the first level trigger conditions are satisfied and integrates the signal intensity in a sequence of test directions.

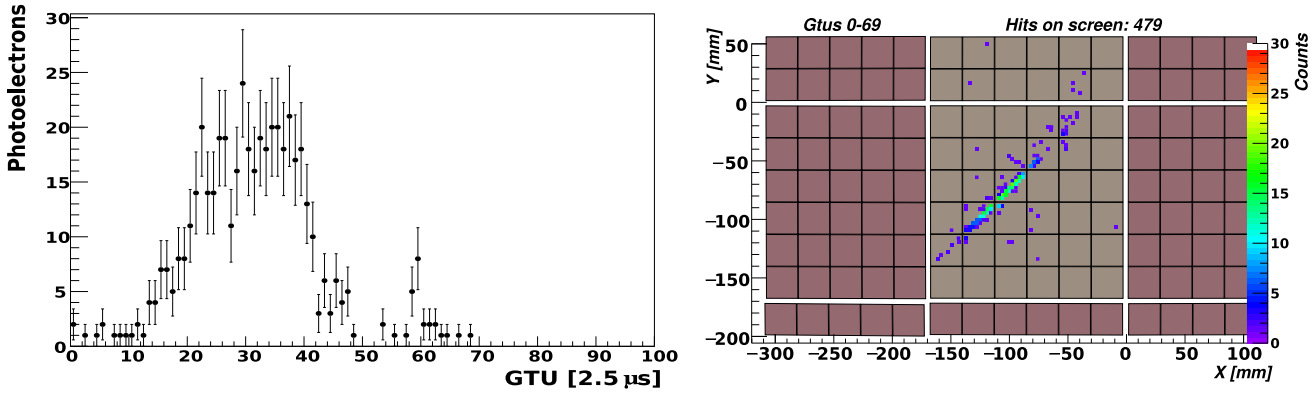

Fig. 8 Simulation of a 10^{20} eV, 60° zenith angle proton event performed for one of the proposed and studied configurations of the K-EUSO detector. On the left, a photoelectron profile at the focal surface is shown. The photoelectron image of the same event on the FS is shown in the right panel

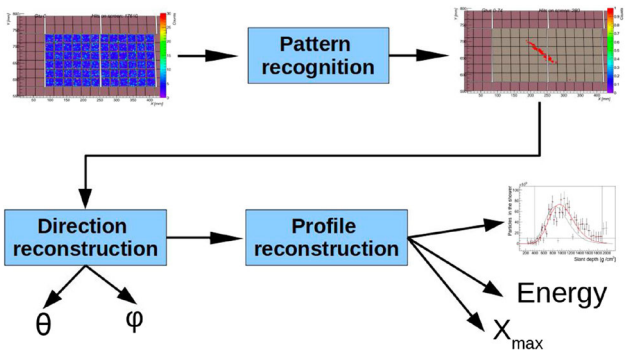

Fig. 9 The general scheme of the reconstruction framework

Directions close to the one of the simulated EAS are expected to have the larger signal over noise ratio (SNR), overcoming, therefore, the preset trigger threshold.

Whenever such condition is met, the second level trigger is issued. The activation of the second level trigger starts the transmission and data storage procedure.

Thresholds are set to have a rate of spurious triggers from background fluctuations at the order of a trigger every few seconds of background simulations at most, to make the rate consistent with the telemetry requirements.

Details of the logic can be found in [34] and in [53] for the first and second levels trigger, respectively. The trigger logic for balloon missions [54] is a modified version of the first level trigger of JEM-EUSO while Mini-EUSO [39] and TUS [17] missions adopt totally different approaches described in Sects. 5.4 and 5.5.

4.2 The EAS reconstruction framework

The first task to accomplish in the reconstruction phase (see Fig. 9) is to identify the signal from the shower in the recorded data.

A number of track recognition algorithms has been implemented in the code. The *PWISE* algorithm [55] searches for high concentrations of the signal on single pixels. The algorithm selects pixels and GTUs in which the signal is above a certain threshold and checks whether this signal excess is persistent over time. The *LTTPatternRecognition* [56] is modeled following the second level trigger philosophy of the JEM-EUSO project. The integration of the signal is performed in a set of predefined test directions and the one which maximizes the integral is chosen to reconstruct the event. Both algorithms exploit the morphology of the signal, which can be seen as a spot of light moving on the focal surface at the projected speed of light.

The next step is the reconstruction of the shower geometry which is an essential step, as it allows the search for anisotropy and provides input required for good energy and X_{max} reconstruction.

The *TrackDirection2* is the angular reconstruction module [57]. Several algorithms are implemented in it but two main families of algorithms are in use; analytical and numerical. In the first group, a fit to the speed of the shower is performed to determine its inclination after the Track Detector Plane (TDP) has been identified.

The inclination of the shower in this plane with respect to the horizontal is inferred from the projected speed of the signal on the focal surface. The algorithms can be used in an iterative way to improve the knowledge of the arrival direction of the shower.

In the numerical approach, a series of test geometries are chosen and the deviations with respect to the timing and arrival direction of the measured event are calculated. The test direction that best describes the measured event properties is taken to be the arrival direction. The so-called Numerical Exact Method 1 has proven to have the best performance and is currently used as default. Such method minimizes the

deviation of the arrival times of the signal from the test shower w.r.t. the data.

The energy reconstruction is performed in the *PmtToShowerReco* module [58]. In this algorithm, the shower profile is reconstructed starting from the signal after correcting for detector effects, atmospheric absorption and fluorescence yield. The shower profile is then fit with a parameterization to obtain the primary particle parameters.

The count profile of the shower is reconstructed by selecting a collection area that follows the cluster of pixels selected by the PWISE or the LTTPatternRecognition. The size of this selection area is a trade-off between the need to collect the highest possible fraction of the signal and the need to limit the background. A stricter selection is indeed more appropriate for the direction reconstruction. For this reason, the PWISE algorithm is more suited for the angular reconstruction, given the typically narrower track selected. On the other hand, the LTTPatternRecognition, with its very wide selection of pixels, is more appropriated for the shower profile reconstruction. The detector modeling allows to take into account the detector efficiency and to retrieve a photon curve at the entrance pupil. The modeling is performed through a series of lookup tables, produced with an extensive Monte-Carlo simulation of the detector response. The arrival direction associated to each pixel is extracted from the very large number of photons simulated. The efficiency of the detector as a function of the arrival direction and on the wavelength can be retrieved then depending on the arrival direction of photons.

The reconstruction currently implemented is designed for the JEM-EUSO mission, which was meant to operate in monocular mode. As such, the method is particularly challenging and has to rely on some iterative procedures. Two methods are described in [59], one with and the other without a Cherenkov reflection peak. The presence of a peak gives a good constraint on the position of $X_{\max}$. The absence of the reflection peak requires using an iterative procedure starting from the reconstructed arrival direction and the parameterized maximum slant depth of a standard shower. Such assumptions are used as starting conditions of an iterative process which minimizes the biases caused by these first choices. Parameters like arrival direction, altitude of the shower maximum and slant depth of the maximum can be varied and the region of the parameter space which best describes the data can be identified. The atmospheric absorption is then modeled according to the LOWTRAN7 package [50] and, after estimating the shower position, the luminosity of the shower can be calculated.

As a final step, a parameterization of the energy distribution of the secondary particles is used to calculate the fluorescence [49] and Cherenkov yields. At the end of the procedure, it is possible to reconstruct the secondary particles profile of the shower.

The reconstruction of energy and $X_{\max}$ is then performed through a fit with a shower profile function to the reconstructed shower profile [59]. A fit with the so called GIL function [42] is adopted. The GIL is a simplified parameterization based on older hadronic interaction models. The difference between GIL and other common descriptions e.g. Gaisser–Hillas is negligible for our application.

4.3 Implementation of other classes of events

The science versatility of experiments like Mini-EUSO and TUS requires the simulation of many different light transients originating from different physical phenomena. For this reason, different types of signals have been included in the capabilities of the ESAF software along the years. In these cases the time profile, the intensity of light emission and the track extension of the event have been included without simulating the physical process responsible for such light emission.

The first class of events implemented in ESAF are Transient Luminous Events (TLEs) such as blue jets, sprites and elves which have been discovered relatively recently and are still not well understood [60]. They have typical durations of ms or tens of ms. Mini-EUSO has a dedicated trigger algorithm to capture TLEs and other millisecond scale phenomena at high resolution [39]. These data could help improve the understanding of the formation mechanisms of filamentary plasma structures, complementing atmospheric science experiments. The TLE simulator in ESAF is composed of the *TLEGenerator, TLELightSource, TLEBunchRadiativeTransfer* classes which are subroutines of the *EventGenerator, LightSource* and *RadiativeTransfer* interfaces respectively. The *TLESpectrumHisto* class is responsible for the spectral distributions of the phenomena.

The left side of Fig. 10 shows a graphical representation of the configurable parameters of the four different classes of events that can be generated in ESAF: (a) a Toy Model; (b) Blue Jet; (c) Sprite; (d) Elves.

The right side of Fig. 10 shows examples of typical TLEs as they are simulated for Mini-EUSO. The simulations employ toy models which in a simplified way reproduce the size, shape and wavelength spectra of the different physical phenomena. Details of the implementation of these phenomena in ESAF can be found in [62].

Among the scientific objectives of the JEM-EUSO program is the study of slower events such as meteors and fireballs. The simulation of meteor-induced light tracks is described in [63], which inherits the approach described in [64]. Similarly to the TLE case, a new class has been developed for meteors called *MeteorLightSource*. Meteors produce tracks which are very slow moving compared to UHECR events, resulting in more than 1000 times more data produced than for UHECR events. The solution that has been adopted is to fully track only a fraction of the produced pho-

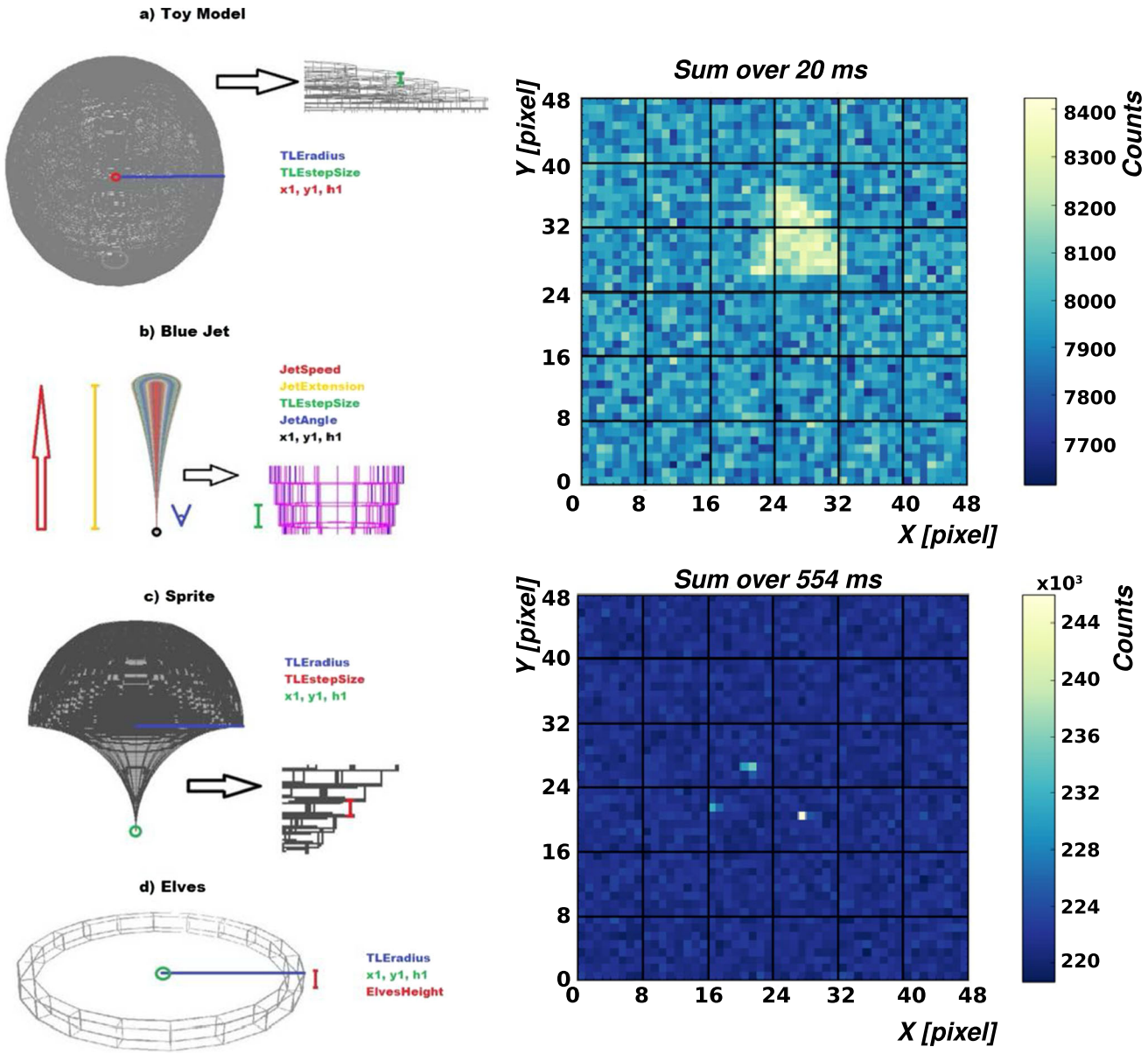

Fig. 10 Left: Graphical representation of the configurable parameters of the four different classes of events that can be generated in ESAF: **a** a Toy Model; **b** Blue Jet; **c** Sprite; **d** Elves. Right: Expected light track of a typical diffused elve (top) and 3 localized blue jet events (bottom) generated by ESAF and detectable by Mini-EUSO. Background emission of 1 count/pixel/GTU is also included. Right plot adapted from [61]

tons and to re-weight them at the detector level. Regarding the simulation of the light signal of the meteor, the starting position, direction, speed, duration and magnitude can be chosen randomly or set as input parameters. The variation of the brightness of the meteor as a function of time, or the meteor lightcurve, is also chosen randomly, or provided as an input. Since the shape of the lightcurve can be highly variable in the real world, the model adopts a very flexible approach, representing it with a 9th degree polynomial. In most practical applications performed so far, simulated lightcurves look reasonably realistic, taking into account the large intrinsic variability of the phenomenon, as shown, for instance, in the analysis by [65]. Moreover, since it is known that real meteors can exhibit one or more secondary bursts, the model includes the possibility to simulate one secondary burst, occurring at some instant before the end of the event, and having a morphology which is also represented by a 9th degree polynomial (again, fixed or randomly chosen). Moreover, ESAF now also includes the implementation of a formula by Jacchia [66] which links the magnitude, mass and the velocity of

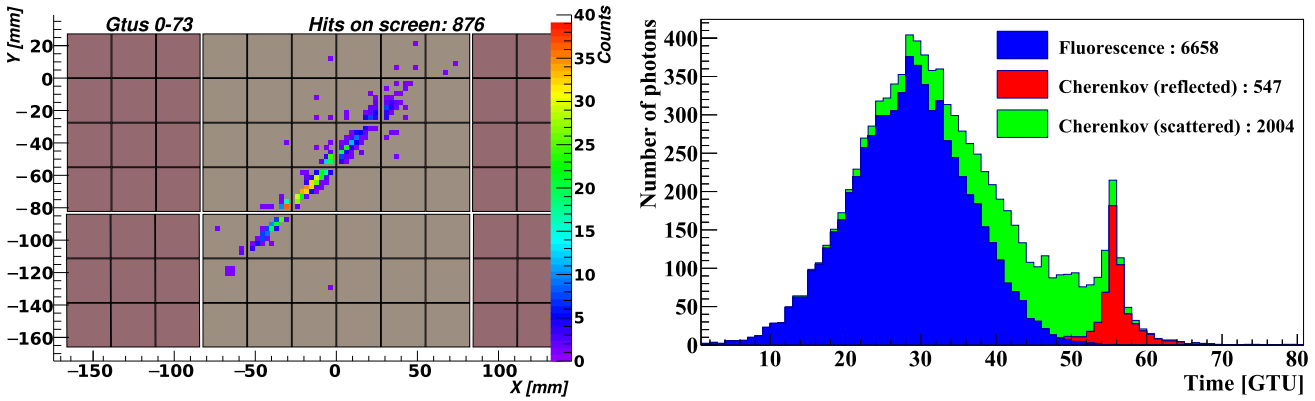

Fig. 11 Left: Spatial profile of photon counts from an EAS caused by a 10^{20} eV proton with zenith angle 60°. Each square (dark and light brown) represents a MAPMT. Parts of 6 PDMs are shown. The small coloured squares show the number of photon counts detected by each channel of the MAPMT. This event is crossing two PDMs, with the shower starting to develop in the bottom central PDM and continuing in the top central PDM. Right: Time profile of photons, obtained adding all photons of the previous picture detected on each GTU of 2.5 μs (∼ 80 GTUs for a total signal duration of ∼ 200 μs). It is possible to see the contribution to the signal from the three components: the UV fluorescence light (blue), scattered Cherenkov (green) and Cherenkov diffusely reflected peak (red)

the meteoroid. Given the meteor's velocity and magnitude, that are free parameters in the simulations, one can derive the corresponding mass of the meteoroid. By assuming a value of the density ρ (so far a fixed value $\rho = 3.55$ g/cm^3 has been assumed in preliminary tests) it is possible to compute the corresponding size of the meteoroid. More details about the simulation of meteors for JEM-EUSO, Mini-EUSO and EUSO-TA can be found in [67], while an example of a simulated meteor with ESAF is reported in Sect. 5.5.

5 Simulation of various missions of the JEM-EUSO program and derived performance

The complexity of the JEM-EUSO program requires an extensive effort to study the performance of all different detectors of the program. The detectors are either space-based, like JEM-EUSO, Mini-EUSO, TUS, K-EUSO, and POEMMA or balloon based, like EUSO-Balloon, EUSO-SPB1 and EUSO-SPB2. EUSO-TA is the only one located on ground. EUSO-SPB2 is not implemented yet in ESAF in the final configuration and can be simulated only using the OffLine package. For this reason it will not be discussed in detail in this paper.

All the detectors point normally in nadir mode or with slightly tilted configurations, except for EUSO-TA which points northwest with an elevation typically of 15–25°. All the detectors have different focal surfaces: Mini-EUSO, EUSO-TA, EUSO-Balloon and EUSO-SPB1 are single-PDMs detectors while JEM-EUSO, POEMMA and K-EUSO have a multi-PDM layout. TUS on the other hand, consists of an array of 256 PMTs on a square of 16 × 16 PMTs. The time frame adopted in the simulations is 2.5 μs with the exception of TUS, which has a frame of 0.8 μs and a totally different electronics configuration. In the following subsections, the main simulation results for each configuration are summarized starting from the JEM-EUSO case, which has been studied more extensively than other configurations. The description of the standard parameters adopted in the simulations is reported in Appendix B. This section includes information which has already been the subject of previous publications.

5.1 The JEM-EUSO configuration

JEM-EUSO has been conceived as a mission to be installed on the ISS orbiting at ∼ 400 km height. The main characteristics of the telescope are summarized in Sect. 1. Figure 11 shows the spatial and temporal profile of an EAS generated by a 10^{20} eV proton with zenith angle 60° simulated with ESAF. The contribution of the fluorescence and Cherenkov components at the pupil level are indicated on the right in different colors.

The optics and detector response are then simulated and Fig. 12 shows the photons arriving at the detector (blue), the photons arriving at the focal surface (FS, red) and the photons detected at pixel level (Detected, green).

By applying the trigger algorithm after introducing the nightglow background, the geometrical aperture is determined in nadir mode. A tilted configuration of the telescope is available in ESAF as well. In the tilt mode, the observation area is scaled by $\propto \sec^3(\xi)$ as a function of tilting angle ξ of the optical axis from the nadir. This increases the sample of events at the highest energies, however, showers will be seen at larger distances, therefore they will appear dimmer compared to nadir mode.

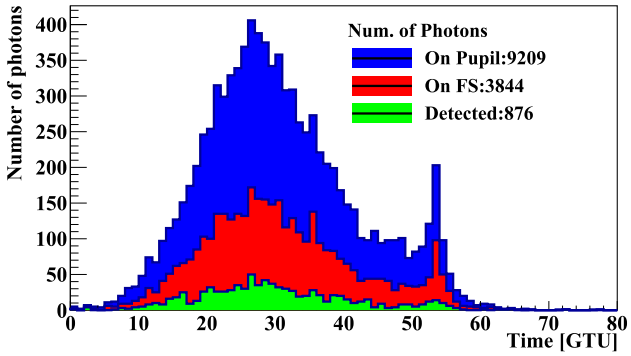

Fig. 12 Photons coming to the detector, photons intersecting the focal surface (FS) and photons detected as a function of time (in GTU). Due to the covering factor and quantum efficiency taken into account, the fraction of photons creating a signal ('Detected') is about 0.3. In this example: 10^{20} eV proton event with 60° zenith angle

In order to estimate the aperture, a specific nightglow emission has to be assumed. A background level (I_{BG}) of 500 photons/(m^2·sr·ns) is considered. This is a typically measured value according to literature [68–70], and it represents also the value assumed in earlier JEM-EUSO simulations. This corresponds to an average count level of $\sim$ 1.1 counts/GTU/pixel. The assumption of a constant background over the entire FoV, most likely, is an overly simplistic assumption since the background radiance depends on the tilting angle under which the atmosphere is observed. However, at a first-order approximation and especially for low tilting angles we can consider the shower-to-detector distance to be the leading factor affecting the threshold in energy. Figure 13 shows the exposure as a function of energy for nadir and different tilting angles. As expected by tilting the telescope, both the threshold energy and exposure increase at the highest energies.

The quasi-nadir configuration of $\xi = 20°$ allows keeping at the lowest energies an almost similar exposure to the nadir configuration, while increasing it moderately at $\sim$ 10−20% level in the $E \gtrsim 10^{20}$ eV.

Compared to nadir mode, the tilted mode is suitable to increase the exposure at energies $E \gtrsim 2 \times 10^{20}$ eV, where the flux is particularly low. The exposure calculation is based on a Monte Carlo simulation of proton EASs of variable energy and direction. To avoid border effects, cosmic rays are injected in an area A_{simu} larger than the FoV. The ratio of the triggered N_{trigg} over simulated N_{simu} events is then calculated for each energy bin. The effects of day-night cycle and Moon phases are taken into account in η, the astronomical duty cycle. Effects of clouds and artificial lights are also taken into account by η_{clouds} (see later on in this section) and η_{city}, respectively. In this formula, we assumed $\eta = 0.2$, $\eta_{clouds} = 0.72$ and $\eta_{city} = 0.9$ (which includes also lightning and aurorae contributions) as estimated in [10]. The exposure $\mathcal{E}(E)$ is then calculated over time t, which is assumed to be 1 year in the following:

$$\mathcal{E}(E) = \frac{N_{trigg}}{N_{simu}}(E) \times A_{simu} \times \Omega \times \eta \times \eta_{clouds} \times \eta_{city} \times t. \tag{1}$$

An overall conversion factor between geometrical aperture and exposure of $\sim$ 13% is obtained as a product of $\eta \times \eta_{clouds} \times \eta_{city}$.

As ESAF provides the opportunity to simulate the presence of clouds, extensive simulations have been conducted to understand their impact on the aperture reduction and reconstruction capabilities. Figure 14 shows the light curves of EAS with different atmospheric conditions for the case of proton EASs with $E = 10^{20}$ eV and $\theta = 60°$. The solid line represents the case for clear atmosphere. Dashed and dotted lines show the cases for clouds optical depth $\tau_C = 1$ at height $H_C = 3$ km and $\tau_C = 0.5$ at $H_C = 10$ km, respectively. The horizontal axis is the absolute time in GTUs. The axis on the top indicates the altitude where photons originate for the given arrival time. In the clear atmosphere condition, the light curve indicates the EAS development followed by the Cherenkov footprint reflectively diffused by the Earth's surface at GTU number 100. For $\theta = 60°$ as in this example, the

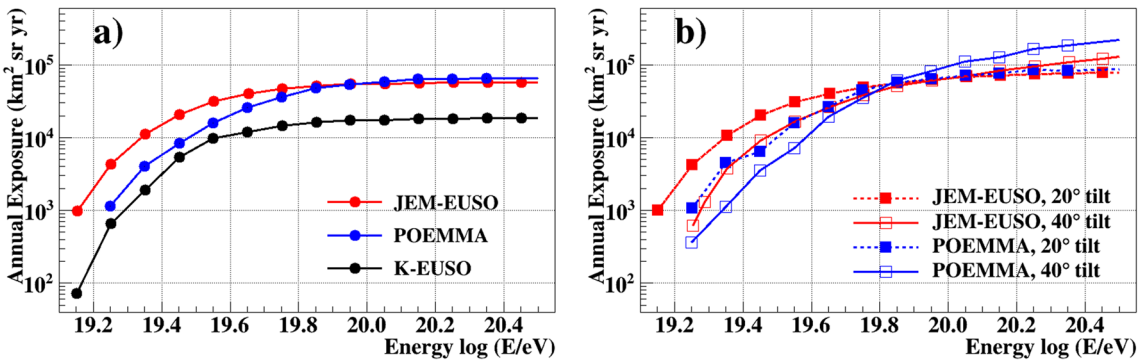

Fig. 13 JEM-EUSO, K-EUSO and POEMMA exposures as a function of energy for nadir (left) and different tilting angles (right). In case of K-EUSO only the nadir configuration has been simulated as the tilt option is not considered in the present mission design

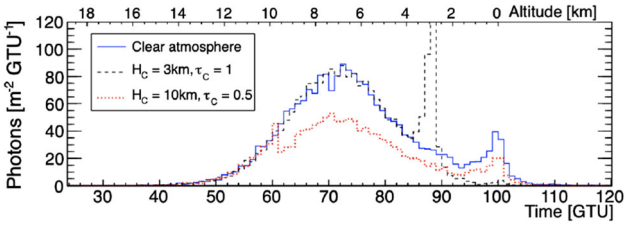

Fig. 14 Arrival time distribution of photons from a proton induced EAS of $E_0 = 10^{20}$ eV and $\theta = 60°$ for different atmospheric conditions. The solid line represents the case for the clear atmosphere. Dashed and dotted lines denote the cloudy cases for optical depth $\tau_C = 1$ at cloud height $H_C = 3$ km and $\tau_C = 0.5$ at $H_C = 10$ km, respectively. The axis on the top indicates the altitude where photons originate for the given arrival time. The photon number is indicated per m^2. In order to compare to the Fig. 12 the reader has to multiply by the optics size (~ 4.5 m^2). Also the starting time of the event is different because it depends on the first photon reaching the optics, however, the duration of the event in both cases is 55–60 GTU in clear sky atmosphere. Image adapted from [71]

apparent shower development lasts ~ 60 GTUs ($= 150$ μs). Using these data, the EAS parameters are reconstructed.

In presence of clouds, EAS light curves are affected. If the optical depth of the cloud is large enough, the shower track is truncated. Upward photons scattered or emitted below the cloud are extinguished and do not contribute to the signals at the telescope. For this example, with a cloud at 3 km, the apparent signals last 40 GTUs. It is still feasible to apply the reconstruction techniques used in the case of the clear atmosphere by using only the measurements taken above the cloud. As seen in the figure for the case of a small optical depth, photon signals originating below the cloud are attenuated. This likely lowers the estimated energy of the EAS if the same techniques for the clear atmosphere are applied. Alternatively, the Cherenkov footprint is still observable and the orientation and apparent velocity are not affected, thus the consequence on arrival direction determination is limited. As described in [71] using of ESAF simulations of EASs in variable cloudy conditions together with the analyses of satellite measurements of the cloud distribution indicate that more than 60% of the cases allow for conventional EAS observation, while an additional $\sim$ 20% can be observed with reduced quality. The combination of the relevant factors results in an effective trigger aperture of $\sim$ 72% of the aperture in clear atmosphere condition.

The scientific outputs of such a mission rely on the quality of the reconstructed EAS parameters. Therefore, the performance on angular, energy and $X_{\max}$ reconstruction have been extensively studied for the JEM-EUSO telescope using different configurations, namely the HTV and Dragon layouts, nadir and tilt options. The study presented in the following adopts either the SLAST-GIL shower generator or CONEX with EPOS-LHC [72] hadronic interaction model. While SLAST-GIL has the advantage of considerably reducing the simulation time, it adopts a simplified approach based on a parameterized shower simulation in which shower-to-shower fluctuations are not completely taken into account. This is not an issue in specific studies such as the aperture curve determination, however, it might have a more significant impact in case of reconstruction of EAS parameters. Another advantage of using the CONEX simulation program is that it is possible to study the behavior of the detector response to different primary particles. In the following we report on proton, iron and photon studies.

In Fig. 15 we present the angular resolution in nadir mode for proton, iron and photon-generated EAS obtained with the Dragon configuration and adopting the CONEX generator. For proton and iron we have simulated events with energies of 5×10^{19} eV and 10^{20} eV with zenith angles of $\theta = 30°$, 45°, 60°, and 75°. For each angle and energy combination, 1000 events are simulated. Additionally, similar simulations have been performed for photons at the energy 10^{20} eV. Due to possible interactions with the geomagnetic field, special care has to be taken when performing the photon simulations. The pair production process depends strongly on the magnetic component transverse to the photon's direction of motion, and, therefore, the event simulation is sensitive to the value and direction of the local geomagnetic field [73]. We characterize the error in the reconstructed arrival direction as the angle between the simulated arrival direction vector $\hat{\Omega}_{\text{Simu}}$ and its reconstructed counterpart $\hat{\Omega}_{\text{Reco}}$. We define $\gamma = \arccos(\hat{\Omega}_{\text{Simu}} \cdot \hat{\Omega}_{\text{Reco}})$ as the error in the reconstruction, and the angular resolution as the value where the cumulative distribution of the reconstruction's error reaches 68%. We shall refer to this value as γ_{68}.

The results using the Dragon option indicate that the angular resolution of the detector is not affected too much from the larger fluctuations of the proton-induced showers as the iron induced EASs have similar reconstruction performance. Figure 15 displays also results obtained with the HTV configuration which have been studied in [57]. The better performance of the Dragon option compared to the HTV option is mainly due to stricter cuts applied in the selection performed with the PWISE algorithm particularly visible in the significant improvement obtained for protons at 30°. However, this comparison shows the possibility to improve the quality of the reconstructed events by applying more stringent cuts at the price of a reduced statistics ($\sim$ 50% at 30°). In a real experiment all the triggering events will be reconstructed with coarser selection cuts. A series of refinements will allow high quality events to be reconstructed with higher performance still keeping the high statistics. The event selection and reconstruction strategy is still in definition. In the case of photons as primary particle we experience a low triggering ratio for the showers that exhibit a strong Landau–Pomeranchuk–Migdal (LPM) effect [74,75]. Showers with the LPM effect appear less bright, as a consequence of their

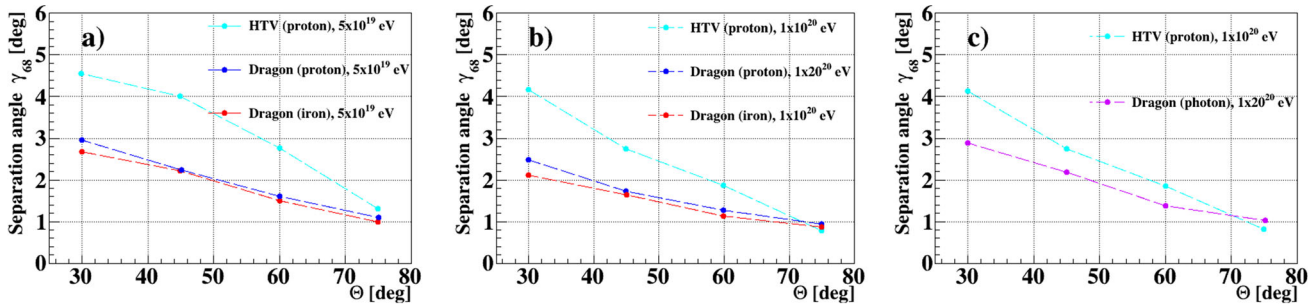

Fig. 15 The angular resolution as a function of the zenith angle for the Dragon-configuration of the JEM-EUSO mission pointing to nadir for proton (dark blue) and iron (red) primaries with an energy of 5×10^{19} eV (**a**), and 10^{20} eV (**b**). Panel **c** shows in violet the angular resolution for photons of 10^{20} eV. Previous results with the HTV-configuration are also shown in light blue. Image adapted from [11]

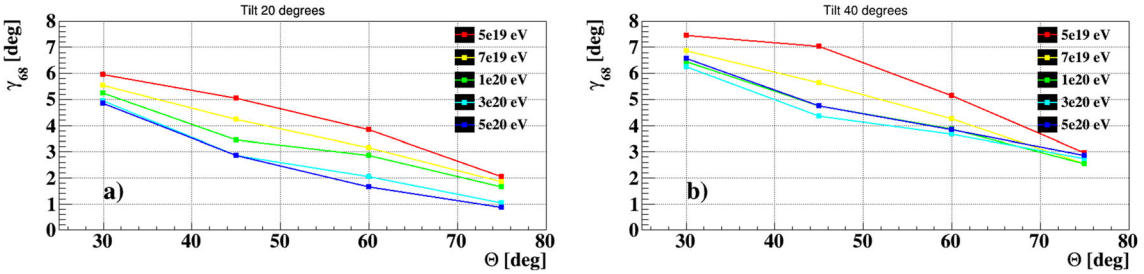

Fig. 16 The angular resolution of the 20° (**a**) and 40° (**b**) tilted JEM-EUSO telescope. Image adapted from [76]

extended longitudinal profile. It works as a selection filter allowing only the brightest photon showers to trigger the detector. Again this is mostly relevant at the lower zenith angles, whereas for higher zenith angles the impact is less dramatic. A more detailed discussion of this analysis can be found in [11].

The angular resolution is studied also for configurations in tilt mode with the Dragon option in case of proton showers [76]. The standard procedure described in [57] is applied here. EASs are generated using the SLAST-GIL simulator with fixed energies between 5×10^{19} eV and 5×10^{20} eV and fixed zenith angles between 30° and 75°. All azimuth angles are picked randomly between 0° and 360°. The shower cores have been placed within a rectangular area of x[−550 km; +100 km] × y[−250 km; +250 km] for $\xi = 20°$ tilt angle and x[−1300 km; 0 km] × y[−400 km; +400 km] for $\xi = 40°$. These areas are considerably larger than the actual FoV of the tilted instrument. For each energy/zenith angle combination the number of triggering events is of the order of 2000 or higher.

Results are presented in Fig. 16. As expected, the angular resolution of the telescope tilted by $\xi = 20°$ gets worse by approximately 2.5° when compared to the nadir mode operation (see Fig. 15). The effect mainly depends on the zenith angle of the showers and to a smaller extent on the energy. Especially the low zenith angles are affected. When we tilt the telescope by $\xi = 40°$, the resolution gets worse compared to the previous 20° case. Again, the effect mainly depends on the zenith angle of the showers and to a smaller extent on the energy. The loss of the angular resolution is about 1.5° compared to the $\xi = 20°$ tilted case. As expected from the analysis of the signal behaviour, we can observe a worsening of the angular resolution due to the fact that less light per EAS reaches the telescope. The instrument resolution capability is determined by four limiting factors, three of which are related to the distance of the shower from the detector. The first one is the proximity effect. Events injected nearby the telescope appear brighter than those farther away, since the number of photons reaching the telescope is scaled by a factor of $1/d^2$, where d represents the distance between the telescope and the location of the emitted photon. The second comes from the projected pixel size on ground as it determines the minimum theoretically reachable air shower resolution of the telescope. Pixels in the outer parts of the FoV observe a larger volume of air than the ones at the centre. The third one is due to optics throughput. Events occurring in the outer parts of the FoV face stronger optical losses, due to a lower transmittance of the optical system. The probability of being attenuated or defocused by the telescope optics is higher. The last one is related to the skimming effect. Shower tracks can skim the field of view and appear only partially on the FS. This effect increases when the nadir FoV is deformed by tilting the detector.

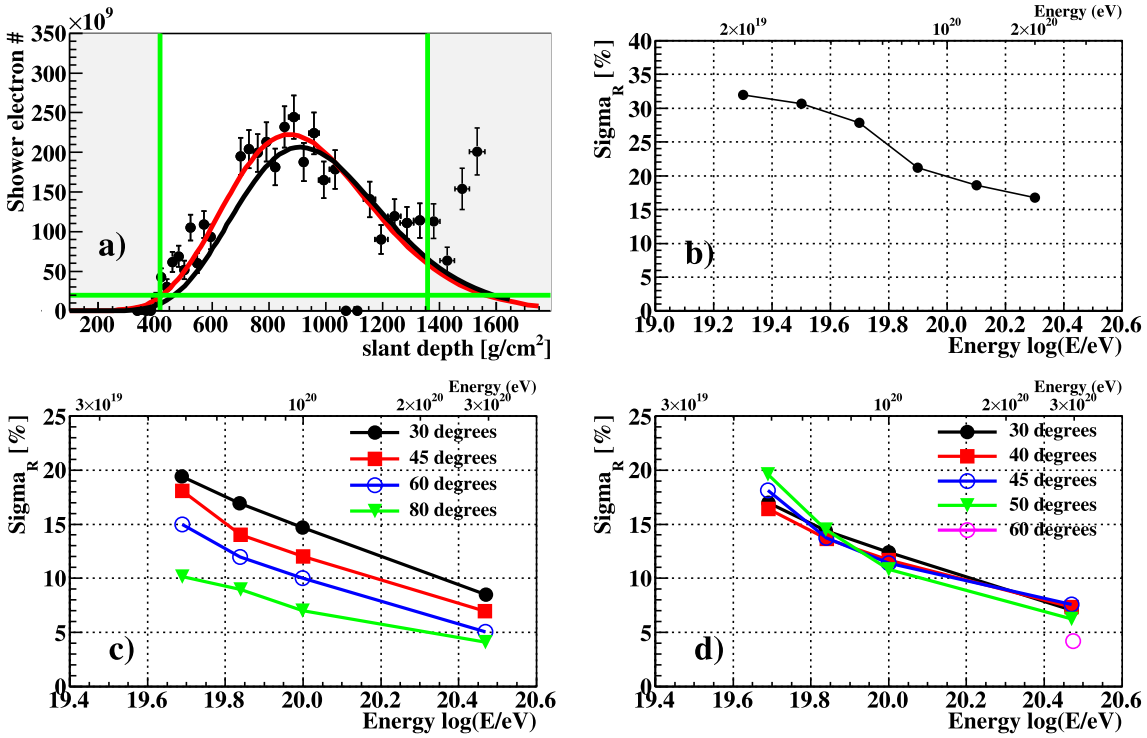

Fig. 17 Panel **a**: The simulated (black line) and reconstructed (points) shower electron curve. The GIL fit is shown as a red line. The simulated proton event has an energy of 3×10^{20} eV, a zenith angle of 50° and an X_{max} of 915 g cm^{-2}. The reconstructed parameters for this fit are 3.2×10^{20} eV and 873 g cm^{-2}. The χ^2/**DOF** of this event is 0.905. The shaded areas show the points which are excluded from the fit. Panel **b**: The energy reconstruction performance is shown here for the all-event sample extracted on the full FoV (±270, ±200) km and energy range 2×10^{19}–2×10^{20} eV. The sample with cuts DOF > 4, χ^2/Ndf < 3 is shown here. Panel **c**: The energy resolution in terms of the σ_R factor (see text for details), in percent, is shown. Here, we plot the results for various zenith angles and energies. All the events are impacting in the central part of the field of view (namely in the inner (±20, ±20) km). The geometry has been reconstructed with the slant depth method. Panel **d**: Same as in **c** but adopting the Cherenkov method. Image adapted from [59,77]

The question whether or not to tilt a JEM-EUSO-like instrument in space strongly depends on the primary objective of the mission. When the emphasis is put on high exposure for the highest energy events, a tilting of the instrument might be useful. When the focus lies on accuracy for direction determination, the nadir mode is the preferred operation mode.

Similar studies have been conducted also in regards to the energy and $X_{\max}$ resolutions. We report here those performed for the HTV configuration in nadir mode adopting the SLAST-GIL shower generator [59], as they were conducted in a more detailed way. This is the standard procedure adopted also for similar studies conducted with POEMMA and K-EUSO. An analysis using different primaries (p, Fe and photons) and using CONEX shower simulator can be found in [11]. After the retrieval of the signal identified by the pattern recognition we start the correction of the inefficiencies of the detector and of the absorption in atmosphere and compute an estimate of the fluorescence yield. The reconstruction of the geometry is done following either of two methods: the slant depth or the Cherenkov method. As final result we obtain a shower profile which we will fit with some predefined shower function. In this way we obtain the energy and $X_{\max}$ of the shower. An example of the reconstructed profile with the related fit is shown in Fig. 17a. This event has an energy of 3×10^{20} eV and a reconstructed energy of 3.2×10^{20} eV. We see the Cherenkov reflection peak in the right part of the profile.

Using the reconstruction procedure discussed in the previous section, a study of the energy resolution of the JEM-EUSO mission has been performed. The impact point is selected in the central part of the field of view (namely in the inner (±20, ±20) km). Showers are generated according to the GIL parameterization. We simulated 8000 events for each point and we applied quality cuts DOF > 4, χ^2/DOF < 3 on all the data. The cut on the degrees of freedom implies a minimum number of 7 points to be fit. Such a cut is a minimal requirement to ensure that events with too much light loss because of gaps are rejected. The cut on the χ^2 rejects instead the catastrophically failing fits. Under such conditions more than 80% of the events above 10^{20} eV are selected.

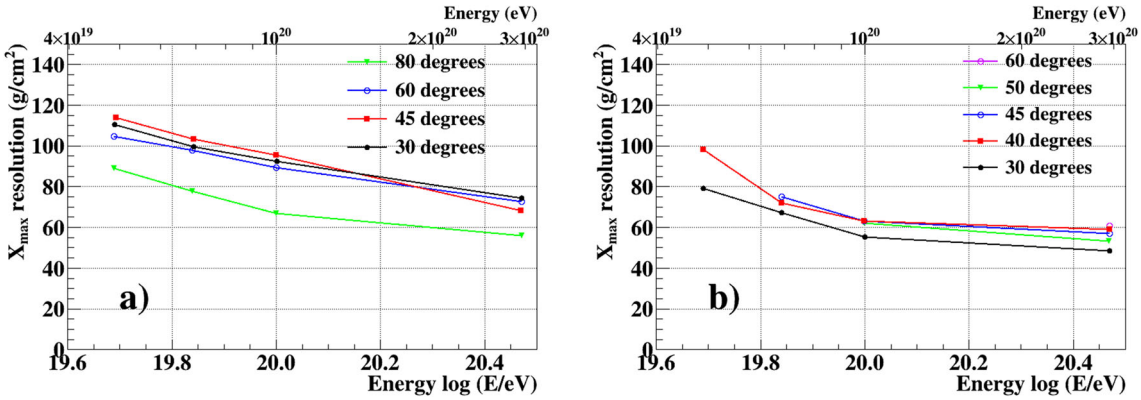

Fig. 18 The X_{max} resolution is shown for various zenith angles and energies of proton events. All the events are impacting in the central part of the field of view (namely in the inner ($\pm 20, \pm 20$) km). The geometry has been reconstructed with the slant depth method in panel **a** and with the Cherenkov method in panel **b**. For the lowest energy bin the reconstruction procedure adopting the Cherenkov method very often fails due to lack of signal, therefore, it can not be applied. Image adapted from [77]

To estimate the resolution, we define the parameter R for each event as:

$$R = \frac{E_{\text{reco}} - E_{\text{real}}}{E_{\text{real}}}. \tag{2}$$

The distribution of parameter (2) for all the events which survived the cuts has then been fitted with a Gaussian curve. The σ_R parameter of such Gaussian fit is reported in panels (b), (c) and (d) of Fig. 17. As can be seen in Fig. 17c, the energy resolution tends to improve toward the higher zenith angles and with the increasing energy due to the better quality of the signal. Generally, the slant depth method will always have a resolution under 20%. At the most extreme energies, the resolution reaches 10% or even lower. In Fig. 17d, the energy resolution obtained with the Cherenkov method is shown. Again, the highest energies allow the best performance, while a clear improvement depending on the zenith angle cannot be seen anymore. This is due to the worsening quality of the Cherenkov peak at the highest zenith angles. In fact, the Cherenkov peak will be much more difficult to recognize at large zenith angles due to the larger spread of the reflection spot. In Fig. 17b the energy resolution, estimated using the slant depth method, is shown for events distributed in the range ($\pm 270, \pm 200$) km and for energies in the range 2×10^{19}–2×10^{20} eV. The events have zenith angles between 0° and 90° distributed as $\sin(2{\cdot}\theta)$. Here, we also apply DOF > 4, χ^2/DOF < 3 quality cuts on $\sim 10^4$ events. The resolution ranges from $\sim 30\%$ at 2×10^{19} eV to 15–20% at $\sim 10^{20}$ eV. Systematics have not been corrected and may still be contributing to the distribution width.

A similar study has been performed for the X_{max} parameter. Using the same samples generated for the study of the energy resolution, we have calculated the distribution of the slant depth of the maximum. Figure 18 shows the JEM-EUSO X_{max} resolution for fixed conditions of zenith angle and energy. Similarly to the case for the energy, we evaluate the parameter $X_{\text{max}}^{\text{reco}} - X_{\text{max}}^{\text{real}}$ for all the events. Then we fit the distribution with a Gaussian and we plot the σ parameter. Figure 18a displays the reconstruction performance for the slant depth method. As can be seen, the X_{max} resolution improves with the energy. At the lowest energies, it ranges from 90 to 120 g cm^{-2} while at the highest energies, from 60 to 80 g cm^{-2}. The higher zenith angles also yields better resolution, due to the better angular resolution. Moreover, the higher altitude of such events implies higher luminosity at the detector. The complete profile can be totally fitted not being cut by the ground impact. Figure 18b, shows the same plot obtained with the Cherenkov method. In this case the performance is significantly better ranging from 80–100 g cm^{-2} at the lowest energies to 50–60 g cm^{-2} at the highest ones. At the highest zenith angles the Cherenkov reflection peak will however not be recognizable. For this reason, the plots will not extend above 60°. We reiterate that at these energies the difference between p and Fe X_{max} is of the order of 100 g cm^{-2} [78,79].

Comparable results have been obtained on the resolution of the X_{max} distributions using the CONEX simulator for either proton or iron showers, and slightly larger resolution for photon showers in all three cases distributed within the full FoV. However, an offset in Xmax was observed in this case indicating a need for a fine tuning of the reconstruction algorithms. Despite the fact that on a single event the uncertainty on X_{max} is large, by collecting a large sample the uncertainty on the average value will reduce significantly (in principle by a factor of 10 with a statistics of 100 events, under the condition of purely statistical errors). This allows obtaining meaningful results in terms of the evolution of the average mass composition as a function of energy at energies

Table 2 Angular, energy and $X_{\max}$ resolutions of the K-EUSO detector for proton EASs of different energies and zenith angles. The angular and energy estimations are done at fixed angles and full FoV while in case of $X_{\max}$ they are performed at one single angle (30°) and refer to the center of the FoV

Energy	Energy res. (%)				Angular res. (°)				$X_{\max}$ res.
[EeV]	30°	45°	60°	75°	30°	45°	60°	75°	[g/cm^2] 30°
50	25	25	22	16	6.8	6.8	4.0	1.6	110
70	27	24	20	14	5.6	4.6	3.0	1.6	83
100	27	24	20	13	4.8	3.0	2.0	1.0	69
300	21	16	13	7	4.2	1.6	1.0	0.63	41

which are not reachable yet by ground-based experiments due to the limited duty cycle and relative exposure.

5.2 The K-EUSO configuration

We present in the following the performance results in terms of aperture, exposure, angular, energy and X_{max} resolutions obtained adopting the latest configuration designed for the K-EUSO mission as reported in Sect. 2.

For this purpose, N = 4500 showers were simulated in the energy range E = 10^{19} eV – 3×10^{20} eV, from all directions uniformly in azimuth and with $\sin(2\theta)$ zenith dependence in the entire field of view of the detector. The yearly exposure as a function of energy is shown in Fig. 13. As it can be seen, at the plateau, which is reached at around 10^{20} eV, K-EUSO achieves an exposure of $\sim$ 18,000 km^2 sr yr. The 50% efficiency is reached at $\sim 4 \times 10^{19}$ eV. Assuming the spectrum recently published by the Auger collaboration [1], the expected rate of triggered events has been calculated to be of the order of 4 events/year above 10^{20} eV and 65 events/year above 5×10^{19} eV.

As discussed in [19], and shown in Table 2 by adopting the so called Numerical Exact 1 method [57], K-EUSO achieves an angular resolution between 3° to 7° at small zenith angles and improves to 1°–2° for nearly-horizontal events in the energy range between 5×10^{19} and 3×10^{20} eV. There is a clear improvement trend as the energy increases.

Estimations of the energy resolution of K-EUSO for UHECRs with different energies arriving at various zenith angles are shown in Table 2. Similarly to the analysis related to the angular resolution, 2500 showers were simulated at fixed energies and zenith angles, both for the center and for the full FoV of the detector. The resolution was estimated as the standard deviation of the R distribution as shown in the previous section. It can be seen that the energy resolution is around 25% at low zenith angles and improves to around 15% for nearly horizontal events, with a small improvement for higher energies. No significant improvement of the performance has been observed if events are simulated on the central part of the FoV.

Reconstruction of the $X_{\max}$ of an EAS is also performed according to [59] and is obtained from the fit of the reconstructed shower profile. In this work, we only show a few examples of the reconstruction performance obtained in some specific condition. The method we use here considers only events with a visible Cherenkov reflection peak. In this way, the impact point of the shower can be identified in the profile and therefore a clear constraint can be put onto the shower geometry. An overview of the performance in few conditions is given in Table 2. The resolution is always around 50–90 g/cm^2 for the center while similar values are obtained for the whole FoV.

These results have to be regarded as a first indication of the performance. Improvements will be possible when the K-EUSO design is frozen and the algorithms will be optimized for this specific configuration.

Figure 19 shows a comparison between JEM-EUSO, K-EUSO and POEMMA performance in terms of angular and energy resolutions at 10^{20} eV for different zenith angles.

5.3 The POEMMA configuration

A first estimation of POEMMA performance in terms of trigger exposure and quality of event reconstruction has been assessed using the ESAF code assuming a clear atmosphere (details can be found in [38]). Because the POEMMA PFC baseline design employs the PDMs and electronics developed for the JEM-EUSO mission, the JEM-EUSO trigger algorithms and reconstruction procedures have been considered to evaluate the POEMMA performance. Proton showers have been simulated using the SLANT-GIL shower generator. The POEMMA optics response was implemented in ESAF using the parametric model. ESAF doesn't allow yet a stereoscopic vision, therefore, monocular mode performance has been determined at first and then extrapolated to the stereoscopic view for what concerns the energy resolution. Instead an independent approach (as detailed in [38]) has been adopted for the estimation of the angular and Xmax resolutions in stereo mode. The simulations were performed assuming a standard UV night glow background level of 500 photons m^{-2} ns^{-1} sr^{-1} in the 300–500 nm band. Taking into

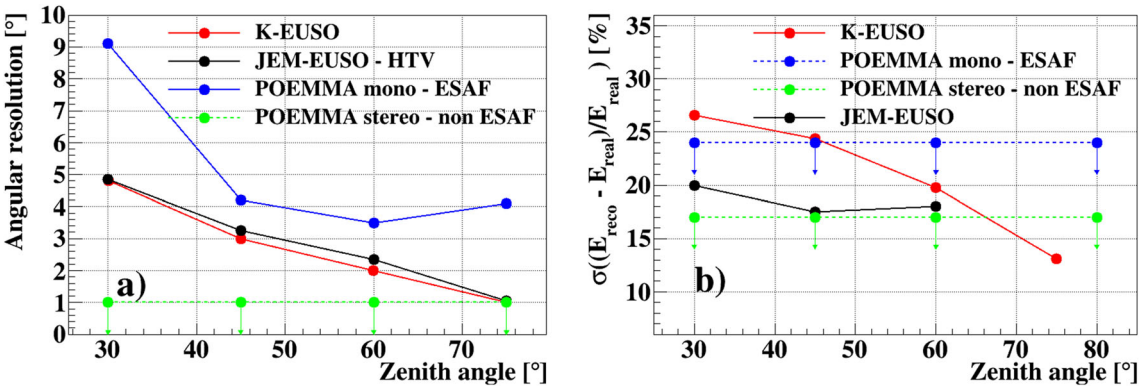

Fig. 19 Comparison between JEM-EUSO, K-EUSO and POEMMA performance in terms of angular (panel **a**) and energy (panel **b**) resolutions for 10^{20} eV proton EASs with different zenith angles. The POEMMA angular resolution in stereo mode is obtained without the use of ESAF, as it implies a stereoscopic vision, while the energy resolution has been extrapolated from the monocular mode derived with ESAF. The dashed lines represent the result of the cumulative resolution obtained for all theta angles. The better performance of JEM-EUSO is due to the smaller pixel footprint at ground and by a dedicated optimization of the reconstruction algorithms. POEMMA and K-EUSO adopted the same algorithms developed for JEM-EUSO with only limited optimizations. Moreover, in case of POEMMA a parametric simulation of the optics has been considered instead of a ray-tracing code. The comparison between JEM-EUSO and POEMMA shows also the margin of improvement which is in principle obtainable with a dedicated fine tuning of the reconstruction algorithms. At the same time the significant improvement of a stereoscopic configuration is clear when the mono and stereo performance of POEMMA are compared

account the POEMMA detector response, this corresponds to an average equivalent count rate of 1.54 counts μs^{-1} pixel^{-1}. The study presented here assumes a 2.5 μs GTU, used as reference for the different projects. Preliminary tests using the independent approach discussed in [38], with short time resolution indicate a significant impact on the angular and X_{max} resolutions, while negligible on the energy resolution. For this reason the stereo reconstruction adopted the 1 μs GTU while for the monocular mode studies the 2.5 μs resolution was considered. The present results have, therefore, to be considered conservative, in terms of POEMMA performance. In Fig. 20 we show the photoelectron (left) and track profile (right) on the PFC focal plane induced by a proton EAS of 10^{20} eV, inclined 60° from the nadir.

To estimate the exposure curve of POEMMA, an overall set of 20,000 proton EASs was simulated with ESAF in the energy range 5×10^{18} eV–5×10^{20} eV uniformly in azimuth and with the same zenith dependence as in K-EUSO simulations over a sampling area that is almost twice the size of that in the FoV ($S_{FoV} \sim 145{,}000$ km^2). The exposure $\mathcal{E}(E)$ was then determined using Eq. (1) under similar assumptions. In case of POEMMA only the first level trigger was applied. Based on JEM-EUSO simulations, it was estimated that the effect of the second level trigger is to increase the exposure curve by $\sim$ 10% at higher energies. The exposure was estimated also for different tilt angles as shown in Fig. 13. The annual exposure in monocular mode reaches $\sim 70{,}000$ km^2 yr sr, while it reduces by about a factor of two if the stereo mode is applied with the satellites separated by 300 km [38].

The triggered EASs were passed through the JEM-EUSO pattern recognition and reconstruction chain using both the slant depth and Cherenkov methods to evaluate the exposure for reconstructed events. To perform a reconstruction, the same cuts as described in the JEM-EUSO Sect. 5.1 were applied. The slant depth method successfully reconstructed $\sim$ 84% of the triggered events with almost constant efficiency above log(E/eV) > 19.6, while for the Cherenkov method only about half of the events were reconstructed. As mentioned before, this is due to the fact that this method is usable up to zenith angles $\sim$ 50° (the value depends on the EAS energy and location on the FS). At higher zenith angles the Cherenkov signal is spread and too dim to be isolated from background fluctuations.

The performance of the angular reconstruction for POEMMA was evaluated at fixed zenith angles (θ = 30°, 45°, 60°, and 75°) for three different energies (E = 7×10^{19}, 10^{20} and 3×10^{20} eV). The same methodology defined for the JEM-EUSO reconstruction was applied to POEMMA, with a fine-tuning of the parameters of the PWISE algorithm. Results are presented in Table 3 in terms of γ_{68} parameter. It is important to underline that a more detailed study of the bias should be performed. The reduction of the bias would improve the overall performance of γ_{68} as it includes both statistical and systematic uncertainties.

The stereoscopic vision of POEMMA allows a much better angular reconstruction than does monocular vision. In stereo mode the reconstruction of the EAS trajectory is robust, yielding a much better angular resolution, which is $\sim 1.5°$($\sim 1°$) or better above 5×10^{19} (10^{20}) eV (see [38] for more details).

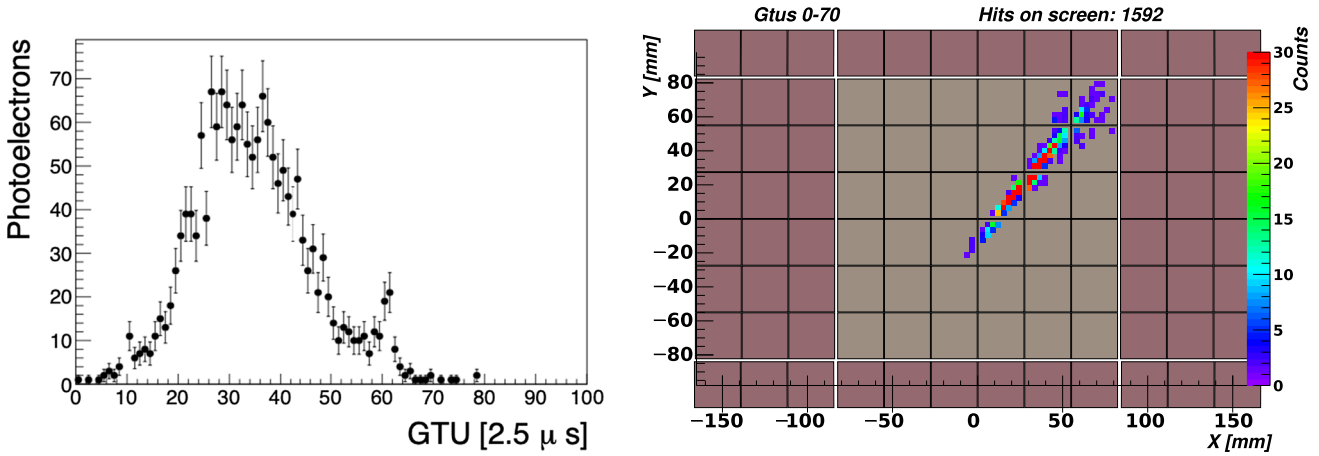

Fig. 20 A 10^{20} eV, 60° zenith angle proton EAS. On the left: The photoelectron profile for the POEMMA detector. On the right: The image on the POEMMA's focal surface. Image taken from [80]

Table 3 Angular and energy resolutions of the POEMMA detector for proton EASs of different energies and zenith angles obtained with ESAF under different assumptions. The angular resolution is obtained at fixed energy in monocular mode. The energy resolution is in monocular mode and is presented for two cases: results in the first column have been obtained with the assumption that the angular reconstruction was provided in stereo mode with an angular resolution of 1° in both zenith and azimuth angles while in the second column we put results without assumption of 1°. Assuming a stereo vision the energy resolution improves by $\sqrt{2}$, assuming no bias or similar bias between the two telescopes

Energy	Energy res. (%)		Angular res. (°)			
[EeV]	All angles (1° res.)	All angles	30°	45°	60°	75°
50	26	30	12	6.2	5.5	5.2
70	25	–	9.9	6.4	3.9	5.1
100	24	27	9.1	4.2	3.5	4.1
300	23	–	6.2	2.3	2.1	1.4

For the energy resolution study, we present here the results for two situations: assuming that the EAS direction has been pre-determined using the stereo approach with a 1° resolution in both zenith and azimuth angles and without this assumption. The results are shown in Table 3. With 1° assumption, for 5×10^{19} eV, the energy resolution is 26% with a +3.5% bias, while for 10^{20} eV the energy resolution is 24% with a −1.5% bias. Since the two POEMMA telescopes provide independent measurements of each EAS, the combined resolution is obtained by dividing by $\sqrt{2}$, assuming no bias or similar bias between the two telescopes, yielding 18% at 5×10^{19} eV and 17% at 10^{20} eV.

A preliminary study of the $X_{\max}$ resolution was performed as well indicating resolutions of the order of those obtained for JEM-EUSO. However, similarly to the angular case, an estimate of the $X_{\max}$ resolution in stereo mode was conducted. The total $X_{\max}$ resolution of POEMMA, including both angular resolution and photoelectron statistics, is about 31 g cm^{-2} at 3×10^{19} eV for events below 60° (72% of the data sample) and 39 g cm^{-2} below 70° (91% of the data sample). At 10^{20} eV the resolution is 17 and 21 g cm^{-2}, respectively (see [38] for more details). These results indicate the much better performance of a stereoscopic detector compared to a monocular vision.

5.4 The TUS configuration

The ESAF code has been used to study the TUS performance and comparison to data with two different approaches and simulation codes. The first one is ESAF coupled with the TUSSIM program package developed at the Joint Institute for Nuclear Research, Dubna (Russia) [81]. ESAF is used to generate the EAS cascade and the fluorescent radiation which is propagated at TUS optics level. Then, the TUSSIM program simulates the TUS detector performance including the Fresnel mirror optical parameters, the light concentrator of the photo detector, the front-end and trigger electronics. In the second approach [82], the TUS detector is implemented directly into the ESAF simulation code. Regarding the optics simulation, approaches similar to JEM-EUSO have been adopted. The standard one, which was used in this work, adopts a parametric simulation module that analytically calculates the position of the photon on the FS and adds a Gaussian spread around this position. This is intended to be a fast working tool to test the features of different optics designs in an approximate way. Once the photons reach the FS, they are transported through the filter and the optical adapter before reaching the photocathode. All the relevant effects including geometrical losses, inefficiencies of the adapter and of the UV filters are taken into account. A parameterization of the photo-multiplier response is included in the electronics part. All the effects like quantum efficiency, dependence on the

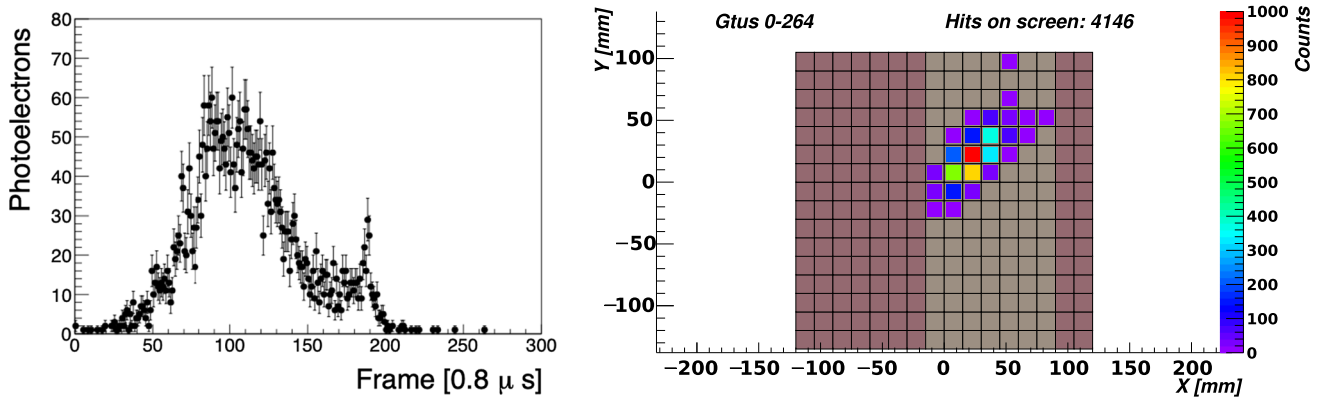

Fig. 21 A simulated 10^{21} eV, 60° zenith angle proton event. Left panel: The photoelectron profile for the TUS detector. Right panel: The photoelectron image for TUS. Image taken from [80]

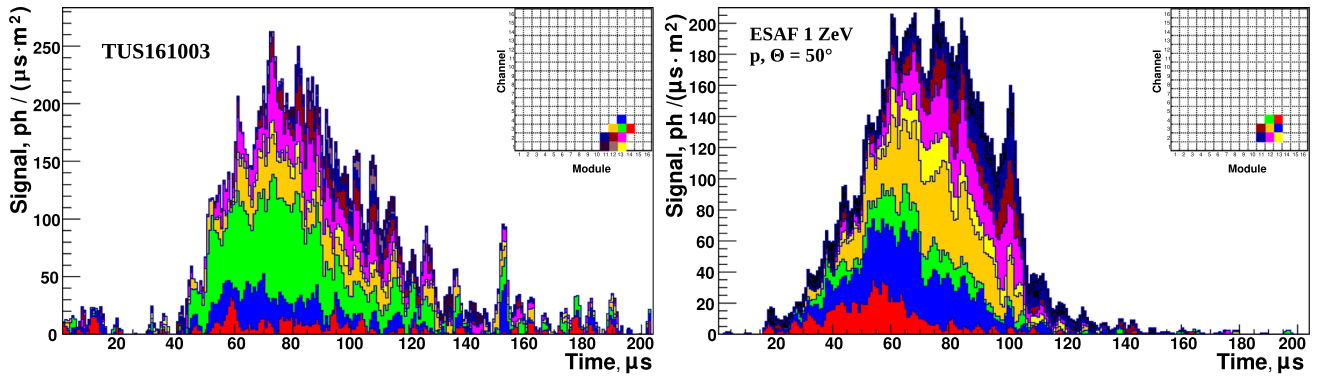

Fig. 22 Left panel: The light curve of the TUS161003 event as the signal of the ten hit channels stacked together. The insert shows positions of the hit pixels on the focal surface. Right panel: An expected TUS detector response to an EAS from a 1 ZeV proton arriving at the zenith angle $\theta \approx 50°$. Image adapted from [29]

incident angle of photons, collection efficiency and cross-talk are also taken into account. The signal is then amplified by a parameterized gain and the resulting output current is collected and treated by the front-end electronics module. Figure 21 shows an example of the light profile and shower track expected to be detected from a 10^{21} eV, 60° zenith angle proton EAS.

During its operation, TUS has detected about 8×10^4 events that have been analyzed offline to select those satisfying basic temporal and spatial criteria of UHECRs. A few events passed this first screening. Those that exhibited some EAS-like characteristics were compared to ESAF simulations to understand if they were consistent with an UHECR origin. One specific event, which was registered in perfect observational conditions, was deeply scrutinized (see Fig. 22). Its phenomenology and the possible interpretations were reported in detail in [29]. Thanks to the comparison with ESAF simulations, it was possible to demonstrate that the PMT waveforms and the light curve of the event show similarities with expectations from an EAS. However, the amplitude corresponds to UHECR energies $E \gtrsim 10^{21}$ eV, which makes the cosmic ray origin of this event highly unlikely as TUS accumulated exposure is two orders of magnitude lower than accumulated exposure collected by ground-based experiments and no event was detected so far above 3×10^{20} eV [83]. Another important phenomenological feature of the event is that it develops very high in the atmosphere. The duration of the signal and its slow attenuation lasting $\sim 60\,\mu$s lead to an estimate of $X_{\max} \sim 550$ g cm^{-2}, which corresponds to the altitude of $\sim$ 7.5 km. On the other hand, if EASs are simulated with an inclination around 45°, which corresponds to the reconstructed direction of the TUS event, the X_{max} has values in the range 915–985 g cm^{-2} which are much deeper in the atmosphere. Moreover, the EAS profile of the TUS event is closer to a 60° inclined event which again doesn't provide a good matching between shower profile and direction reconstruction. An even higher altitude ($\sim$ 8.5 km) of the signal maximum is obtained if one assumes the narrow peak at around 150 μs to be Cherenkov reflection. These values are in a contradiction with expectations from the ESAF simulation of a ZeV event (see Fig. 22). This inconsistency indicates that the peak around 150 μs might be due to other

reasons, including a random fluctuation of the signal or an artifact of the electronics or due to an anthropogenic source on ground. A similar peak was indeed observed also in other events which showed an apparent movement of the signal. These were later on associated with the presence of airports [84]. On the ocean 15 EAS-like events in total were found, four of which had at least three active channels and were registered in good observational conditions. However, for none of them it was possible to reconstruct the arrival direction of the light source accurately, either for the limited number of hit pixels or because they occurred at the edge of the FoV [82]. This shows the importance of ESAF not only to understand the performance of an instrument but also to inspect experimental events through simulations. Mini-EUSO results, as the detector features similar FoV per pixel, even though a higher energy threshold, will help understanding the expected random imitation rate of this kind of EAS-like signals.

ESAF was also used to perform a detailed analysis of the TUS exposure and sensitivity to UHECRs [85]. Two thousand EASs were injected in an area A_{simu} larger than the FoV ($\pm$150 km) to avoid border effects. The TUS trigger logic was implemented in ESAF. Several trigger thresholds used in the mission were tested with an airglow rate of $\sim$ 18 photoelectrons per frame. As a result of our preliminary estimation, we obtained a trigger threshold $\gtrsim 5 \times 10^{20}$ eV. However, this estimation is affected by large uncertainties due to an accident that occurred during the first days after launch (described in [29]), when 20% of the PMTs were destroyed and sensitivities of the remaining PMTs changed compared to the pre-flight measurements. Despite a number of in-flight calibration attempts, considerable uncertainties still remain on the PMT gains. Moreover, the TUS trigger algorithm is more efficient for horizontal showers leading to a higher fraction of high zenith angle events. The majority of the events could indeed trigger only above 40°–50°. This is a consequence of the persistence condition of the trigger that rejects all events lasting for a short time.

Secondly, the efficiency of the trigger in cloudy conditions was evaluated. The cloud condition for each trigger has been estimated based on MERRA data (see [82] for details). One thousand EASs at fixed energy have been simulated for each cloud top height condition in similar way as for clear sky. An estimate of the overall reduction of the exposure during the whole flight can be given by an average of the trigger efficiency weighted by the fraction of triggers in each condition. This leads to 57% of what is expected for the clear sky case. By taking into account the above factors the geometrical exposure in clear sky conditions amounts to $\sim$ 1550 km^2 sr yr at plateau energies, reducing to $\sim$ 884 km^2 sr yr at 2×10^{21} eV taking into account the cloud impact. It is important to recall that the estimation of the exposure might have a cloud dependence due to the interplay of the brightness of the shower and the location of its maximum. For the same cloud location, at lower energy a lower value for the exposure is expected.

5.5 The Mini-EUSO configuration

The Mini-EUSO configuration has been incorporated in ESAF including its trigger logic [39]. Proton showers have been simulated using the SLAST-GIL shower generator. A ray trace code of the Mini-EUSO optics response is included in ESAF. Figure 23 shows an example of a 10^{21} eV, 60° zenith angle simulated proton event. Mini-EUSO is at the detection threshold at such energies. The signal looks dim. Background has not been simulated but it is expected to be at a level of $\sim$ 1 count/pixel/GTU(2.5 μs) in standard observational conditions.

The trigger efficiency curve and aperture have been studied in a way similar to that used for the other instruments. Figure 24 shows the derived trigger efficiency and the aperture curves.

The experimental data taken by Mini-EUSO allow a first comparison with the assumed background levels in JEM-EUSO, K-EUSO and POEMMA to verify that the estimated performance is based on justified assumptions. Table 4 shows Mini-EUSO results on the average UV emissions in different conditions: clear and cloudy conditions, sea and land, various lunar phases as reported in [30]. As explained in [30] the presence of clouds is derived from the US National Weather Service Global Forecast System (GFS) [86]. Assuming no-moon conditions and typical land/ocean and clear/cloudy atmosphere ratios equal to 30/70, the average background level is $\sim$ 1.3 counts/pixel/GTU.

In order to re-scale this value to the JEM-EUSO (JE) case a full simulation of JEM-EUSO and Mini-EUSO detectors was performed with ESAF. In case of Mini-EUSO (ME) the overall efficiency of the detector was fine-tuned in ESAF, mainly acting at the level of MAPMT response, to match the measured one $\epsilon_{ME} = 0.080 \pm 0.015$ (see [30]) for a point-like source on ground. A flat diffused UV emission in the range λ = 300–400 nm was simulated at the detector's aperture either with a range of zenith directions much larger than the FoV of the instrument ($\pm$60° for both detectors) or just within the FoV of the detectors ($\pm$30° for JEM-EUSO and $\pm$22° for Mini-EUSO). The measured background ratio (R(ME/JE)) between Mini-EUSO and JEM-EUSO at FS level was R(ME/JE) = 0.98–1.04 slightly depending on the range of zenith angles. This indicates that the expected photon counts for JEM-EUSO should be similar to Mini-EUSO one $\sim(1.3 \pm 0.2)$ counts/pixel/GTU taking into account the uncertainty in the estimation of Mini-EUSO efficiency. This result indicates that the average value of $\sim$ 1.1 counts/pixel/GTU assumed in JEM-EUSO simulations is within the current estimation and confirms the robustness of the hypotheses undertaken with ESAF.

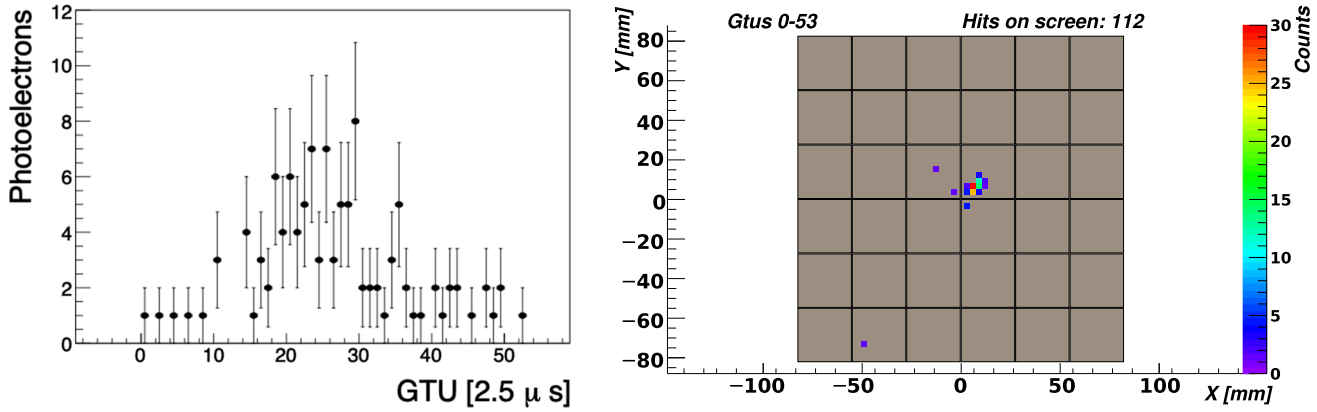

Fig. 23 A 10^{21} eV, 60° zenith angle proton event. Left: The photoelectron profile for the Mini-EUSO detector. Right: The photoelectron image. Image taken from [80]

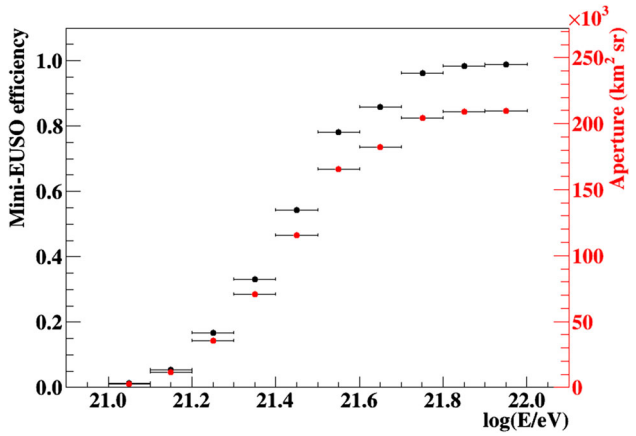

Fig. 24 The trigger efficiency (on the left axis, in black) and geometrical aperture (on the right axis, in red) are shown as a function of the EAS energy, E, in eV. A UV background level of 1 count/pixel/GTU(2.5 μs) was considered in both cases

ESAF simulations are performed to test the UHECR origin of short bright signals detected by Mini-EUSO with time duration in the range of EASs. So far all the investigated candidates are not compatible in pulse shape and track image with those expected from EAS. Those showing a periodic behaviour can be immediately discarded as anthropogenic sources, while non-repetitive ones require a more detailed analysis. One of the most interesting examples in the Mini-EUSO data sample is shown in Fig. 25. It has been detected off the coast of Sri Lanka. The trigger was issued by the event in the red circle. The lightcurve presents the characteristic bi-gaussian shape of an EAS, with a faster rise and a slower decay time. The event was compared to different simulated EASs with variable energy and zenith angle. No simulated EAS is compatible with both the image size and the time duration of the light profile. In fact, the light spot is compatible with a nearly vertical event, but the duration is much longer than the time needed by a vertical shower to develop in atmosphere and reach the ground. This event has, therefore, a different nature which is currently under investigation. A detailed description of the onboard performance of the Mini-EUSO first level trigger and search for EAS-like events can be found in [87].

Among Mini-EUSO scientific objectives there is also the study of slower events such as meteors and fireballs, and the proof-of-principle of space debris observation with absolute magnitude of $M \lesssim +5$ using the albedo from the Sun [88]. In optimal dark conditions, at the detection threshold $M = +5$, the signal (integrated at steps of 40.96 ms) will exceed the UV-nightglow level by 3–4σ. These events will be detected using offline trigger algorithms on ground [89].

Table 4 Average emission values in counts/(pixel·GTU) for Mini-EUSO for sea and ground for various lunar phases and cloudiness. In the table 'cloudy all' indicates the weighted average of the counts in 'cloudy land' and 'cloudy sea'. Half-moon includes Moon fractions between 0.4 and 0.5, and full-moon includes fractions between 0.9 and 1. The brightest pixels (above the 99th percentile) were excluded when calculating the mean and standard deviation to mitigate the effects from bright anthropogenic sources. For conditions with multi-modal distributions, the mode closest to the average is displayed. Table adapted from [30]

	Clear sea	Clear land	Cloudy sea	Cloudy land	Cloudy all
No-moon	0.9	1.4	1.3	1.7	1.4
Half-moon	1.8	2.8	13.0	8.1	9.7
Full-moon	37.6	35.1	50.7	51.1	51.0

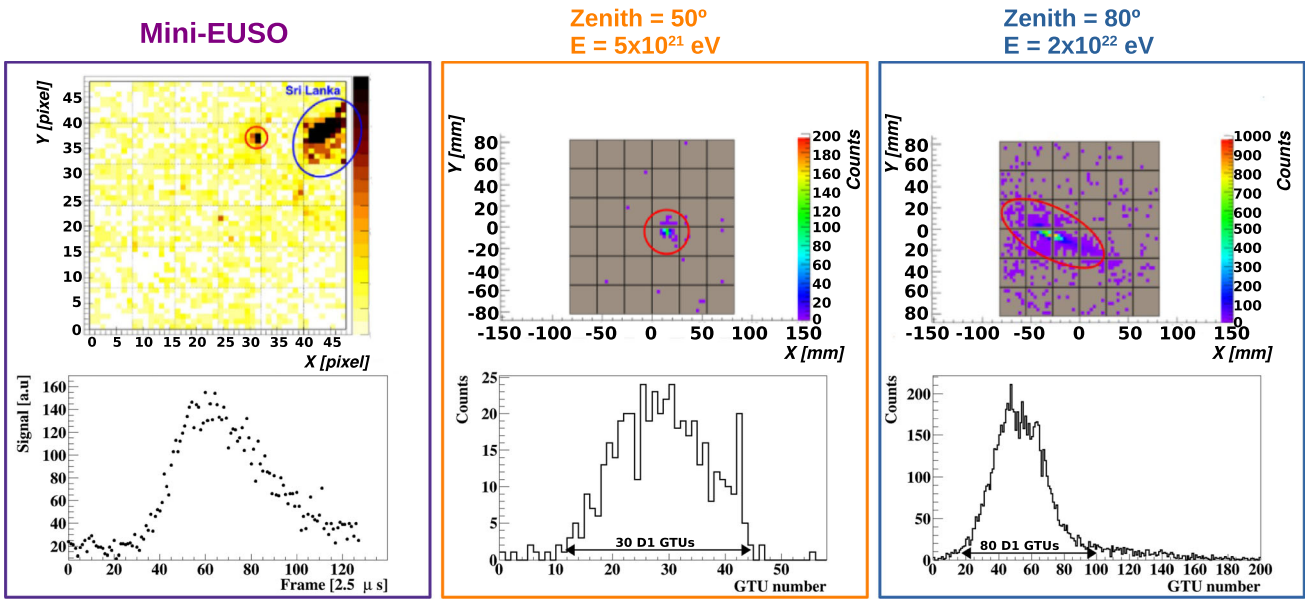

Fig. 25 Left panel: One frame of an event triggered off the coast of Sri Lanka. The blue circle (upper right) encloses a static, bright light source to be discarded. The trigger was issued by the event in the red circle. Bottom left pane: The lightcurve of a 3 × 3 pixel box that contains the event. The lightcurve presents the characteristic bi-gaussian shape, with a faster rise and a slower decay time. Center and right panels: Two proton EAS simulated through ESAF at two different energies and zenith angles (top part presents the image of the events while the bottom part the corresponding light profiles). Center panel shows a simulation at zenith $\theta = 50°$ and energy $E = 5 \times 10^{21}$ eV. The signal persists on few pixels for $\sim$ 30 GTUs, much shorter than the measured one, the sharp cutoff is given by the shower reaching the ground. Right side is a simulation at zenith $\theta = 80°$ and energy $E = 2 \times 10^{22}$ eV. The signal is much longer in time but the footprint on the focal plane is much more elongated. Image adapted from [87]

Figure 26 shows an example of a simulated meteor track having absolute magnitude M = +5 crossing the field of view of Mini-EUSO with a 45° inclination with respect to the nadir axis. The meteor speed is 70 km s^{-1} and its duration is 2 s. The center and right panels show two different meteor candidates detected by Mini-EUSO. In Mini-EUSO data, there are tens of thousands of meteor candidates with different brightness and time duration which can be simulated with ESAF.

As pointed out in [88], a detector like Mini-EUSO is also potentially capable of detecting space debris, if not directly exposed to sunlight. Under this assumption, Mini-EUSO would be effectively a high-speed camera with a large FoV and could be used as a prototype for the detection of space debris during the twilight periods of observation. It will detect debris when they are illuminated by the Sun. In the current simulation with ESAF, the photon flux of the Sun in the 300–400 nm has been considered to be 10^{20} photons m^{-2} s^{-1}. The debris are assumed to have a spherical shape of diameter d and a variable reflectance. Therefore, the event appears as a spot of light moving through the field of view with slowly variable light profile.

Figure 27 shows the potential of Mini-EUSO to detect space debris. On the left side a simulated object with 3 cm radius flying at 360 km height (40 km from Mini-EUSO) with a speed 7.7 km/s is displayed. A study of the sensitivity of Mini-EUSO to space debris in terms of size and relative distance has been carried out. The trigger threshold requires a signal at least 3σ above background for at least 5 consecutive frames of 40.96 ms each. The UV background has been assumed to be the same as in the other simulations at 1 count/pixel/GTU. However, it is possible that for this specific measurement, the background could be higher due to the presence of some sunlight. Results are displayed on the right side of Fig. 27.

Usually, Mini-EUSO detects on continents ground flashers. They are often associated with airport lights (but not always). These types of lights are simulated in ESAF as point-like sources with a rising and decaying curve following the specifications of commercial flashers. In parallel we are also testing the response of ESAF to the light emitted by flasher systems that have been built in the framework of the JEM-EUSO collaboration to provide an in-flight instrument calibration. The flasher consists of a 100 W COB-UV LEDs, DC power supply and an Arduino circuit. The flasher campaign has been done at Piana di Castelluccio, Italy, at 1500 m above sea level (lat. 42.766, lon. 13.190), in the clear night sky conditions of May 3rd–4th, 2021 when Mini-EUSO was operational while ISS was flying over central Italy. After including in ESAF the estimation of the detector sensitivity

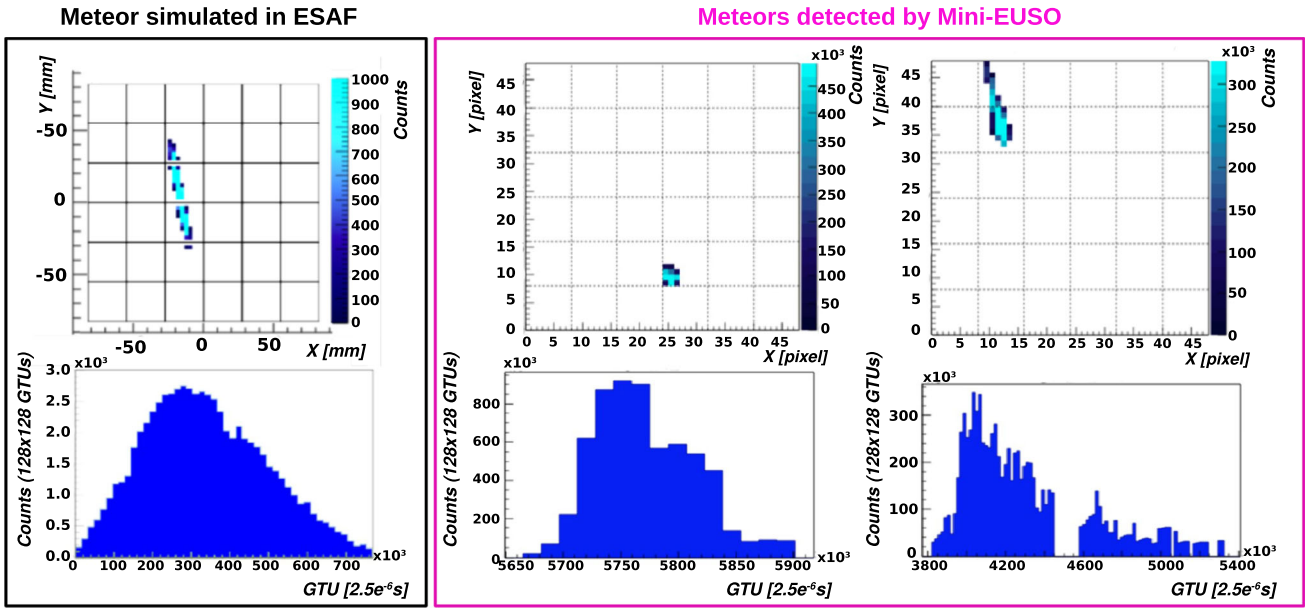

Fig. 26 Left panel: ESAF simulated light track of a meteor of absolute magnitude M = + 5 and 45° inclination in Mini-EUSO (the effects of UV-nightglow are not included and the threshold is 30 counts). Bottom: Expected light profile. Each time bin on the x-axis corresponds to an integration time of 40.96 ms. Center and right panels: Example of meteors detected by Mini-EUSO. In the Mini-EUSO data, there are meteors with different brightness and time duration. Image taken from [90]

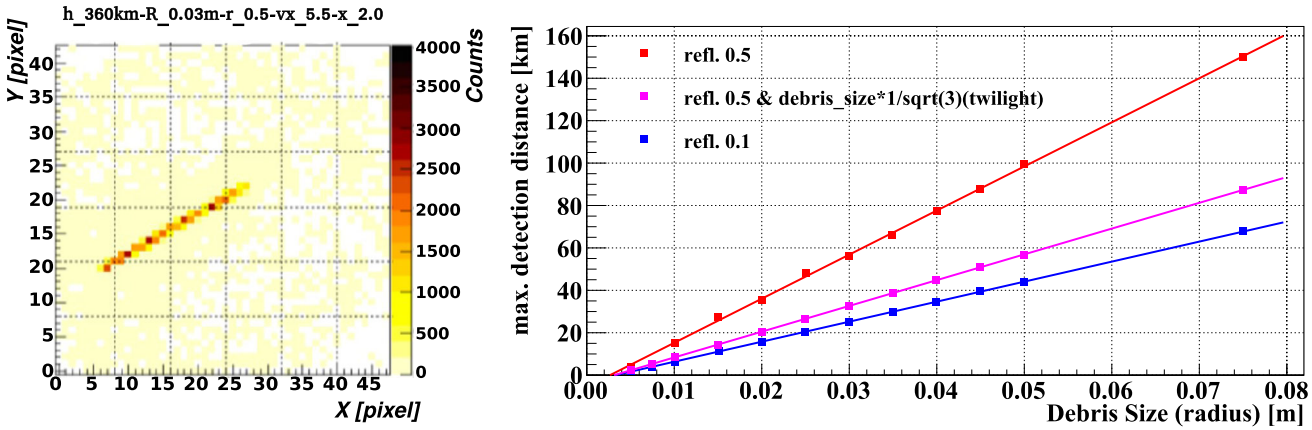

Fig. 27 Left panel: An example of space debris detection simulated with ESAF. Right panel: Maximum distance of space debris observable by Mini-EUSO from the ISS as a function of reflectance and size of the debris, derived from ESAF simulations using the standard background level adopted for UHECR detections. Image adopted from [90]

obtained with ground tests, simulations were performed. The top panel of Fig. 28 shows the Mini-EUSO data. The left plot is the raw data image of one D3 frame (GTU = 40.96 ms) while the central one shows the light curve of the integrated counts of 3 × 3 pixels around the peak count pixel inside the red circle. The right plot shows the zoomed in image of the green circled part of the center plot, corresponding to the timing and duration of the ESAF simulation. The bottom panel shows the simulated flasher event with a background level of 2.5 counts/pixel/GTU which is resulting in ∼ 15% difference between simulated and real background. The center shows the integrated counts of 3 × 3 pixels around the peak pixel inside the red circle in the left plot, with background photons, while the right shows the integrated counts of the same pixels but without background photon counts to see the total signal contribution. The tendency of signal fading as the flasher moves in the FoV is clearly visible in both Mini-EUSO and ESAF data. As a preliminary result, the number of expected detections obtained by ESAF matches well to the

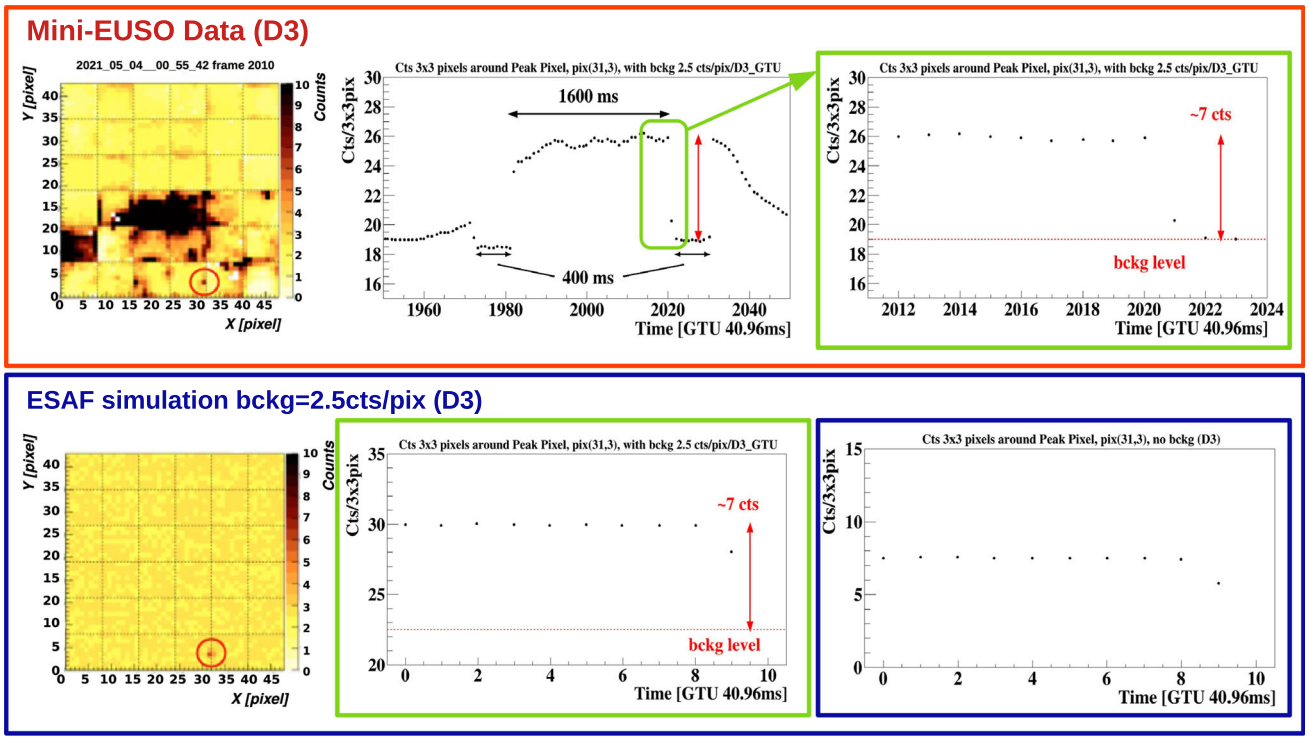

Fig. 28 Top: Mini-EUSO flasher campaign event. The central panel shows the light evolution of summed counts of 3 × 3 pixels around the peak count pixel, indicated by the red-circle on the left plot, for a cycle of 1600 ms pulse (GTU = 40.96 ms). The transit of the 1600 ms pulse preceded and followed by 400 ms off is clearly seen. Right panel: The zoomed in plot to the duration and timing where ESAF simulated the same event, as shown in the bottom plots. Bottom: Simulated flasher campaign event by ESAF. The central panel shows the light evolution of summed counts of 3 × 3 pixels around the peak count pixel, indicated by the red-circle on the left plot with a background level of 2.5 counts/pixel/GTU, which is resulting in ∼ 15% difference between simulated and real background. The right panel is the same as the central one without background to see the signal contribution

detected number by Mini-EUSO. More details can be found in [90].

5.6 EUSO Balloons configuration

EUSO-Balloon and EUSO-SPB1 have been implemented in ESAF while EUSO-SPB2 in its final configuration is currently implemented only in OffLine. EUSO-Balloon and EUSO-SPB1 share the same configuration in ESAF. Only parameters such as quantum efficiency of MAPMTs, balloon height, etc. change depending on the performed simulation. A ray trace code configuration for the optics response has been implemented as well together with the parametric option. The adopted trigger logic can be activated too. Figure 29 shows an example of a light profile and shower track for a proton simulated EAS of 10^{19} eV energy and 45° of zenith angle.

A significant difference compared to space-based missions is the much shorter distance between the detector and cascade in the atmosphere. As a result, most of the EAS tracks are not fully contained in the FoV. To perform an estimation of the energy range of sensitivity to UHECRs and of the expected number of events under specific assumptions of the balloon configuration, a new methodology has been adopted to compute the aperture of the instrument which speeds up the simulation by a factor of 10 at least. We defined a cylindrical volume $\mathcal{V}$ (8 km radius on ground) around the FoV where EAS must pass before being fully simulated by ESAF (see Fig. 30). Showers not passing through this volume are guaranteed to never cross the FoV (which is much smaller, ±4 km side on ground) and therefore are not simulated.

We define the exposure $\mathcal{E}$ as:

$$\mathcal{E}(E) = \langle\epsilon\rangle(E) \int_{A_{\text{simu}}} dA \int_{\Omega} d\Omega \int_{t_{\text{acq}}} dt. \tag{3}$$

The average efficiency $\langle\epsilon\rangle(E)$ is therefore computed as:

$$\langle\epsilon\rangle(E) = \frac{\int_{A_{\text{simu}}} dA \int_{\Omega} d\Omega \frac{N_{\text{trigg}}(E,x,y,\theta,\phi)}{N_{\text{simu}}(E,x,y,\theta,\phi)}}{\int_{A_{\text{simu}}} dA \int_{\Omega} d\Omega} k, \tag{4}$$

where k represents the average correction factor for the efficiency taking into account the fraction of events passing through the volume $\mathcal{V}$ with respect to the events on the entire

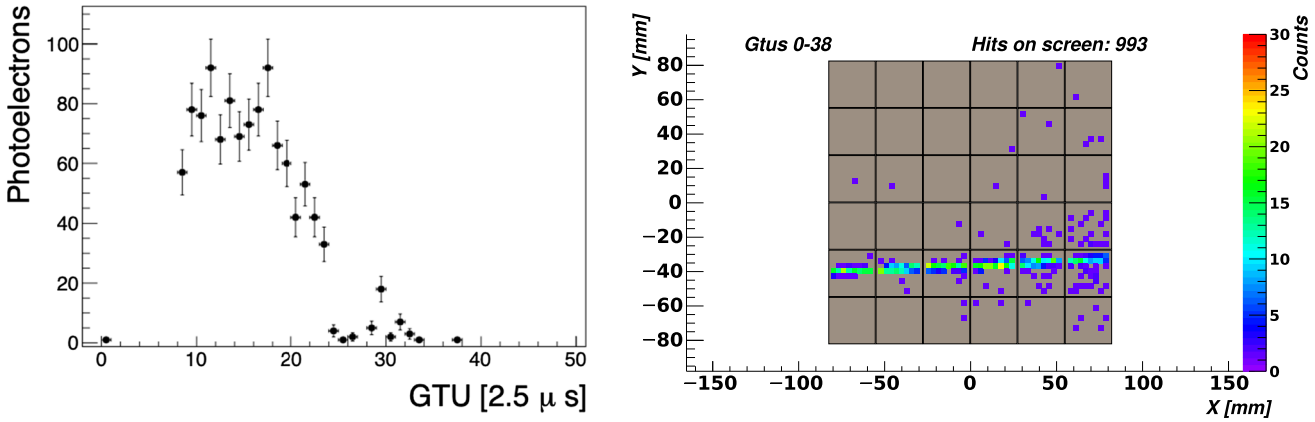

Fig. 29 A 10^{19} eV, 45° zenith angle simulated proton event. Left: The photoelectron profile for the EUSO-SPB1 detector. Right: The photoelectron image for EUSO-SPB1. Image adapted from [80]

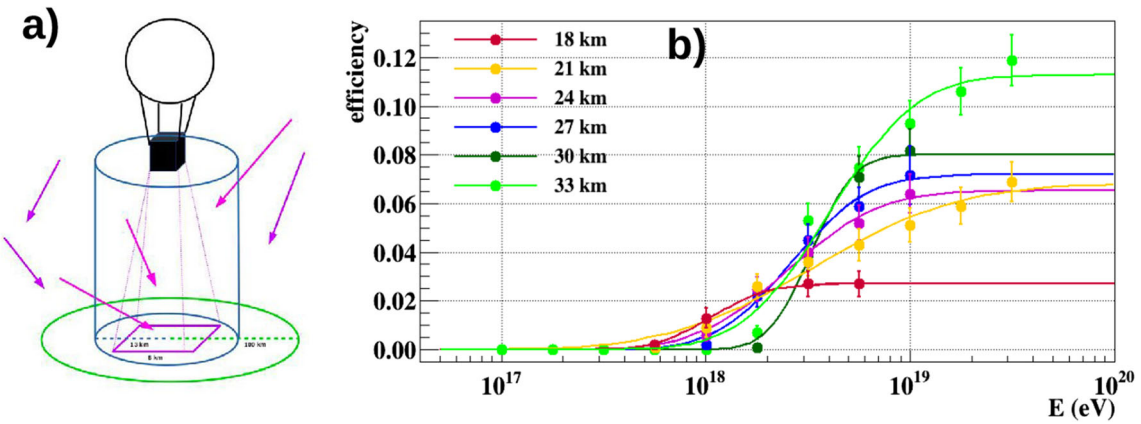

Fig. 30 Panel **a**: To speed up the simulation process in balloon configurations, EASs are fully simulated if crossing a cylindrical volume $\mathcal{V}$ which includes the balloon FoV. EAS not crossing this volume are not simulated. Panel **b**: Trigger efficiency as a function of proton EASs energy for different heights of the balloon

solid angle N_{test}:

$$k = \frac{\int_{A_{\text{simu}}} dA \int_{\Omega} d\Omega \frac{N_{\text{simu}}}{N_{\text{test}}}}{\int_{A_{\text{simu}}} dA \int_{\Omega} d\Omega}. \tag{5}$$

The right panel of Fig. 30 presents an example of the trigger efficiency as a function of proton EAS energy for different heights of the balloon. Finally, the number of events is calculated as

$$N(E) = \mathcal{E}(E)\Psi(E), \tag{6}$$

where $\Psi(E)$ is a fit to the Pierre Auger spectrum [1]. We see in Fig. 31 the triggered spectrum as expected by EUSO-SPB1 floating at an altitude of 30 km in clear sky and for a mission duration t_{acq} of 118 h. This was the total dark time expected prior to launch on the moon phase of March–April 2017. The total number of events has been calculated by integrating the number of events on the entire energy range. The spectrum is peaked at energies around 3×10^{18} eV. It is important to point out that this is the energy at which EUSO-SPB1 was 50% efficient in EAS triggering according to the field tests performed at EUSO-TA site in October 2016, prior to flight [91] (see Sect. 5.7).

By implementing the cloud distribution in ESAF according to satellite databases along the trajectories of previous NASA-SPB flights and by assuming 30 h of acquired data, due to the short EUSO-SPB1 flight, ESAF provided a preliminary expected number of $\sim$ 1 UHECR along the flight right after the conclusion of the mission. Successive studies which employed both OffLine and ESAF, and took better into account the effective detector performance, the measured background level and the effective presence of clouds showed that this preliminary estimation [15,93,94] has to be decreased by a factor of $\sim$ 2 (0.4 events in 25 h of effective good quality data taking). This shows the usefulness of ESAF either as a tool for quick performance studies or for more accurate data analyses. Additionally, EAS tracks generated with ESAF were extensively used in neural network

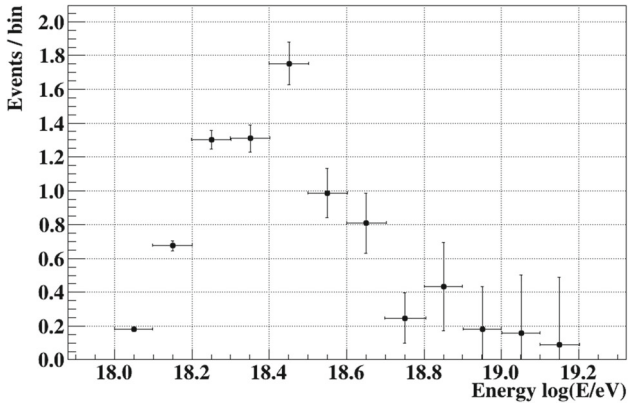

Fig. 31 The expected number of triggered EAS for EUSO-SPB1 floating at an altitude of 30 km assuming clear sky condition and a flight duration corresponding to 118 h of dark time. Image adapted from [92]

algorithms to train the networks to search for EAS tracks. No track was found in the data [95].

At the very beginning of the flight, low energy cosmic rays directly interacting in the detector drew the attention as they looked like very fast linear tracks, faster than normal EAS events. During one single GTU the entire PDM is crossed by such a light pulse. An example of this class of events is shown in Fig. 32. The left side shows the typical light track of a direct cosmic ray quasi-planar to the PDM. The signal lasts one GTU. The right side of the figure shows the attempted production of a similar track with an EAS generated by an UHECR proton. The track shown in the figure is generated by a highly inclined EAS with $\theta = 89°$ and energy $E = 5 \times 10^{18}$ eV, with the first interaction point at 280 km from the nadir position at 30 km altitude, and crossing the detector FoV at a distance of $\sim$ 4.5 km from the detector. The EAS event appears much dimmer than the experimental one. This is due to two different reasons. The first is that at high altitudes the light emission is smaller due to the much lower atmospheric density. The second is related to the fact that the signal crosses the pixel FoV in $\sim$ 80 ns as the pixel FoV is $\sim$ 25 m wide at 4.5 km distance from the balloon. Taking into account a double-pulse resolution of 6 ns, the signal can not exceed a few counts/pixel/GTU as seen in the ESAF event. It is, therefore, extremely difficult to reproduce such a bright and fast signal in the camera with an UHECR event. On the other hand, a direct cosmic ray can produce de-excitation in the glass filter or photo-cathode with a decay time comparable to 1 GTU and the signal can be much brighter. This study was carried out during the days just after this event was detected and shows the utility of ESAF also as a quasi-online tool to interpret the data.

A first attempt to adapt the JEM-EUSO reconstruction algorithms to the balloon configuration was performed. Figure 33a shows an example of reconstructed shower profile for EUSO-Balloon. We can see here the real (black line) and reconstructed profile (points). The GIL fit to the reconstructed points marked in red is represented as a continuous red line. As the figure shows, the reconstructed profile is slightly overestimated (as in the case of JEM-EUSO) due to the lack of backscattered Cherenkov correction. The profile is cut above $\sim$ 1090 g/cm^2 due to the impact with the ground. The resulting Cherenkov reflection feature is also visible in the reconstructed profile. The shower of energy 10^{19} eV and 25° zenith angle has been reconstructed as 1.1×10^{19} eV. The χ^2/DoF is 0.97 and the number of degrees of freedom of the fit is 12.

Figure 33b shows a sample of reconstructed events with energy 10^{19} eV and 25° zenith angle. As in JEM-EUSO, we calculated the parameter R (2) for each event. A gaussian fit has been performed for the resulting distribution and

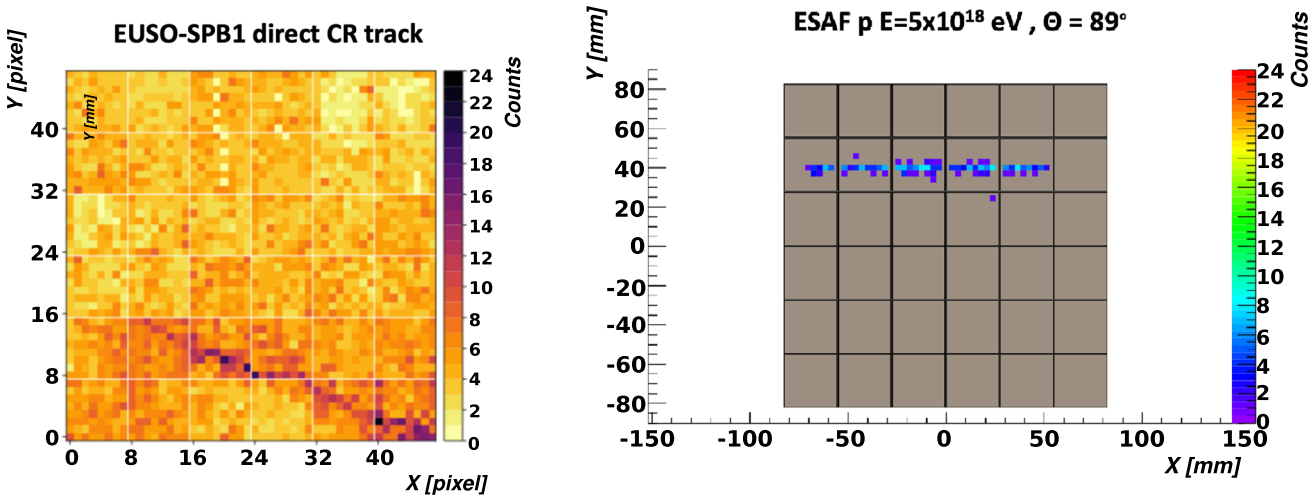

Fig. 32 Left side: Direct cosmic ray triggering the EUSO-SPB1 detector. Right side: Simulated proton EAS of energy $E = 5 \times 10^{18}$ eV crossing the balloon FoV at $\sim$ 25 km altitude with a zenith angle of $\theta = 89°$. They both correspond to 1 GTU data

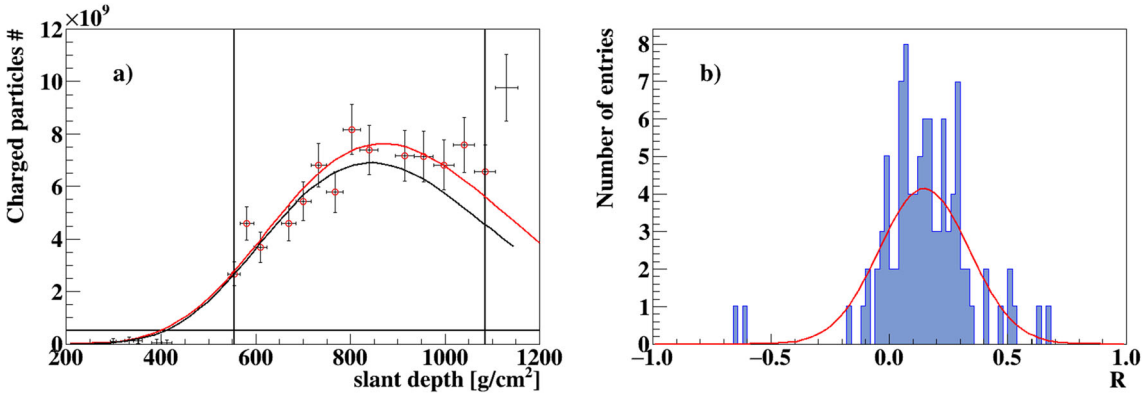

Fig. 33 Panel **a**: We show here an example of an event reconstructed by EUSO-Balloon. The continuous black line indicates the real simulated shower profile (the number of charged particles in the shower at each slant depth). The black points show the reconstructed profile as obtained by the algorithms. The points which are accepted as fit data are indicated by red circles and the GIL fit applied to these points is shown by the continuous red line. We clearly see how the automatic fit correctly excluded the Cherenkov mark visible at the end of the curve. The fitting range and the minimal threshold automatically chosen by the algorithms are also shown as black straight lines. Panel **b**: An example of the R reconstruction parameter fitted over a sample of events with a gaussian function. The sigma of the distribution is 0.16, with a mean value of ~ 0.15 showing a clear overestimation of the energy due to the lack of the backscattered Cherenkov correction. Image adapted from [96]

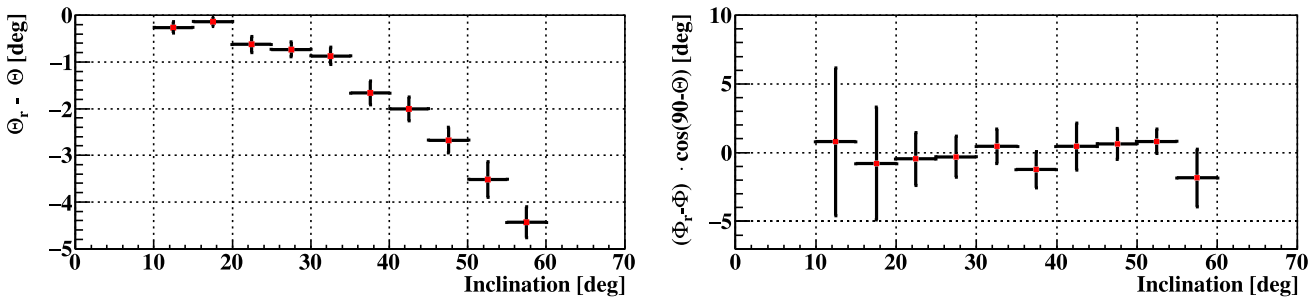

Fig. 34 Mean value and standard deviation of $\Delta\Theta = \Theta_{rec} - \Theta_{sim}$ (left) and $\Delta\Phi = (\Phi_{rec} - \Phi_{sim})cos(90 - \Theta)$ (right) plotted against the true zenith angle (inclination) for EUSO-Balloon. Image adapted from [97]

represented as a red continuous line. The sigma of this distribution is 0.16 providing an estimation of the resolution for this energy and angle. At energies around $3-5 \times 10^{18}$ the resolution worsens to 30% while for 45° inclined EAS a further 10% decrease in resolution is observed. This is opposite to the JEM-EUSO case, where the reconstruction of inclined EAS gives better performance. This behaviour is due to the relatively small FoV of the balloon leading to only partial containment within the FoV for inclined showers and hence much larger uncertainties in the reconstruction. Concerning the angular resolution, the γ_{68} analysis provides resolutions which are $\sim 4°$ for 10^{19} eV and 25° zenith angle. At $3-5 \times 10^{18}$ eV the resolution worsens to around 5°. On average the angular resolution for 45° inclined EAS worsens by $\sim 2°$. These results are consistent with the energy reconstruction, giving again an indication that the different kinematics of the signal may be affecting the reconstruction. The fraction of events that can be reconstructed, even if with modest angular and energy resolutions, is $\sim 70\%$ at energies $E > 3 \times 10^{18}$ eV and angles between 25° and 45°. This is promising for the future balloon flights as it demonstrates that for a significant fraction of detected events a reconstruction procedure could be applied to derive a reasonable energy estimation.

We present in Fig. 34 results related to the angular reconstruction in EUSO-Balloon. Over 12,300 EAS were simulated in the energy range between 10^{18} and 10^{19} eV. The zenith angles were chosen between 10° and 60°. All events were distributed randomly having their impact point within an area of 10×10 km^2 around nadir position. The FoV projected on ground corresponds to an area of 8.4×8.4 km^2. The lower limit in zenith angle is due to the fact that the track on the FS is too short to be fitted. For zenith angles exceeding about 50°, the shower track does not fit entirely on the PDM. Slightly fewer than 2500 events were successfully triggered and reconstructed. The angular reconstruction is evaluated in terms of mean value and standard deviation between reconstructed and simulated angles ($\Delta\Theta = \Theta_{\rm rec} - \Theta_{\rm sim}$

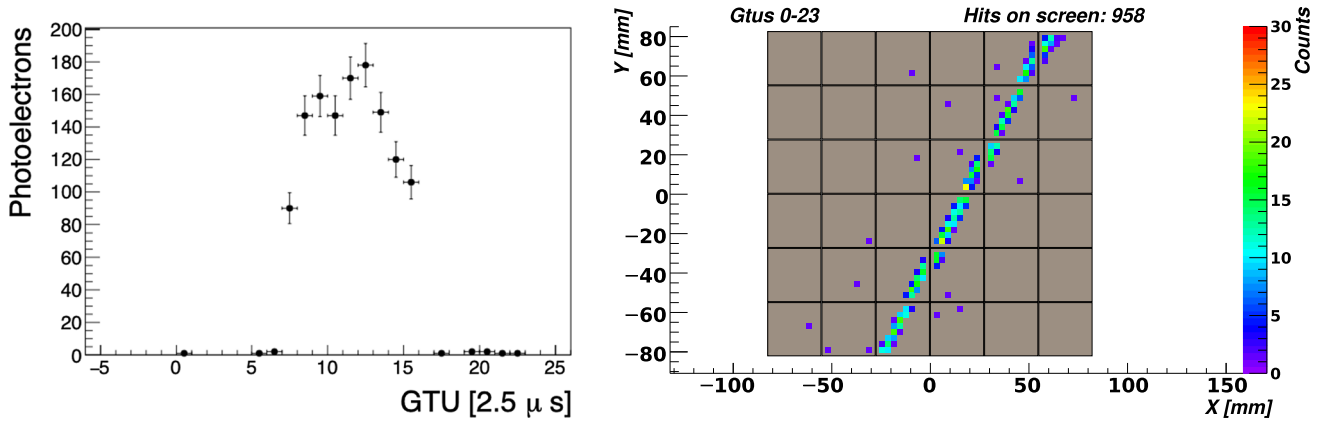

Fig. 35 A 10^{19} eV, 45° zenith angle simulated proton event impacting at 25 km distance from the detector. Panel **a**: The photoelectron profile for the EUSO-TA detector. Panel **b**: The photoelectron image for EUSO-TA. Image taken from [80]

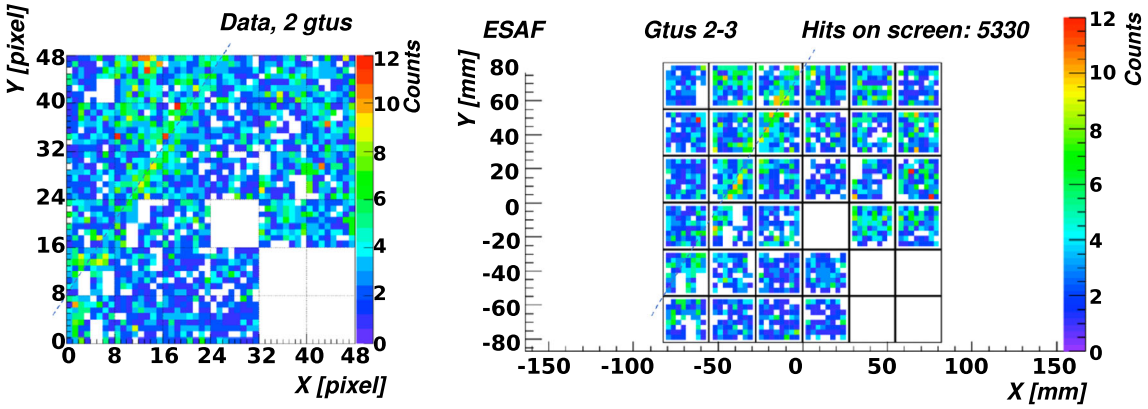

Fig. 36 Comparison between an UHECR event observed by EUSO-TA (left) and a proton shower simulated with ESAF (right) assuming the EAS parameters provided by the TA reconstruction of the event (E = **2.4** $\times 10^{18}$ eV, zenith $\theta = 41°$). No longitudinal distribution is provided for this event as its duration is confined in 2 GTUs. The background is added to the EAS simulation using real data. The dashed line is just guidance to recognize the event track. Data collected in two following GTUs are added together, reducing signal over noise ratio. The white squares include 1 full EC and 1 MAPMT not operational at that time as well as low efficiency pixels

and $\Delta\Phi = (\Phi_{\text{rec}} - \Phi_{\text{sim}}) \cdot \cos(90 - \Theta))$. The direction of the EAS can be measured sufficiently well when the zenith angle is between 10° and approximately 50°. The resolution of γ, the opening angle between the true shower direction and the reconstructed direction, is found to be $\gamma < 5$ for EAS contained within the FoV increasing and saturating at about 8 deg for uncontained showers. Obviously, the probability that parts of the signal are lost increases at the edge of the FoV, increasing the uncertainty in the arrival direction reconstruction. More details of this analysis can be found in [97].

5.7 EUSO-TA configuration

The EUSO-TA configuration has been included in ESAF as well. An example of a simulated 10^{19} eV, 45° zenith angle event impacting at a distance of 25 km from the detector is shown in Fig. 35.

EUSO-TA was also the first detector implemented in OffLine. Therefore, at the very beginning several efforts were made to cross-check the detector implementations and EAS simulations in the two software packages, by comparing the expected number of detected events and their characteristics with those predicted by simulations. Figure 36 shows a comparison between an UHECR event observed by EUSO-TA and a proton simulated with ESAF assuming the EAS parameters provided by the TA reconstruction of the event (E = **2.4** $\times 10^{18}$ eV, zenith $\theta = 41°$). In this phase EUSO-TA events were acquired through an external trigger from TA fluorescence detectors. The background is added to the EAS simulation using real data. Taking account of reconstruction uncertainties, the simulated event reasonably reproduces the detected one.

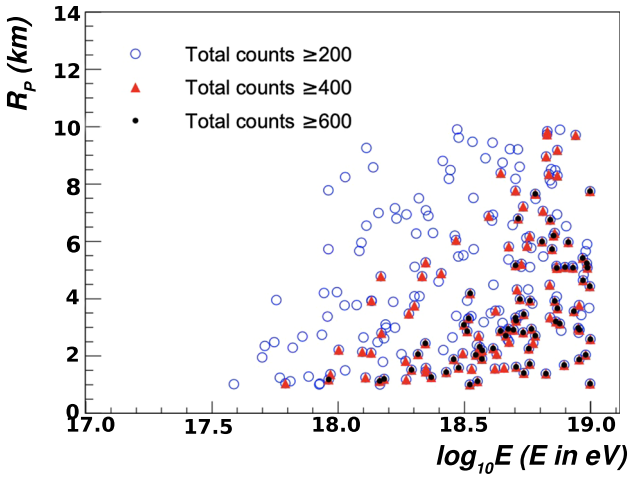

Fig. 37 Relation between the EAS energy and the impact parameter R_p. 1000 proton events were simulated, and among them 229, 118, and 67 events generated more than 200, 400, and 600 counts over 3 consecutive GTUs in the EUSO-TA detector, respectively. In this plot a cosmic ray power spectrum E^{-1} has been considered: more events at high energies are present in the plot than expected in reality, for which the average spectrum scales by about E^{-3}. Image taken from [98]

The ESAF software was also used at the beginning to cross-check the measured number of UHECRs with expectations from simulations [98]. In this analysis the following assumptions were made: (1) the TA trigger efficiency was assumed to be 100%; (2) the cosmic ray power spectrum was simulated with an E^{-1} differential spectrum in the range $10^{17} \leq E \leq 10^{19}$ eV to have higher statistics of sample for calculating the trigger efficiency for every energy bin. The spectrum was later on re-weighted according to the IceTop measurements [99] in the $10^{17} - 5 \times 10^{17}$ eV energy range and with the Auger spectrum [1] at higher energies; (3) EASs were uniformly generated in azimuth angle with a $\sin(2 \cdot \theta)$ distribution in zenith angle; (4) the impact point on ground of the shower axis was generated uniformly within a radius $R \leq 50$ km around the telescope.

The number of EASs within the EUSO-TA FoV with an impact parameter $1 \leq R_p \leq 10$ km was then estimated. A selection was made to require at least 200, 400, or 600 counts in the detector integrated over 3 consecutive GTUs. EASs in EUSO-TA are detected on average at even closer distances compared to the balloon configuration, so the signal can last no more than 1 GTU. Figure 37 shows the relation between the EAS energy and the impact parameter R_p. Among 1000 simulated events with a power spectrum E^{-1}, 229, 118, and 67 EASs generated more than 200, 400, and 600 counts in the EUSO-TA detector, respectively.

This number of events was then rescaled by taking into account the IceTop and Auger fluxes. The results indicate that under the assumption of an acquisition time of 120 h, the total acquisition time in 2015, EUSO-TA can detect ~ 6 events with a signal of at least 600 counts integrated over 3 consecutive GTUs. This signal is in the range of the photon-counts excess over the background level, typically measured in the events detected by EUSO-TA.

These results, extrapolated to 140 hours of effective data taking by EUSO-TA would predict 7 detectable events which is a number compatible with the 9 effectively detected events by EUSO-TA in similar amount of time, thus confirming the capability of ESAF to reproduce the EAS detected by the EUSO-TA.

6 Conclusions and perspectives

The JEM-EUSO program is an international effort devoted to the study of UHECRs from space. The program consists of a series of missions some completed and some in preparation, in space, on stratospheric balloons, or on ground. All such detectors demand an extensive simulation work to estimate the performance and to support the data analysis. The original ESAF package developed in the framework of the EUSO project evolved within the JEM-EUSO collaboration. A new branch was created which includes the detector configurations of almost all the missions which have been conceived, performed, or under development in the program: JEM-EUSO, K-EUSO, POEMMA, TUS, Mini-EUSO, EUSO-Balloon, EUSO-SPB1, and EUSO-TA. Along the years, the ESAF code was an essential tool to assess the expected performance of the missions, to fine tune their objectives and to drive the technological developments in order to satisfy the scientific requirements as well as to help in the interpretation of the collected experimental data. In fact, thanks to the missions of the JEM-EUSO program, for the first time the ESAF simulated data have been compared to experimental measurements. Moreover, the large panel of scientific objectives of missions like Mini-EUSO and TUS, required the implementation in ESAF of simplified versions of a large variety of luminous transients aside from EASs, such as elves, meteors, space debris and flashers which were not present in the original ESAF version. In conclusion, evaluation of the expected performance of future space-based missions and interpretation of the experimental data with ESAF simulations indicate that a space-based UHECR detector has a satisfactory performance to contribute in unveiling the origin of the extremely energetic particles of the Universe.

ESAF is expected to remain an essential tool for further developments of the planned missions of the program and for the interpretation of the data they will acquire.

Acknowledgements This work was partially supported by Basic Science Interdisciplinary Research Projects of RIKEN and JSPS KAKENHI Grant (22340063, 23340081, and 24244042), by the ASI-INAF agreement n.2017-14-H.O, by the Italian Ministry of Foreign Affairs and International Cooperation, by the Italian Space Agency through

the ASI INFN agreements Mini-EUSO n. 2016-1-U.0, EUSO-SPB1 n. 2017-8-H.0, OBP (n. 2020-26-Hh.0) and EUSO-SPB2 n. 2021-8-HH.0. by NASA award 11-APRA-0058, 16-APROBES16-0023, 17-APRA17-0066, NNX17AJ82G, NNX13AH54G, 80NSSC18K0246, 80NSSC18K0473, 80NSSC19K0626, 80NSSC18K0464 and 80NS SC22K1488 in the USA, by the French space agency CNES, by the Deutsches Zentrum für Luft- und Raumfahrt, the Helmholtz Alliance for Astroparticle Physics funded by the Initiative and Networking Fund of the Helmholtz Association (Germany), by Slovak Academy of Sciences MVTS JEM-EUSO, by National Science Centre in Poland grants 2017/27/B/ST9/02162 and 2020/37/B/ST9/01821, by Deutsche Forschungsgemeinschaft (DFG, German Research Foundation) under Germany Excellence Strategy – EXC-2094-390783311, by Mexican funding agencies PAPIIT-UNAM, CONACyT and the Mexican Space Agency (AEM), as well as VEGA grant agency project 2/0132/17, by grant S2018/NMT-4291 (TEC2SPACE-CM) "Desarrollo y explotación de nuevas tecnologías para instrumentación espacial en la Comunidad de Madrid", and by State Space Corporation ROSCOSMOS and the Interdisciplinary Scientific and Educational School of Moscow University "Fundamental and Applied Space Research". L. W. Piotrowski acknowledges financing by the Polish National Agency for Academic Exchange within Polish Returns Programme no. PPN/PPO/2020/1/00024/U/00001 and National Science Centre, Poland grant no. 2022/45/B/ST2/02889. A special thanks goes to the original developers of the ESAF code. Without their effort it would have been a much tougher job to setup a simulation and analysis framework as complex and as powerful as ESAF. Their help and support during the transition phase between EUSO and JEM-EUSO is deeply acknowledged.

Data Availability Statement This manuscript has no associated data or the data will not be deposited. [Authors' comment: All the associated data can be read off directly from the figures and is available upon request from the authors.]

Funded by SCOAP[3]. SCOAP[3] supports the goals of the International Year of Basic Sciences for Sustainable Development.

Appendix A: The ESAF design

The ESAF simulation code is structured in several independent modules with the *SimuApplication* at the top of the hierarchy. An instance of this class is created in the *simu_main.cc* file where the method *SimuApplication::DoAll()* is called. This method performs the iterative call of the *SimuApplication::DoEvent ()* method which takes care of the entire physical process on a single event basis. This method creates an instance of the *LightToEuso* class which executes the entire process from primary particle to photons on pupil. Several choices are available for which simulator is to be used but the default option is the *StandardLightToEuso* class. By calling the *StandardLightToEuso::Get()*, the virtual *Get()* methods of the shower generator and of the light production and transport will be called. Each one of the above-mentioned *Get()* methods delivers output objects describing the shower profile, photons in atmosphere and photons on pupil. The choice of the object oriented approach shows its power here where the call of several polymorphic *Get()* methods allows great flexibility. The *SimuApplication::DoEvent()* method calls the virtual *Detector::Get()* method. This method takes care of the entire detector simulation. At this stage, several choices are available between various detector configurations. The most important of them are the *EusoDetector* (activating the RIKEN ray trace code), the *G4Detector* (activating the Geant 4 optics) and other testing or debugging detector simulators. Calling one of the above described methods activates both optics and electronics simulators. As final output of the entire procedure a *Telemetry* object is produced.

The reconstruction procedure is activated in the *reco main.cc* file. Here an instance of the *RecoFramework* class is created and the method *RecoFramework::Execute()* is called. While in the constructor function *RecoFramework::RecoFramework()* the module chain is built, the *RecoFramework::Execute()* method performs the entire sequence of calls to reconstruct the event. In fact, the module sequence is firstly initialized through an iterative call of the *ModuleFactory::MakeModule()* method which allocates all the *RecoModule* objects requested by parameter files. A vector named *fModules* with all the pointers to the *RecoModule* objects is created. In the *RecoFramework::Execute()* method all the modules (which inherit from *RecoModule*) are initialized, called and cleared. Eventually all the output data are saved in a ROOT file. For performing all the mentioned operations, the polymorphic methods *RecoModule::PreProcess(), RecoModule::Process(), RecoModule:: PostProcess() and RecoModule::SaveRootData()* are declared in each module. Each module has a specific function which can be either pattern recognition, direction fitting, profile reconstruction or X_{max} and energy reconstruction. Several modules have been implemented in the course of the years but the most current are the *LTTPreClustering* and *PWISE* for the pattern recognition, the *TrackDirection2* for the direction reconstruction and the *PmtToShowerReco* for the energy reconstruction. A schematic view of the above mentioned structure is shown in Fig. 38.

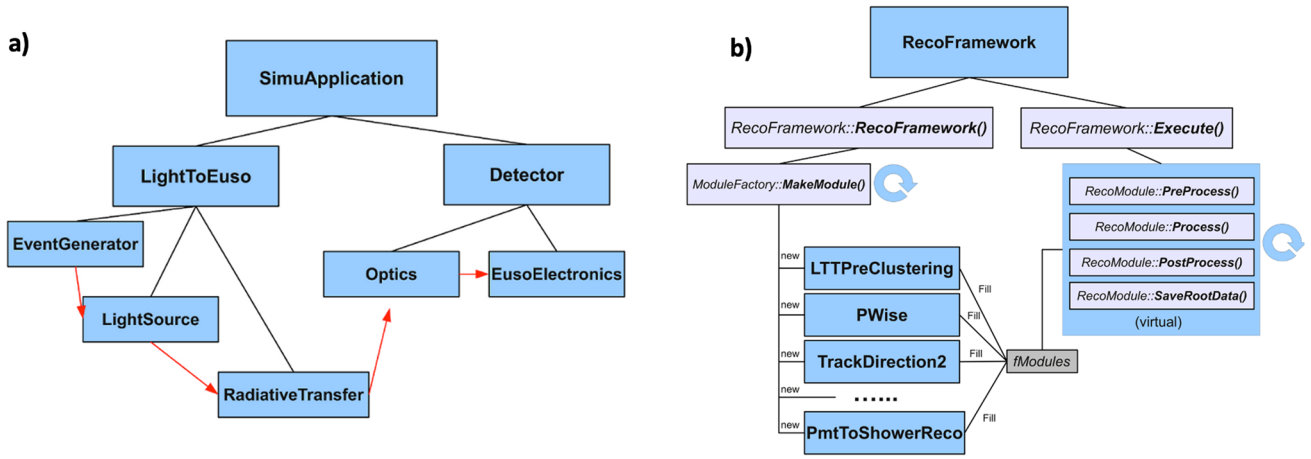

Fig. 38 Panel **a**: A schematic view of the ESAF Simu application structure. The main application is the so called *SimuApplication*. The *LightToEuso* application takes care of all the physical process from shower to detector. The *EusoDetector* (Detector in the panel) application performs the simulation of optics and electronics. Panel **b**: A sketch of the reconstruction framework. The main application *RecoFramework* calls iteratively the *MakeModule* method which allocates all the required modules. In the *Execute* method the operations of all the modules are performed. All the modules are inheriting from the *RecoModule* class. The virtual methods *PreProcess, Process, PostProcess* and *SaveRootData* are called for all the allocated modules. In this picture, blue boxes represent classes, blue-gray boxes methods, the gray box is a C++ *vector* and the circular arrow indicates iterative repetition of some method or sequence of methods. Image adapted from [16]

Appendix B: The main simulation parameters

We present in the following the description of the parameters used in the simulations. Such parameters are the standard but a set of alternatives is still present in ESAF. A review of such parameters can be found in Chapter 3 of the bibliographic reference [58].

The parameterizations for the shower generation, light production and transport are reported in the following:

- Shower parameterization: GIL [42]
- Secondary particle energy distribution: Giller parameterization [100]
- Fluorescence Yield: Nagano et al. [49]
- Atmospheric model: Standard US atmosphere [48]
- Clouds: parametric; uniform layer; optical depth, altitude and thickness by parameter.
- Rayleigh scattering and Ozone absorption modelled according to the lowtran 7 package [50]

The detector is simulated according to the following assumptions:

- A parametric optics in case of POEMMA and TUS. A Gaussian PSF is assumed (ParamOpticalSystem)
- The RIKEN ray trace code for: JEM-EUSO, K-EUSO, Mini-EUSO, EUSO-TA, EUSO-Balloon and EUSO-SPB (NOpticalSystem)
- A parametric optical adaptor is simulated to collect photons on the photocathode (IdealOpticalAdaptor)
- A parametric PMT is simulated. A detection efficiency accounting for quantum and collection efficiency is applied to the photons reaching the photocathode. The gain and gain fluctuations are read in by parameter. A threshold in charge is set on the anode signal to determine the number of counts per pixel per GTU.

The event reconstruction is based on a chain of modules that aim at the reconstruction of the primary parameters:

- the PWISE method is adopted for trace identification. This is optimal for the angular reconstruction [55].
- the LTTPatternRecognition is adopted for trace identification. This is optimal for the profile reconstruction
- the TrackDirection2Module is adopted to reconstruct the direction of the shower as indicated in [57].
- the PmtToShowerReco is adopted to reconstruct the profile of the shower. After a fit of the profile it is possible to retrieve the energy and the X_{max} (see [59]).

Appendix C: A comparison between ESAF and $\overline{\text{Off}}\underline{\text{Line}}$ simulation codes

The two official software packages adopted by the JEM-EUSO collaboration are the Euso Simulation and Analysis Framework (ESAF) [21], originally developed within the EUSO project, and the $\overline{\text{Off}}\underline{\text{Line}}$ package [22] originally designed for the Pierre Auger Observatory [23]. The main motivations to adopt both packages are: (a) it is straightfor-

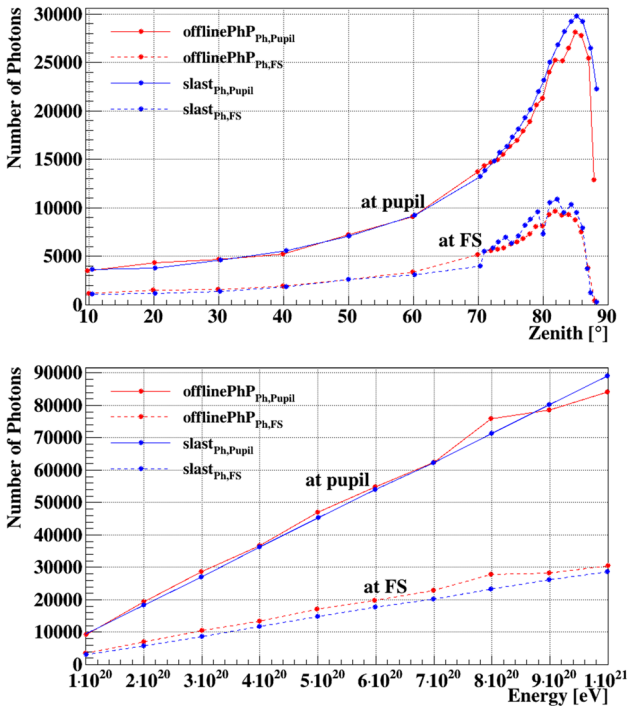

Fig. 39 Comparison between light signals received by the JEM-EUSO detector from simulated proton showers using CONEX+OffLine or ESAF/SLAST simulation codes. Red color indicates the photon counts obtained using OffLine and blue color the corresponding photon counts obtained with SLAST; the continuous lines refer to the signal at the pupil level, while the dashed lines to the signal collected at the Focal Surface (FS) level. The top panel shows the dependence of the photon counts on the zenith angle of the EAS for 10^{20} eV events, while the bottom panel shows the energy dependence of the signal for a fixed zenith angle of 60°. Figure adapted from [101]

ward to re-adapt the EUSO code to the JEM-EUSO configuration; (b) OffLine output is extensively tested within the Pierre Auger Observatory and thus with experimental data; (c) the possibility to adopt both packages gives opportunities for cross-checks. In the following we present a subset of tests that were done in the past years to cross-check the response of the two simulation codes for a mutual validation. A thorough comparison of the codes is out of the scope of this paper.

A first test was performed by comparing the light signal produced in atmosphere by an EAS and its propagation through the atmosphere up to the detector's level. In this case, the light signal generated by showers simulated with SLAST and propagated through the atmosphere using the routines embedded in ESAF was compared to the signal induced by similar showers simulated with CONEX and propagated through the atmosphere according to OffLine routines. Both sets of showers were then passed through the JEM-EUSO detector with ESAF. In this way the possible differences in the results had to be ascribed only to the cascading process and/or light generation in atmosphere. Figure 39 shows the results of this comparison by simulating proton showers with fixed zenith angle (60°) at different energies (top panel) and proton showers at fixed energy (10^{20} eV) with variable zenith angle (bottom panel). The comparison is performed at both the pupil (=aperture) and the focal surface levels. Red color indicates the photon counts obtained using the CONEX+OffLine package and blue color the corresponding photon counts obtained with ESAF/SLAST. There is a general agreement in the light intensity at all energies and angles with a slightly higher signal by ESAF/SLAST at high zenith angles, but the differences remain within 10% level. More details can be found in [101].

The second test refers to the capability of reproducing through an end-to-end simulation the experimentally detected EAS events by EUSO-TA, including the detector response. Figure 40 shows this time the comparison of the event already displayed in Fig. 36 (left panel) simulated with OffLine and ESAF, each one simulating the detector response. Also in this case, both ESAF and OffLine provide a quite similar simulation of the event.

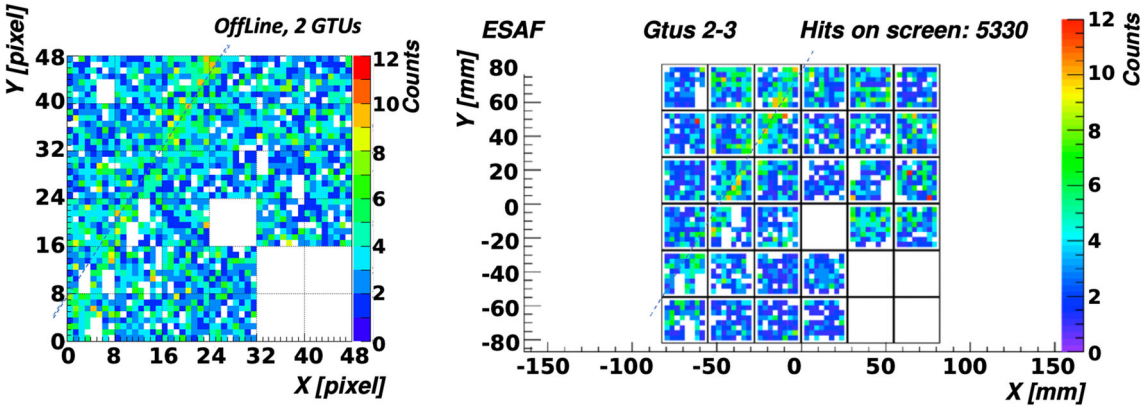

Fig. 40 Comparison between a proton shower simulated with OffLine (left) and ESAF (right) assuming the EAS parameters provided by the TA reconstruction of the event (E = 2.4 × 10^{18} eV, zenith $\theta = 41°$) shown on the left side of Fig. 36

References

1. A. Aab et al., Measurement of the cosmic-ray energy spectrum above 2.5×10^{18} eV using the Pierre Auger Observatory. Phys. Rev. D **102**(6), 062005 (2020). https://doi.org/10.1103/PhysRevD.102.062005. arXiv:2008.06486 [astro-ph.HE]
2. R. Benson, J. Linsley, Satellite observation of cosmic ray air showers. in *17th International Cosmic Ray Conference, Paris, France*, vol. 8 (1981), pp. 145–148
3. Y. Takahashi (OWL), in *Proc. 24th International Cosmic Ray Conference, Rome*, vol. 3 (1995), pp. 595–598
4. F.W. Stecker, J.F. Krizmanic, L.M. Barbier, E. Loh, J.W. Mitchell, P. Sokolsky, R.E. Streitmatter, Observing the ultrahigh-energy universe with OWL eyes. Nucl. Phys. B Proc. Suppl. **136**, 433–438 (2004). https://doi.org/10.1016/j.nuclphysbps.2004.10.027. arXiv:astro-ph/0408162
5. Call for mission proposals for flexi-missions (f2 and f3) (2019). https://sci.esa.int/web/director-desk/-/14685-call-for-mission-proposals-for-flexi-missions. Accessed 22 Feb 2023
6. A.N. Parmar, J. Clavel, O. Catalano, A. Santangelo, in *28th International Cosmic Ray Conference* (2003), pp. 1073–1076
7. Y. Takahashi, The JEM-EUSO mission. New J. Phys. **11**, 065009 (2009). https://doi.org/10.1088/1367-2630/11/6/065009. arXiv:0910.4187 [astro-ph.HE]
8. A. Haungs, G. Medina-Tanco, A. Santangelo, Special issue on the JEM-EUSO mission. Exp. Astron. **40**(1), 1–2 (2015). https://doi.org/10.1007/s10686-015-9483-9
9. M. Casolino et al., The JEM-EUSO instrument. Exp. Astron. **40**(1), 19–44 (2015). https://doi.org/10.1007/s10686-014-9418-x
10. J.H. Adams et al., An evaluation of the exposure in nadir observation of the JEM-EUSO mission. Astropart. Phys. **44**, 76–90 (2013). https://doi.org/10.1016/j.astropartphys.2013.01.008. arXiv:1305.2478 [astro-ph.HE]
11. A. Guzman et al., JEM-EUSO observational capabilities for different UHE primaries. PoS **ICRC2015**, 600 (2016). https://doi.org/10.22323/1.236.0600
12. M.E. Bertaina, An overview of the JEM-EUSO program and results. PoS **ICRC2021**, 406 (2021). https://doi.org/10.22323/1.395.0406
13. G. Abdellaoui et al., EUSO-TA—first results from a ground-based EUSO telescope. Astropart. Phys. **102**, 98–111 (2018). https://doi.org/10.1016/j.astropartphys.2018.05.007
14. J.H. Adams, The EUSO-Balloon pathfinder. Exp. Astron. **40**(1), 281–299 (2015). https://doi.org/10.1007/s10686-015-9467-9
15. G. Abdellaoui et al., EUSO-SPB1 mission and science. Astropart. Phys. 154, 102891 (2024). https://doi.org/10.1016/j.astropartphys.2023.102891
16. J.H. Adams et al., White paper on EUSO-SPB2 (2017). arXiv:1703.04513 [astro-ph.HE]
17. P.A. Klimov et al., The TUS detector of extreme energy cosmic rays on board the Lomonosov satellite. Space Sci. Rev. **212**(3–4), 1687–1703 (2017). https://doi.org/10.1007/s11214-017-0403-3. arXiv:1706.04976 [astro-ph.IM]
18. S. Bacholle et al., Mini-EUSO mission to study Earth UV emissions on board the ISS. Astrophys. J. Suppl. **253**(2), 36 (2021). https://doi.org/10.3847/1538-4365/abd93d. arXiv:2010.01937 [astro-ph.IM]
19. P. Klimov et al., Status of the K-EUSO orbital detector of ultra-high energy cosmic rays. Universe **8**(2), 88 (2022). https://doi.org/10.3390/universe8020088. arXiv:2201.12766 [astro-ph.IM]
20. A.V. Olinto et al., The POEMMA (Probe of Extreme Multi-Messenger Astrophysics) observatory. JCAP **06**, 007 (2021). https://doi.org/10.1088/1475-7516/2021/06/007. arXiv:2012.07945 [astro-ph.IM]
21. C. Berat et al., ESAF: full simulation of space-based extensive air showers detectors. Astropart. Phys. **33**, 221–247 (2010). https://doi.org/10.1016/j.astropartphys.2010.02.005. arXiv:0907.5275 [astro-ph.IM]
22. S. Argiro, S.L.C. Barroso, J. Gonzalez, L. Nellen, T.C. Paul, T.A. Porter, L. Prado Jr., M. Roth, R. Ulrich, D. Veberic, The offline software framework of the Pierre Auger Observatory. Nucl. Instrum. Methods A **580**, 1485–1496 (2007). https://doi.org/10.1016/j.nima.2007.07.010. arXiv:0707.1652 [astro-ph]
23. A. Aab et al., The Pierre Auger cosmic ray observatory. Nucl. Instrum. Methods A **798**, 172–213 (2015). https://doi.org/10.1016/j.nima.2015.06.058. arXiv:1502.01323 [astro-ph.IM]
24. T.C. Paul, M. Bertaina, F. Bisconti, J. Eser, G. Figueiredo, M. Fouka, F. Guarino, L. Peral, Z. Sahnoun, New simulation and reconstruction software for the EUSO pathfinders, with example applications. PoS **ICRC2017**, 464 (2017). https://doi.org/10.22323/1.301.0464
25. B.A. Khrenov, M.I. Panasyuk, V.V. Alexandrov, D.I. Bugrov, A. Cordero, G.K. Garipov, J. Linsley, O. Martinez, H. Salazar, O.A. Saprykin, A.A. Silaev, D.V. Surogatov, V.S. Syromyatnikov, L. Villaseñor, A. Zepeda, Space program KOSMOTEPETL (project KLYPVE and TUS) for the study of extremely high energy cosmic rays. AIP Conf. Proc. **566**(1), 57–75 (2001). https://doi.org/10.1063/1.1378622
26. M.I. Panasyuk, P. Klimov, B. Khrenov, S. Sharakin, M. Zotov, P. Picozza, M. Casolino, T. Ebisuzaki, P. Gorodetzky, Ultra high energy cosmic ray detector KLYPVE on board the Russian Segment of the ISS. PoS **ICRC2015**, 669 (2016). https://doi.org/10.22323/1.236.0669
27. P. Klimov, M. Casolino, Status of the KLYPVE-EUSO detector for EECR study on board the ISS. PoS **ICRC2017**, 412 (2018). https://doi.org/10.22323/1.301.0412
28. F. Fenu, S. Sharakin, M. Zotov, N. Sakaki, Y. Takizawa, M. Bianciotto, M.E. Bertaina, M. Casolino, P. Klimov, Expected performance of the K-EUSO space-based observatory. PoS **ICRC2021**, 409 (2021). https://doi.org/10.22323/1.395.0409. arXiv:2112.11302 [astro-ph.HE]
29. B.A. Khrenov et al., An extensive-air-shower-like event registered with the TUS orbital detector. JCAP **03**, 033 (2020). https://doi.org/10.1088/1475-7516/2020/03/033. arXiv:1907.06028 [astro-ph.HE]
30. M. Casolino et al., Observation of night-time emissions of the Earth in the near UV range from the International Space Station with the Mini-EUSO detector. Remote Sens. Environ. **284**, 113336 (2023). https://doi.org/10.1016/j.rse.2022.113336. arXiv:2212.02353 [astro-ph.IM]
31. G. Abdellaoui et al., Ultra-violet imaging of the night-time earth by EUSO-Balloon towards space-based ultra-high energy cosmic ray observations. Astropart. Phys. **111**, 54–71 (2019). https://doi.org/10.1016/j.astropartphys.2018.10.008
32. G. Abdellaoui et al., First observations of speed of light tracks by a fluorescence detector looking down on the atmosphere. JINST **13**(05), P05023 (2018). https://doi.org/10.1088/1748-0221/13/05/P05023. arXiv:1808.02557 [astro-ph.IM]
33. J.H. Adams et al., A review of the EUSO-balloon pathfinder for the JEM-EUSO program. Space Sci. Rev. **218**(1), 3 (2022). https://doi.org/10.1007/s11214-022-00870-x
34. G. Abdellaoui et al., Cosmic ray oriented performance studies for the JEM-EUSO first level trigger. Nucl. Instrum. Methods A **866**, 150–163 (2017). https://doi.org/10.1016/j.nima.2017.05.043
35. V. Scotti, J. Bayer, F. Cafagna, C. Fornaro, W. Hidber, G. Osteria, F. Perfetto, J. Sanchez, The data processor system of EUSO-SPB1. Nucl. Instrum. Methods Phys. Res. Sect. A: Accel. Spec-

trom. Detect. Assoc. Equip. **916**, 94–101 (2019). https://doi.org/10.1016/j.nima.2018.10.207
36. G. Filippatos, M. Battisti, A. Belov, M. Bertaina, F. Bisconti, J. Eser, M. Mignone, F. Sarazin, L. Wiencke, Development of a cosmic ray oriented trigger for the fluorescence telescope on EUSO-SPB2. Adv. Space Res. **70**, 2794–2803 (2022). https://doi.org/10.1016/j.asr.2021.12.028. arXiv:2201.00794 [astro-ph.HE]
37. J. Eser, A.V. Olinto, L. Wiencke, Overview and first results of EUSO-SPB2. PoS **ICRC2023**, 397 (2023)
38. L.A. Anchordoqui et al., Performance and science reach of the probe of extreme multimessenger astrophysics for ultrahigh-energy particles. Phys. Rev. D **101**(2), 023012 (2020). https://doi.org/10.1103/PhysRevD.101.023012. arXiv:1907.03694 [astro-ph.HE]
39. A. Belov, M. Bertaina, F. Capel, F. Fausti, F. Fenu, P. Klimov, M. Mignone, H. Miyamoto, The integration and testing of the mini-EUSO multi-level trigger system. Adv. Space Res. **62**, 2966–2976 (2018). https://doi.org/10.1016/j.asr.2017.10.044. arXiv:1711.02376 [astro-ph.IM]
40. T. Abu-Zayyad et al., The cosmic ray energy spectrum observed with the surface detector of the telescope array experiment. Astrophys. J. Lett. **768**, L1 (2013). https://doi.org/10.1088/2041-8205/768/1/L1. arXiv:1205.5067 [astro-ph.HE]
41. R. Brun, F. Rademakers, ROOT: an object oriented data analysis framework. Nucl. Instrum. Methods A **389**, 81–86 (1997). https://doi.org/10.1016/S0168-9002(97)00048-X
42. N.P. Ilina, N.N. Kalmykov, V.V. Prosin, Cherenkov radiation and parameters of extensive air showers. Sov. J. Nucl. Phys. **55**, 1540–1547 (1992)
43. D. Heck, J. Knapp, J.N. Capdevielle, G. Schatz, T. Thouw, CORSIKA: a Monte Carlo code to simulate extensive air showers. FZKA 6019 (1998). https://www.iap.kit.edu/corsika/70.php
44. T. Pierog et al., First results of fast one-dimensional hybrid simulation of EAS using CONEX. Nucl. Phys. B Proc. Suppl. **151**, 159–162 (2006). https://doi.org/10.1016/j.nuclphysbps.2005.07.029. arXiv:astro-ph/0411260
45. U.S. Inan, T.F. Bell, J.V. Rodriguez, Heating and ionization of the lower ionosphere by lightning. Geophys. Res. Lett. **18**(4), 705–708 (1991). https://doi.org/10.1029/91GL00364. https://agupubs.onlinelibrary.wiley.com/doi/abs/10.1029/91GL00364
46. A. De Rujula, S.L. Glashow, Nuclearites: a novel form of cosmic radiation. Nature **312**, 734–737 (1984). https://doi.org/10.1038/312734a0
47. Slastshowergenerator (2005). https://www.ge.infn.it/euso/main/Software/docold/SlastShowerGenerator.html. Accessed 22 Feb 2023
48. U.S.C. on Extension to the Standard Atmosphere, *U.S. Standard Atmosphere, 1976: Sponsored by the National Oceanic and Atmospheric Administration, National Aeronautics and Space Administration and United States Air Force* (U.S. Government Printing Office, 1976). https://books.google.it/books?id=Ug_vzQEACAAJ
49. M. Nagano, K. Kobayakawa, N. Sakaki, K. Ando, New measurement on photon yields from air and the application to the energy estimation of primary cosmic rays. Astropart. Phys. **22**, 235–248 (2004). https://doi.org/10.1016/j.astropartphys.2004.08.002. arXiv:astro-ph/0406474
50. F. Kneizys, U.A.F.G. Laboratory, *Users Guide to Lowtran 7*. AFGL-TR (Air Force Geophysics Laboratory, 1988). https://books.google.it/books?id=xOgaAQAAIAAJ
51. N. Sakaki, F. Fenu, Y. Takizawa, M.I. Panasyuk, P. Klimov, S. Sharakin, M. Bertaina, T. Ebisuzaki, S. Ogio, Expected acceptance of the KLYPVE/K-EUSO space-based mission for the observation of ultra-high energy cosmic rays. PoS **ICRC2015**, 647 (2016). https://doi.org/10.22323/1.236.0647
52. S. Biktemerova, M. Gonchar, D. Naumov, Integration of ESAF and Geant4 for simulation of space based telescopes. in *31st International Cosmic Ray Conference, ICRC 2009* (2009)
53. J. Bayer et al., Second level trigger and Cluster Control Board for the JEM-EUSO mission. in *33rd International Cosmic Ray Conference Proceedings (ID0432)*, vol. 99 (2013). arXiv:1307.7071
54. M. Battisti, J. Bayer, M. Bertaina, A. Cummings, J. Eser, F. Fenu, A. Jung, M. Mignone, H. Miyamoto, K. Shinozaki, Performance results of the trigger logic implemented in EUSO-SPB. Nucl. Instrum. Methods A **936**, 349–350 (2019). https://doi.org/10.1016/j.nima.2018.11.002
55. A. Guzman, T. Mernik, A. Santangelo, G. Medina-Tanco, M. Bertaina, K. Shinozaki, F. Fenu, A. Gorgi, The peak and window searching technique for the EUSO simulation and analysis framework: impact on the angular reconstruction of EAS. J. Phys. Conf. Ser. **409**(1), 012104 (2013). https://doi.org/10.1088/1742-6596/409/1/012104
56. M. Bertaina, S. Biktemerova, K. Bittermann, P. Bobik, D. Campana, F. Fenu, A. Gorgi, F. Guarino, A. Guzmán, K. Higashide, G. Medina-Tanco, T. Mernik, D. Naumov, M. Putis, M. Rodríguez Frías, G. Sáez Cano, A. Santangelo, K. Shinozaki, S. Toscano, Performance and air-shower reconstruction techniques for the JEM-EUSO mission. Adv. Space Res. **53**(10), 1515–1535 (2014). https://doi.org/10.1016/j.asr.2014.02.018. https://www.sciencedirect.com/science/article/pii/S0273117714001392. Cosmic Ray Origins: Viktor Hess Centennial Anniversary
57. S. Biktemerova, A. Guzman, T. Mernik, Performances of JEM-EUSO: angular reconstruction. Exp. Astron. **40**(1), 153–177 (2015). https://doi.org/10.1007/s10686-013-9371-0. [Erratum: Exp. Astron. **40**, 179–181 (2015)]
58. F. Fenu, A simulation study of the JEM–EUSO mission for the detection of ultra-high energy cosmic rays. Ph.D. thesis, University of Tübingen (2013)
59. F. Fenu, A. Santangelo, D. Naumov, Performances of JEM–EUSO: energy and X_{max} reconstruction. Exp. Astron. **40**(1), 183–214 (2015). https://doi.org/10.1007/s10686-014-9427-9
60. V.P. Pasko, Y. Yair, C.L. Kuo, Lightning related transient luminous events at high altitude in the Earth's atmosphere: phenomenology, mechanisms and effects. Space Sci. Rev. **168**(1–4), 475–516 (2012). https://doi.org/10.1007/s11214-011-9813-9
61. F. Capel, A. Belov, M. Casolino, P. Klimov, Mini-EUSO: a high resolution detector for the study of terrestrial and cosmic uv emission from the international space station. Adv. Space Res. **62**(10), 2954–2965 (2018). https://doi.org/10.1016/j.asr.2017.08.030. https://www.sciencedirect.com/science/article/pii/S0273117717306257. Origins of Cosmic Rays
62. M. Perdichizzi, Simulation of TLE phenomena in ESAF within the JEM-EUSO project. B. S. thesis, Uninettuno University (2015)
63. A. Nardelli, Meteor simulation in ESAF for the JEM-EUSO mission. B. S. thesis, Uninettuno University (2014)
64. M. Bertaina, A. Cellino, F. Ronga, E. Parizot, D. Allard, JEM-EUSO: meteor and nuclearite observations. Exp. Astron. **40**(1), 253–279 (2015). https://doi.org/10.1007/s10686-014-9375-4
65. P. Pecina, P. Koten, On the theory of light curves of video-meteors. A&A **499**(1), 313–320 (2009). https://doi.org/10.1051/0004-6361/200811503
66. L.G. Jacchia, F. Verniani, R.E. Briggs, An analysis of the atmospheric trajectories of 413 precisely reduced photographic meteors. SAO Special Report 175 (1965)
67. G. Abdellaoui et al., Meteor studies in the framework of the JEM-EUSO program. Planet. Space Sci. **143**, 245–255 (2017). https://doi.org/10.1016/j.pss.2016.12.001
68. G. Garipov, B. Khrenov, M. Panasyuk, V. Tulupov, A. Shirokov, I. Yashin, H. Salazar, UV radiation from the atmosphere: results of the MSU "Tatiana" satellite measurements. Astropart. Phys.

24(4), 400–408 (2005). https://doi.org/10.1016/j.astropartphys.2005.09.001
69. L.M. Barbier, R. Smith, S. Murphy, E.R. Christian, R. Farley, J.F. Krizmanic, J.W. Mitchell, R.E. Streitmatter, E.C. Loh, S. Stochaj, Nightglow: an instrument to measure the earth's nighttime ultraviolet glow-results from the first engineering flight. Astropart. Phys. **22**(5), 439–449 (2005). https://doi.org/10.1016/j.astropartphys.2004.10.002
70. O. Catalano, G. Agnetta, B. Biondo, F. Celi, R. Di Raffaele, S. Giarrusso, J. Linsley, G. La Rosa, A. Lo Bue, A. Mangano, F. Russo, The atmospheric nightglow in the 300–400 nm wavelength: results by the balloon-borne experiment "baby". Nucl. Instrum. Methods Phys. Res. Sect. A: Accel. Spectrom., Detect. Assoc. Equip. **480**(2), 547–554 (2002). https://doi.org/10.1016/S0168-9002(01)00958-5
71. A. Guzman, K. Shinozaki, G. Saez-Cano, D. Allard, C. Blaksley, J.N. Capedevielle, P. Gorodetzky, E. Parizot, T. Patzak, The JEM-EUSO observation in cloudy conditions. Exp. Astron. **40**(1), 135–152 (2015). https://doi.org/10.1007/s10686-014-9377-2
72. T. Pierog, LHC results and high energy cosmic ray interaction models. J. Phys.: Conf. Ser. **409**(1), 012008 (2013). https://doi.org/10.1088/1742-6596/409/1/012008
73. P. Homola, D. Gora, D. Heck, H. Klages, J. Pekala, M. Risse, B. Wilczynska, H. Wilczynski, Simulation of ultrahigh energy photon propagation in the geomagnetic field. Comput. Phys. Commun. **173**, 71–90 (2005). https://doi.org/10.1016/j.cpc.2005.07.001. arXiv:astro-ph/0311442
74. L.D. Landau, I. Pomeranchuk, Electron cascade process at very high-energies. Dokl. Akad. Nauk Ser. Fiz. **92**, 735–738 (1953)
75. A.B. Migdal, Bremsstrahlung and pair production in condensed media at high-energies. Phys. Rev. **103**, 1811–1820 (1956). https://doi.org/10.1103/PhysRev.103.1811
76. T. Mernik, D. Cabrera, A. Santangelo, K. Shinozaki, J. Bayer, E. Iwotschkin, M.E. Bertaina, F. Fenu, The expected angular resolution performance of the tilted JEM-EUSO instrument . PoS **ICRC2015**, 602 (2016). https://doi.org/10.22323/1.236.0602
77. F. Fenu, The JEM-EUSO energy and X_{max} reconstruction performances. PoS **ICRC2015**, 604 (2016). https://doi.org/10.22323/1.236.0604
78. A. Yushkov, Mass composition of cosmic rays with energies above $10^{17.2}$ eV from the hybrid data of the Pierre Auger Observatory. PoS **ICRC2019**, 482 (2020). https://doi.org/10.22323/1.358.0482
79. R.U. Abbasi et al., Depth of ultra high energy cosmic ray induced air shower maxima measured by the telescope array black rock and long ridge FADC fluorescence detectors and surface array in hybrid mode. Astrophys. J. **858**(2), 76 (2018). https://doi.org/10.3847/1538-4357/aabad7. arXiv:1801.09784 [astro-ph.HE]
80. F. Fenu, K. Shinozaki, H. Miyamoto, A. Liberatore, N. Sakaki, S. Sharakin, M. Zotov, G. Chiritoi, Simulations for the JEM–EUSO program with ESAF. PoS **ICRC2019**, 252 (2021). https://doi.org/10.22323/1.358.0252. arXiv:1909.12012 [astro-ph.HE]
81. L. Tkachev, The TUS orbital detector simulation. PoS **ICRC2015**, 610 (2016). https://doi.org/10.22323/1.236.0610
82. D. Barghini et al., UV telescope TUS on board Lomonosov satellite: selected results of the mission. Adv. Space Res. **70**, 2734–2749 (2022). https://doi.org/10.1016/j.asr.2021.11.044
83. D.J. Bird et al., Detection of a cosmic ray with measured energy well beyond the expected spectral cutoff due to cosmic microwave radiation. Astrophys. J. **441**, 144–150 (1995). https://doi.org/10.1086/175344. arXiv:astro-ph/9410067
84. S. Sharakin, O.R. Hernandez, Kinematics reconstruction of the EAS-like events registered by the TUS detector. J. Instrum. **16**(07), T07013 (2021). https://doi.org/10.1088/1748-0221/16/07/T07013
85. F. Fenu, K. Shinozaki, M. Zotov, M.E. Bertaina, A. Castellina, A. Cellino, P. Klimov, Estimation of the exposure of the TUS space-based cosmic ray observatory. PoS **ICRC2021**, 333 (2021). https://doi.org/10.22323/1.395.0333. arXiv:2112.11316 [astro-ph.HE]
86. National Centers for Environmental Prediction, National Weather Service, NOAA, U.S. Department of Commerce. NCEP global forecast system (GFS) analyses and forecasts (2007). https://doi.org/10.5065/D65Q4TSG
87. M. Battisti, D. Barghini, A. Belov, M. Bertaina, F. Bisconti, K. Bolmgren, G. Cambiè, F. Capel, M. Casolino, T. Ebisuzaki, F. Fenu, M. Franceschi, C. Fuglesang, A. Golzio, P. Gorodetzki, F. Kajino, P. Klimov, M. Manfrin, L. Marcelli, W. Marszał, H. Miyamoto, T. Napolitano, E. Parizot, P. Picozza, L. Piotrowski, Z. Plebaniak, G. Prévôt, E. Reali, M. Ricci, N. Sakaki, K. Shinozaki, J. Szabelski, Y. Takizawa, Onboard performance of the level 1 trigger of the mini-EUSO telescope. Adv. Space Res. **70**(9), 2750–2766 (2022). https://doi.org/10.1016/j.asr.2022.07.077. Astrophysics of Cosmic Rays
88. T. Ebisuzaki, M.N. Quinn, S. Wada, L.W. Piotrowski, Y. Takizawa, M. Casolino, M.E. Bertaina, P. Gorodetzky, E. Parizot, T. Tajima, R. Soulard, G. Mourou, Demonstration designs for the remediation of space debris from the international space station. Acta Astronaut. **112**, 102–113 (2015). https://doi.org/10.1016/j.actaastro.2015.03.004
89. H. Miyamoto et al., Space Debris detection and tracking with the techniques of cosmic ray physics. PoS **ICRC2019**, 253 (2021). https://doi.org/10.22323/1.358.0253. arXiv:1909.05601 [astro-ph.IM]
90. H. Miyamoto et al., Simulation studies for the mini-EUSO detector. PoS **ICRC2021**, 334 (2021). https://doi.org/10.22323/1.395.0334. arXiv:2112.12150 [astro-ph.IM]
91. M. Battisti, J. Bayer, M. Bertaina, A. Cummings, J. Eser, F. Fenu, A. Jung, M. Mignone, H. Miyamoto, K. Shinozaki, Performance results of the trigger logic implemented in EUSO-SPB. Nucl. Instrum. Methods A **936**, 349–350 (2019). https://doi.org/10.1016/j.nima.2018.11.002
92. F. Fenu, M.E. Bertaina, A. Bortone, A. Cummings, N. Sakaki, A. Veneziani, S. Cambursano, Expected number of extensive air showers observable by EUSO-SPB. PoS **ICRC2017**, 426 (2018). https://doi.org/10.22323/1.301.0426
93. J. Eser, Results of the EUSO-SPB1 flight. PoS **ICRC2019**, 247 (2019). https://doi.org/10.22323/1.358.0247
94. K. Shinozaki et al., Estimation of the exposure for the air shower detection mode of EUSO-SPB1. PoS **ICRC2019**, 427 (2020). https://doi.org/10.22323/1.358.0427. arXiv:1909.05713 [astro-ph.HE]
95. M. Vrábel, J. Genci, P. Bobik, F. Bisconti, Machine learning approach for air shower recognition in EUSO-SPB data. PoS **ICRC2019**, 456 (2020). https://doi.org/10.22323/1.358.0456
96. F. Fenu, The simulation of cosmic rays in EUSO–Balloon: performances of the direction and energy reconstruction. PoS **ICRC2015**, 609 (2016). https://doi.org/10.22323/1.236.0609
97. T. Mernik, A. Guzman, A. Santangelo, K. Shinozaki, N. Sakaki, C. Moretto, D. Monnier Ragaigne, H. Miyamoto, S. Dagoret Campagne, C. Catalano, P. Von Ballmoos, *ESAF-Simulation of the EUSO-Balloon, 33rd International Cosmic Ray Conference Proceedings (ID0875)*, vol. 51 (2013). arXiv:1307.7071
98. F. Bisconti, F. Catalano, F. Fenu, M.E. Bertaina, T.C. Paul, H. Shin, Simulation study of the detected and expected events for the EUSO-TA fluorescence detector. PoS **ICRC2017**, 463 (2018). https://doi.org/10.22323/1.301.0463

99. M.G. Aartsen et al., Measurement of the cosmic ray energy spectrum with IceTop-73. Phys. Rev. D **88**(4), 042004 (2013). https://doi.org/10.1103/PhysRevD.88.042004. arXiv:1307.3795 [astro-ph.HE]
100. M. Giller, G. Wieczorek, A. Kacperczyk, H. Stojek, W. Tkaczyk, Energy spectra of electrons in the extensive air showers of ultra-high energy. J. Phys. G **30**, 97–105 (2004). https://doi.org/10.1088/0954-3899/30/2/009
101. M. Blaicher, End-to-end simulation of the extreme universe space observatory (EUSO). B. S. thesis, Karlsruhe Institute of Technology (2012). https://publish.etp.kit.edu/record/20826